TOPOLOGICAL PHASES IN SELF-SIMILAR SYSTEMS

Dissertation

SASWAT SARANGI

Max-Planck-Institut für Physik komplexer Systeme

Institut für Theoretische Physik
Fakultät Physik
Technische Universität Dresden

Dresden, Deutschland
March, 2024

TOPOLOGICAL PHASES IN SELF-SIMILAR SYSTEMS

Dissertation

zur Erlagung des akademischen Grades
Doctor in Philosophy (Ph.D.)
vorlegt dem Bereich Mathematik und Naturwissenschaften

von

SASWAT SARANGI

Prof. Dr. Anne E. B. Nielsen.
Prof. Dr. Roderich Moessner

Max-Planck-Institut für Physik komplexer Systeme

Institut für Theoretische Physik
Fakultät Physik
Technische Universität Dresden

Dresden, Deutschland
March, 2024

Eingereicht am 12.10.2023

Betreuer : 1. Prof. Dr. Anne E. B. Nielsen
2. Prof. Dr. Roderich Moessner

Vorsitzender : Prof. Dr. Liu Hao Tjeng

Gutachter : 1. Prof. Dr. Roderich Moessner
2. Prof. Dr. Jan C. Budich

Rigorosum : 1. Prof. Dr. Holger Kantz
2. Prof. Dr. Carsten Timm

Protokollant : Dr. Suraj Hegde

Verteidigt am 05.03.2024

I do not know what I may appear to the world, but to myself I seem to have been only like a boy playing on the sea-shore, and diverting myself in now and then finding a smoother pebble or a prettier shell than ordinary, whilst the great ocean of truth lay all undiscovered before me.

— Sir Isaac Newton. [SM20]

Dedicated to my loved ones.

ABSTRACT

The study of topological phases in condensed matter physics has seen remarkable advancements, primarily focusing on systems with a well-defined bulk and boundary. However, the emergence of topological phenomena on self-similar systems, characterized by the absence of a clear distinction between bulk and boundary, presents a fascinating challenge. This thesis focuses on the topological phases on self-similar systems, shedding light on their unique properties through the lens of adiabatic charge pumping. We observe that the spectral flow in these systems exhibits striking qualitative distinctions from that of translationally invariant non-interacting systems subjected to a perpendicular magnetic field. We show that the instantaneous eigenspectra can be used to understand the quantization of the charge pumped over a cycle, and hence to understand the topological character of the system. Furthermore, we establish a correspondence between the local contributions to the Hall conductivity and the spectral flow of edge-like states. We also find that the edge-like states can be approximated as eigenstates of the discrete angular-momentum operator, with their chiral characteristics stemming from this unique perspective. We also investigate the effect of local structure on the topological phases on self-similar structures embedded in two dimensions. We study a geometry dependent model on two self-similar structures having different coordination numbers, constructed from the Sierpinski gasket. For different non-spatial symmetries present in the system, we numerically study and compare the phases on both structures. We characterize these phases by the localization properties of the single-particle states, their robustness to disorder, and by using a real-space topological index. We find that both structures host topologically nontrivial phases and the phase diagrams are different on the two structures, emphasizing the interplay between non-spatial symmetries and the local structure of the self-similar unit in determining topological phases. Furthermore, we demonstrate the presence of topologically ordered chiral spin liquid on fractals by extending the Kitaev model to the Sierpinski Gasket. We show a way to perform the Jordan-Wigner transformation to make this model exactly solvable on the Sierpinski Gasket. This system exhibits a fractal density of states for Majorana modes and showcases a transition from a gapped to a gapless phase. Notably, the gapped phase features symmetry-protected Majorana corner modes, while the gapless phase harbors robust zero-energy and low-energy self-similar Majorana edge-like modes. We also study the vortex excitations, characterized by remarkable localization properties even in small fractal generations. These localized excitations exhibit anyonic behavior, with preliminary calculations hinting at their fundamental differences anyons observed in the Kitaev model on a honeycomb lattice.

PUBLICATIONS

Some ideas and figures have appeared previously in the following publications:

[SN21] Sarangi, S., Nielsen, A. (2021). Effect of coordination on topological phases on self-similar structures. Phys. Rev. B, 104, 045147.
DOI: https://doi.org/10.1103/PhysRevB.104.045147

[SN23] Sarangi, S., Nielsen, A. (2023). Adiabatic pumping and transport in the Sierpinski-Hofstadter model. Phys. Rev. Res., 5, 033132.
DOI: https://doi.org/10.1103/PhysRevResearch.5.033132

Science is the search for truth - it is not a game in which one tries to beat his opponent, to do harm to others. We need to have the spirit of science in international affairs, to make the conduct of international affairs the effort to find the right solution, the just solution of international problems, not the effort by each nation to get the better of other nations, to do harm to them when it is possible.

— Linus Pauling [PH58]

ACKNOWLEDGMENTS

I would like to extend my sincere gratitude to my Ph.D. supervisor, Prof. Dr. Anne E. B. Nielsen, for her invaluable guidance and unwavering support throughout my doctoral journey. I am also deeply appreciative of Prof. Dr. Roderich Moessner for his leadership as the head of the Condensed Matter Division at MPIPKS.

I want to express my heartfelt thanks to all the members of our research group, with special appreciation to Hadi and Aniket, for their invaluable support, insightful physics discussions, and guidance during critical phases of my research. It was a pleasure to be in the company of my dear friends Aidan, Sid, Daniele, Sayantan, Puneet, Dillip, Mani, Błażej, Roberto, Tobias and Giacomo.

I am also grateful to various departments and teams at MPIPKS, including the Visitors' Program, HR department, cafeteria, IT department, and administrative staff, who were always ready to address any issues and provide assistance throughout my time here.

Last but not least, my heartfelt thanks go to my parents, whose unwavering support has made my career at MPIPKS possible.

CONTENTS

1

INTRODUCTION

The field of condensed matter physics has witnessed a remarkable evolution, with topological phases emerging as a captivating frontier. These phases, which encompass a diverse range of exotic behaviors, have fundamentally reshaped the understanding of quantum matter. This field delves into the exotic behaviors of quantum matter that cannot be described by traditional symmetry-breaking paradigms. In essence, topological phases represent a new realm of understanding in condensed matter physics, opening the door to novel material properties and potential technological applications.

The journey into the realm of topological phases began with the groundbreaking discovery of the Integer Quantum Hall Effect (IQHE) in the early 1980s. This breakthrough phenomenon demonstrated that in two-dimensional electron gases subjected to strong magnetic fields, the Hall conductivity becomes quantized in integer multiples of a fundamental constant (e^2/h) to better than one part in 10^5 along with the presence of robust current carrying edge states, a profound manifestation of topological order [KDP80; Lau81; Hal82]. The quantization of Hall conductivity is intimately linked to the underlying topology of the electronic wavefunctions, reflecting the robustness of these topological phases against perturbations [Lau81; Tho+82]. Subsequently, the Fractional Quantum Hall Effect (FQHE) unfolded as another remarkable chapter in this history, introducing anyons as fractional charge quasiparticles and emphasizing the exotic nature of topological phases [TSG82; WEN90]. These seminal discoveries marked a paradigm shift in the study of condensed matter, shifting the focus from conventional symmetry-breaking transitions to the exploration of topological phases and their intricate interplay with quantum matter.

The topological nature of the IQHE is further underscored by the existence of energy gaps between different Landau levels, which represent distinct quantum states. As a result, the many-body ground state is gapped when the fermi energy lies in the gap between two landau levels which implies that electronic correlations are weak. In such cases, the electron-electron interaction can be safely ignored while describing the low-energy physics and ground-state properties. These gaps are a consequence of the magnetic field-induced quantization which protect the topological properties of the system against small perturbations. The presence of magnetic field results in the change in the phase of the electronic wavefunctions as one moves through the momentum space. The winding number represents the net change in phase or the number of times the phase "winds around" the Brillouin zone which is quantified by the TKNN invariant or the Chern number.

The Hall conductivity in IQHE is directly related to the TKNN invariant; its quantized nature being a consequence of this [Tho+82].

The principles underpinning the Integer Quantum Hall Effect (IQHE) resonate throughout a broader context encompassing various topological phases. A notable illustration of this resonance emerges in certain crystalline insulators like Chern insulators and topological insulators, in which non-interacting electrons show similar behaviour as IQHE in the absence of external magnetic field as a result of their intrinsic topological character. These insulators feature gapped energy bands due to the translational invariance within the crystalline lattice, which naturally establishes the Brillouin zone as the parameter space for defining essential topological invariants, such as the Chern number (TKNN invariant). In the context of non-interacting systems, the systems with a non-zero topological invariants are said to belong to a topologically non-trivial phase as they cannot be adiabatically deformed to a trivial insulator. Topologically non-trivial phases are usually identified by the presence of robust in-gap boundary modes, and are characterized by relevant topological invariants [KM05; FK07]. These phases are well understood for translationally invariant systems, as the presence of a well-defined momentum eigenbasis gives a natural setting to describe the topology of bulk wavefunctions. Systematic classification of topological phases on non-interacting translationally invariant systems has been done in terms of both non-spatial and spatial symmetries [Sch+08; Kit09; Fu11; Lud15; Sla+13; Chi+16].

While translational invariance serves as a fundamental condition for the presence of a well-defined momentum eigenbasis, it is increasingly evident that this requirement is not essential for the existence of topological phases. Surprisingly, topological phases have been discovered and extensively studied in systems that lack translational invariance, such as quasi-periodic, quasi-crystalline, and amorphous materials [DMN20; AS17; Mit+18]. Unlike their crystalline counterparts, these systems do not possess a well-defined momentum eigenbasis, making it impossible to describe topologically non-trivial phases through the traditional notion of winding of eigenstates over a manifold in momentum space, similar to the Bloch states' winding in k-space for translationally invariant non-interacting systems. However, what these systems retain is the concept of a well-defined 'bulk' and 'boundary', akin to regular lattice systems with open 'boundary'. Consequently, it becomes feasible to define (albeit approximately) 'boundary' conditions analogous to periodic boundary conditions in lattices. The identification of topologically non-trivial phases in such systems hinges on several key characteristics. These include a gapped spectrum under 'periodic' boundary conditions which captures the physics in the bulk, and the presence of in-gap edge states in scenarios with open boundary conditions which captures the physics on the boundary. Real-space formulations of topological invariants, such as the real-space Chern number and the Bott Index, become

instrumental in characterizing these phases. The discovery and study of topological phases in non-crystalline settings have not only expanded our understanding but have also led to a more comprehensive comprehension of these phases, transcending the confines of translationally invariant systems.

Traditional understandings of topological phases in non-interacting crystalline systems have been grounded in the existence of a well-defined k-space manifold within the bulk and a gapped bands. The emergence of edge states under open boundary conditions is conventionally interpreted as a manifestation of the bulk topology, as described by the bulk-boundary correspondence. However, the landscape shifts when considering amorphous and quasi-crystalline systems. These systems lack the well-defined k-space eigenbasis seen in crystalline materials but retain the notion of locality, and well-defined bulk and boundary. The discovery of topological phases within systems like amorphous and quasi-crystalline materials has fostered a broader understanding of topological phenomena that relies on the presence of well-defined gapped bulk. This naturally raises the intriguing question: what transpires in systems where the distinction between a well-defined bulk and boundary becomes less clear; thereby bringing fractals and self-similar structures into the picture. Examples of such systems are tight-binding models defined on finite truncations of fractals like the Sierpinski Gasket (SG) and the Sierpinski Carpet (SC) with one or more degrees of freedom per site [Aga19; BCN18; Fre+20; PP19; IKY20]. Non-trivial phases have been reported in such systems. These phases seem to be identified with the presence of gapless self-similar states which are chiral in nature and are localized around each of the intrinsic 'holes' present in these structures[Aga19; BCN18; PP19]. Also, the Hall conductivity in such phases is shown to be quantized and robust to small disorders [BCN18; Fis+21]. These phases also seem to be characterized by a non-zero value of real-space topological invariants and hence have also been dubbed 'topological'.

The study of topological phases in self-similar structures presents a captivating challenge, as several key aspects remain shrouded in ambiguity. While non-trivial phases exhibiting some semblance to conventional topological phases have been reported, a comprehensive understanding of these phases continues to elude us. The existing literature offers only a limited microscopic comprehension of these phases. One puzzling observation pertains to the real-space invariants employed to characterize these systems. Traditionally, these invariants are well-defined when there exists a group of states, isolated from the rest of the spectrum by energy gaps. Intriguingly, in certain self-similar phases, these invariants are reported to be quantized even when the spectrum remains gapless, lacking a distinct group of isolated states. The microscopic origin of this quantization not yet understood well. Equally perplexing is the emergence of special self-similar chiral states. In amorphous systems, a periodic boundary condition can be defined, yielding a gapped spectrum. The in-gap states appearing in open-boundary condi-

tions, localized along the boundary, are readily interpreted as manifestations of bulk topology. However, the absence of a clear demarcation between bulk and boundary in fractal structures raises uncertainty regarding the interpretation of these self-similar special chiral states. Whether or not they can truly be understood as analog to edge states in integer-dimensional systems is still not clear. Several other questions intensify the quest for understanding: Can the comprehension of topological phases within self-similar systems somehow be linked to our understanding of lattices? What variables dictate the presence and properties of topological phases within self-similar systems: the Hausdorff dimension of the fractal, non-spatial symmetries, or the coordination number? Is it possible to realize non-trivial topological order on interacting systems with fractal geometries, such as the chiral spin liquids on fractals? These questions underscore the captivating journey of discovery that lies ahead, promising to shed light on the intricate nature of topological phases within self-replicating structures. Moreover, with the recent advances in the field of experimental physics, it possible to realize and study such quantum systems in controlled lab settings [Xu+21], making this study even more relevant. This thesis endeavors to contribute to this fascinating field of study by addressing some of these questions, striving to present a comprehensive understanding of topological phases in self-similar systems.

This document is divide in three parts. The first part is subdivided into two chapters and deals with the preliminaries. The second part is also subdivided into 2 parts where we present our study of the non-interacting models on self-similar structure. This is based on our works in Ref. [SN23] and Ref. [SN21]. And in the third part we present our yet unpublished ongoing study on the chiral spin-liquid on fractals before finally concluding the document.

In chapter 2, we review some of the fundamental works in topology in order to provide foundational knowledge necessary to grasp the core concepts underpinning our research in this thesis. We introduce the concept of topology and Chern number in 2-dimensional systems through Harper-Hofstadter model. We also present real-space topological invariants as essential tools for characterizing topological phases in systems lacking translational invariance.

In chapter 3, we introduce fractals and and review some of the existing works on fractals in the literature. It begins with an exploration of tight-binding models on fractals and self-similar graphs, offering the requisite mathematical framework. Furthermore, the chapter describes prior works on the Harper-Hofstadter model on Sierpinski Gasket, setting the stage for the original research presented in the subsequent chapters.

In chapter 4, we present an understanding of quantization of Hall conductivity in self-similar structures, hence topology, from a perspective of adiabatic charge pumping. A central focus is the establishment of a correspondence that connects the local nature of spectral flow to local contribu-

tions to the Hall conductivity. We present an understanding of edge-like states in fractals like the Sierpinski gasket in terms of eigenstates of particle on a ring. We further examine self-similar structures with different Hausdorff dimensions, shedding light on the topological characteristics of these structures. We also establish a connection between the well-established bulk-boundary correspondence observed in square lattices and the local correspondence within self-similar fractals mentioned above.

In chapter 5, we study the role of non-spatial symmetries on the topological phases in self-similar system. Specifically, we investigate the interplay between non-spatial symmetries and the inherent self-similarity of structures. Owing to the self-similarity of these structures, the way the sites are coordinated locally becomes an important aspect to study. Through numerical calculations, we demonstrate that in the presence of certain non-spatial symmetries, the coordination number becomes an important factor in deciding if the system can host a topological phase.

Chapter 6 delves into the realm of spin-liquids within fractal structures. We show the existence of an exactly solvable topologically ordered chiral spin liquid on self-similar systems by studying Kitaev model on a self-similar graph embedded in Sierpinski gasket. We present a way to perform the Jordan-Wigner transformation on the corresponding (non-bipartite) graph making the model exactly solvable. The system fractionalizes into Majorana fermions and Z2 fluxes with a fractal density of states of the Majorana modes. We further show the existence of a gapped and gapless phases, with the presence of symmetry-protected robust Majorana corner modes in the gapped phase and the robust presence zero-energy and low-energy self-similar Majorana modes in the gapless phase.

Chapter 7 offers a reflective summary of the research findings and their implications. It synthesizes key insights and connections between the diverse aspects explored in the preceding chapters. The chapter concludes with a forward-looking perspective, highlighting potential avenues for future research and the lasting relevance of the discoveries made within the context of topological phases within self-similar structures.

Part I

PRELIMINARIES

In this part, we review the concepts which are necessary to motivate the main ideas of this work and would be used in the subsequent chapters of this thesis. Specifically, we review two main concepts, (i) concepts of topological phases in non-interacting lattice systems, and (ii) we present a scheme to construct self-similar graphs on from fractals, study simple tight binding models using these graphs, and show how the idea of real space renormalization can be inherently associated with these graphs.

2

TOPOLOGICAL PHASES IN NON-INTERACTING LATTICE SYSTEMS

Topology is the study of geometrical properties of a system which remain unaffected under continuous deformations. These deformations can be something like including stretching, twisting, and bending, all executed without abrupt structural discontinuities, such as tearing or puncturing. Properties that do not change throughout these continuous changes are called as topological invariants. Similarly, in the context of condensed matter physics, topological phases are the phases of matter which remain invariant when Hamiltonian of the system is continuously deformed.

Traditionally, condensed matter physics focused on understanding phases of matter through the lens of symmetry breaking. However, the discovery of the quantum Hall effect played a pivotal role in the development of the field of topology in condensed matter physics. The quantum Hall effect was first observed in 1980 by Klaus von Klitzing, who later received the Nobel Prize in Physics for this groundbreaking discovery. The effect occurs when a two-dimensional electron gas (2DEG) is subjected to a strong magnetic field perpendicular to its plane, resulting in the emergence of quantized Hall resistance.

The significance of the quantum Hall effect lies in its robustness and the presence of highly conductive edge states that are insensitive to disorder and imperfections. These edge states are topologically protected, meaning they are immune to local perturbations and can only be destroyed by a phase transition. This behavior immediately captured the attention of physicists and led to a deeper exploration of topological properties in condensed matter systems. In this chapter, we review some existing literature demonstrating the idea of topology in condensed matter systems, focusing primarily on two dimensional lattice systems.

2.1 THE BERRY PHASE, BERRY CURVATURE AND THE CHERN NUMBER

Berry phase and Berry curvature are few of the key ideas demonstrating the emergence of geometry and topology in quantum mechanical systems. Here, we will mainly focus on abelian Berry curvatures. A more general discussion can be found in reference [SW89].

Consider a Hamiltonian $H(\varphi(t))$ which depends on a time dependent parameter $\varphi(t)$. Note that this parameter can be a vector. We consider the

ground state, $|\psi\rangle$ of this system and look at how the state evolves when the Hamiltonian adiabatically evolves along a closed path in the parameter space. The evolution of the state is given by the time-dependent Schrodinger equation

$$i\hbar\frac{\partial|\psi(t)\rangle}{\partial t} = H(\varphi(t))\psi(t) \tag{2.1}$$

We denote the instantaneous ground states of the Hamiltonian by $|n(\varphi)\rangle$. Note that the choice of phases for the instantaneous ground states are fixed but arbitrary. In the absence of any level crossings, the adiabatic theorem states that the ground state would evolve and acquire a phase given by, $|\psi(t)\rangle = e^{i\theta(t)}e^{i\gamma}|n(\varphi(t))\rangle$, where $\theta(t) = -(1/\hbar)\int_0^t E_0(\varphi(t'))dt'$ is the dynamical phase and $\gamma(t) = \int_0^t i\langle n(\varphi(t'))|\dot{n}(\varphi(t'))\rangle\, dt'$ is the geometrical phase. We are not interested in the dynamical phase and we can get rid of it by setting $E_0(t) = 0$. This would correspond to a simple redefinition of the Hamiltonian $H(\varphi) \to H(\varphi) - E_0(\varphi)$, under which the instantaneous eigenstates remain unchanged.

To demonstrate the geometrical nature of the geometric phase, we define a *Berry connection*

$$\mathcal{A}_j(\varphi) = -i\langle n|\frac{\partial}{\partial\varphi_j}|n\rangle\,. \tag{2.2}$$

When we evolve the ground state adiabatically along a closed curve C in the parameter space, the geometrical nature of the geometrical phase shows up as γ can then be expressed in a time independent form (only depends on the path in the parameter space)

$$\gamma = -\int_0^t \mathcal{A}_j(\varphi)\frac{\partial\varphi^j}{\partial t'}dt' = -\oint_C \mathcal{A}_j(\varphi)d\varphi^j \tag{2.3}$$

However, the Berry connection is not gauge invariant. It is dependent on the initial choice of phases of $|n(\varphi)\rangle$. Suppose we change the phase of the instantaneous ground states by a parameter dependent phase $|n'(\varphi)\rangle = e^{i\omega(\varphi)}|n(\varphi)\rangle$. Then the corresponding Berry connection would be given by $\mathcal{A'}_j = \mathcal{A}_j + \partial\omega/\partial\varphi^j$. This takes the same form as the gauge transformation of magnetic vector potential in electromagnetism. Following the analogy from electromagnetism, we remove this gauge redundancy by defining the *curvature* of the connection. The *Berry curvature* is then given by

$$\mathcal{F}_{jk} = \frac{\partial\mathcal{A}_j}{\partial\varphi^k} - \frac{\partial\mathcal{A}_k}{\partial\varphi^j} = -i\left(\left\langle\frac{\partial n}{\partial\varphi^k}\middle|\frac{\partial n}{\partial\varphi^j}\right\rangle - \left\langle\frac{\partial n}{\partial\varphi^j}\middle|\frac{\partial n}{\partial\varphi^k}\right\rangle\right) \tag{2.4}$$

We can express the berry phase in terms of the Berry curvature by using the generalized Stokes theorem

$$\gamma = -\oint_C \mathcal{A}_j(\varphi)d\varphi^j = -\int_S \mathcal{F}_{jk}dS^{jk}, \tag{2.5}$$

where S is the two-dimensional area in the parameter space which is bounded by the contour C. This shows that the Berry phase is also gauge invariant and contains physical information.

Till now, we have only shown the emergence of geometry in quantum mechanical systems in the context of adiabatic evolution. Next we demonstrate the emergence of topology. The Berry phase can be expressed in the form an integral of a curvature over a surface in the parameter space. However if the surface in the parameter space is a smooth closed surface, then by Chern-Gauss-Bonnet theorem, the integral of the curvature over the surface is quantized in the units of 2π. To see emergence of such a quantity in quantum mechanical systems, let us consider the derivatives of the Hamiltonian with respect to the adiabatic parameters. The expectation values of the derivative of the Hamiltonian in the ground state is given by

$$\begin{aligned}
\langle\psi(t)|\frac{\partial H(\varphi)}{\partial\varphi^j}|\psi(t)\rangle &= \frac{\partial}{\partial\varphi^j}\langle\psi(t)|H(\varphi)|\psi(t)\rangle \\
&\quad - \left\langle\frac{\partial\psi(t)}{\partial\varphi^j}\middle|H(\varphi)\middle|\psi(t)\right\rangle - \left\langle\psi(t)\middle|H(\varphi)\middle|\frac{\partial\psi(t)}{\partial\varphi^j}\right\rangle \\
&= -i\left(\left\langle\frac{\partial\psi(t)}{\partial\varphi^j}\middle|\frac{d\psi(t)}{dt}\right\rangle - \left\langle\frac{d\psi(t)}{dt}\middle|\frac{\partial\psi(t)}{\partial\varphi^j}\right\rangle\right) \\
&= -i\left(\left\langle\frac{\partial n(\varphi)}{\partial\varphi^j}\middle|\frac{dn(\varphi)}{dt}\right\rangle - \left\langle\frac{dn(\varphi)}{dt}\middle|\frac{\partial n(\varphi)}{\partial\varphi^j}\right\rangle\right) \\
&= -i\frac{d\varphi^k}{dt}\left(\left\langle\frac{\partial n(\varphi)}{\partial\varphi^j}\middle|\frac{\partial n(\varphi)}{\partial\varphi^k}\right\rangle - \left\langle\frac{\partial n(\varphi)}{\partial\varphi^k}\middle|\frac{\partial n(\varphi)}{\partial\varphi^j}\right\rangle\right) \\
&= \dot{\varphi^k}\mathcal{F}_{jk}
\end{aligned} \tag{2.6}$$

where we have used $|dn(\varphi)/dt\rangle = \dot{\varphi^k}\,|\partial n/\partial\varphi^k\rangle$ going from the third line to the fourth line. Suppose the adiabatic parameters lie on a 2-dimensional smooth closed surface, S, (for example, a torus). Then a topological quantity, namely the first Chern number, emerges when we average out the initial values of adiabatic parameters in Eq. (2.6),

$$\left\langle\frac{\partial H(\varphi)}{\partial\varphi^j}\right\rangle = \int_S\frac{d^2\varphi}{(2\pi)^2}\langle\psi(t)|\frac{\partial H(\varphi)}{\partial\varphi^j}|\psi(t)\rangle = \dot{\varphi^k}\int_S\frac{d^2\varphi}{(2\pi)^2}\mathcal{F}_{jk}. \tag{2.7}$$

The integral of the curvature over the closed surface is the first Chern number given by

$$\mathcal{C} = \frac{1}{2\pi}\int_S d^2\varphi\mathcal{F}_{jk} \tag{2.8}$$

and is always an integer: $\mathcal{C}\in\mathbb{Z}$, as a consequence of the Chern-Gauss-Bonnet theorem.

While we have introduced the concept of Berry curvature and Chern numbers arising from adiabatic dynamics, it's important to note that such curvatures have broader applications. For instance, consider particles on a lattice with translational invariance. In two-dimensional translationally invariant systems, the Hamiltonian exhibits block diagonalization in the quasi-momentum basis due to this invariance. Each block is labeled by a quasi-momentum vector $\mathbf{k} = (k_x, k_y)$, and we denote the corresponding Hamiltonian block as $H(\mathbf{k})$. Consequently, the Brillouin zone naturally becomes the parameter space for the Hamiltonian $H(\mathbf{k})$. The Hall conductivity can then be expressed as an integral of the curvature over the Brillouin zone, known as the TKNN [Tho+82] invariant, given by:

$$\sigma_{xy} = \frac{-ie^2}{h} \sum_{\alpha} \mathcal{C}_\alpha; \quad \mathcal{C}_\alpha = \int_{\mathbf{BZ}} \frac{d^2\mathbf{k}}{2\pi} \left(\left\langle \frac{\partial u^\alpha_{\mathbf{k}}}{\partial k_x} \middle| \frac{\partial u^\alpha_{\mathbf{k}}}{\partial k_y} \right\rangle - \left\langle \frac{\partial u^\alpha_{\mathbf{k}}}{\partial k_y} \middle| \frac{\partial u^\alpha_{\mathbf{k}}}{\partial k_x} \right\rangle \right), \tag{2.9}$$

Here, α represents the index of the filled bands, and $\int_{\mathbf{BZ}}$ denotes the integral over the Brillouin zone. The Chern number $\mathcal{C}_\alpha$ is well-defined as long as the band remains gapped from the rest of the spectrum. Being solely dependent on the eigenvectors, it remains invariant under continuous deformation of the spectra as long as the gap remains open, making it 'topological' in essence.

2.2 REAL-SPACE FORMULATIONS OF CHERN NUMBER

Although $\mathcal{C}_\alpha$ is defined above in the momentum basis, the Chern number is not dependent on the choice of basis of representation being a physical property of the system. So, it is possible to express the Chern number in terms of the projectors on to the set of occupied states given by

$$\mathcal{C} = \int_{\mathrm{BZ}} \frac{d^2\mathbf{k}}{2\pi i} \mathrm{Tr}(P_{\mathbf{k}}[\frac{\partial P_{\mathbf{k}}}{\partial k_x}, \frac{\partial P_{\mathbf{k}}}{\partial k_y}]) \tag{2.10}$$

where $P_{\mathbf{k}}$ is the projector on to the set of occupied states with quasi-momentum $\mathbf{k}$ [PHB10]. The corresponding real-space formulation is obtained by identifying $\boldsymbol{\nabla}_{\vec{K}} = -i\hat{\mathbf{r}}$, where $\hat{\mathbf{r}}$ is the position operator. Using this we can express $\partial P_{\mathbf{k}}/\partial k_x = -i[\hat{x}, P_{\mathbf{k}}]$ and $\partial P_{\mathbf{k}}/\partial k_y = -i[\hat{y}, P_{\mathbf{k}}]$. Substituting this into Eq. (2.10) and using $\int_{\mathrm{BZ}} d^2\mathbf{k} P_{\mathbf{k}}/(2\pi)^2 = P$, we get that

$$\mathcal{C} = -2\pi i \,\mathrm{tr}_{cell}(P[[\hat{x}, P], [\hat{y}, P]]) \tag{2.11}$$

where tr_{cell} refers to the trace over the degrees of freedom of a single unit cell [PHB10] and the area of a unit cell is taken to be 1. We note that $P[\hat{x}, \hat{y}]P = [P\hat{x}P, P\hat{y}P] - P[\hat{x}, \hat{y}P] = [P\hat{x}P, P\hat{y}P]$, giving us $\mathcal{C} = -2\pi i \,\mathrm{tr}_{cell}[P\hat{x}P, P\hat{y}P]$. So, one can identify the real-space Chern marker operator to be $\hat{\mathcal{C}} = -2\pi i[P\hat{x}P, P\hat{y}P]$. The same result has been obtained independently in Ref. [BR11], with a slight reformulation in the form of the local Chern marker where they identify the local Chern marker operator as $4\pi\mathrm{Im}(P\hat{x}P\hat{y})$. For

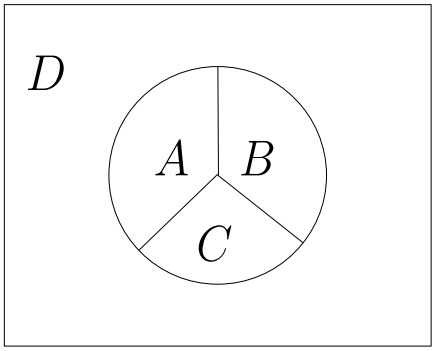

Figure 2.1: Schematic of the partition for the defining Kitaev's real-space Chern number

translationally invariant systems, $\mathcal{C}$ is same for every unit cell. So, when if we consider a supercell, then we just need to divide by the area of the supercell and we get back the same Chern number. But one cannot supercell to be the whole lattice as position operators are not well defined due to periodic boundary conditions(PBC). For open boundary conditions(OBC), when we trace over the entire lattice, we see that $\mathcal{C} = -2\pi i \,\mathrm{Tr}[P\hat{x}P, P\hat{y}P] = 0$ as the trace of commutator is zero. This is intuitive as the global topology is trivial in the case of OBC. However, the topology and bulk is not dependent on the boundary conditions. So, for a system with well-defined bulk and boundary, in OBC one can decompose the contribution to the Chern number $-2\pi i \,\mathrm{Tr}[P\hat{x}P, P\hat{y}P] = 0 = \mathcal{C}_{bulk} + \mathcal{C}_{edge}$ and recover the Chern number of the bulk [BR11].

Another formulation of the real-space Chern number is given by Kitaev [Kito6], which has been used in the literature to characterize the topological phases in self-similar systems. Here we only highlight the main ideas. The details of the derivation can be found in Ref. [Kito6]. The real-space Chern number is defined in terms of tri-partition of a region as

$$\mathcal{C} = 12\pi i \,\mathrm{Tr}(PAPBPC - PAPCPB) \tag{2.12}$$

where P is the projector onto the occupied states and A, B and C are the spatial projectors to the corresponding regions marked in Fig. 2.1. The key idea here that this quantity is not sensitive to the points away from the triple contact point of the tri-partition if the P decays exponentially, which is the case for the gapped bands [FZG23]. As a result, the real-space Chern number does not depend on the exact regions A,B and C. So, one can deform the region freely away from the triple contact point. In the case of infinite systems, one can extend the boundaries of the circle in Fig. 2.1 all the way to infinity. In that case, $A + B + C = 1$ and the real-space Chern number can be expressed as $\mathcal{C}(P, A, B) = 4\pi i \,\mathrm{Tr}([PAP, PBP])$. One can also make use of freedom of choice of A and B and calculate the real-space Chern number for different topological configuration. For a configuration, where $A = \Pi_{x_0}$

is the projection on to the left of $x = x_0$ and $B = \Pi_{y_0}$ is the projection onto the bottom of of $y = y_0$, the real-space Chern number can be expressed as

$$\mathcal{C}(P, \Pi_{x_0}, \Pi_{y_0}) = 2\pi i \operatorname{Tr}\big([P\Pi_{x_0}P, P\Pi_{y_0}P]\big) = 2\pi i \operatorname{Tr}\big(P[[\Pi_{x_0}P], [\Pi_{y_0}P]]\big) \tag{2.13}$$

[Kito6]. Notice that in this case, the half-planes, whose spatial projectors are Π_{x_0} and Π_{y_0}, are defined to have a sharp boundary. For translationally invariant systems, one can deform these sharp boundaries to make it linear and then by replacing $\Pi_{x_0} \to \hat{x}$ and $\Pi_{y_0} \to \hat{y}$, we recover the expression in Eq. (2.11) with a minus sign, which is just an artifact of the definition.

There are other real-space formulations of the Chern number like the Bott-Index and the Localizer index [LH10; Lor19] which we do not cover here. Local decomposition of the real-space Chern number by Kitaev will be discussed in Chapter. 4.

2.3 EDGE STATES AND THE BULK-BOUNDARY CORRESPONDENCE

One of the immediate consequences of the presence of gapped bulk with non-zero Chern number is the appearance of robust states in the gap when one introduces an edge or interface in the system. This is one of the most common signatures of topologically non-trivial systems. The main idea is the following. Let us consider an interface between two systems which have different Chern numbers. We assume both systems to have a gapped bulk. So as one moves from one system to the other through the interface the Chern number changes. However, being a topological invariant, the Chern number cannot change as long as the gap remains open. This automatically implies that the bulk gap must close at the interface leading to the presence of gapless states. These gapless states must be localized at the interface as both the systems have a gapped bulk away from the interface. This idea also applies to the case for finite systems which have a topologically non-trivial bulk away from the edges. The edges can be considered as an interface between a topologically non-trivial gapped system and vacuum, which is trivial by definition with zero Chern number. This leads to the presence of gapless states at the edge. These states cannot be destroyed as long as the bulk-gap remains open, making them robust to the presence of small local disorders.

The bulk-boundary correspondence is the statement that in the absence of additional symmetries, the number of edge modes equals to the difference in the Chern number at the interface. Here, we follow the derivation presented in Ref. [FJK11] and deomnstrate this for a simple two band gapped Hamiltonian H. Without the loss of generality, we further assume it to be spectrally flat with eigenvalues ± 1, as any gapped two band Hamiltonian can be continuously deformed into one which is spectrally flat. Ler the

spectral projector on to the band with energy -1 be called P. So, we have $H = 1 - 2P$. A boundary can be introduced in this by defining

$$H_e = PV(x)P + 1 - P; \begin{cases} V(x) = 1 & \text{if } x \leq 0 \\ V(x) = -1 & \text{if } x > 0 \end{cases} \tag{2.14}$$

such that $H_e = 1$ (trivial) for $x \leq 0$ and $H_e = H$ for $x > 0$, modeling an interface of the system with the vacuucm. Notice that H_e has decays exponentially with x as P decays exponentially and $V(x)$ is local. To see the bulk-boundary correspondence, we start with the real-space formulation of the Chern number given in Eq. (2.13). Given that we have translational invariance along y, we deform the boundary of the one of the half-planes, $\Pi_{y_0} \to \hat{y}$. Using the identity $-i[\hat{y}, P_{k_y}] = \partial P_{k_y}/\partial k_y$ and replacing the sum as integrals, we get that

$$\mathcal{C} = \int dk_y \, \mathrm{Tr}\, \mathcal{C}(k_y), \tag{2.15}$$

where $\mathcal{C}(k_y) = P_{k_y}[[\Pi_{x_0} P_{k_y}], \partial P_{k_y}/\partial k_y]$. Eq. (2.15) is then evaluated in the eigenbasis $\{|\psi_n\rangle\}$ of $P_{k_y} V(x) P_{k_y}$ with eigenvalues $\{\lambda_n\}$ and We have

$$\langle \psi_n | \mathcal{C}(k_y) | \psi_n \rangle = \partial(1 + \lambda_n)/2\partial k_y.$$

So, $\mathcal{C} = \sum_n (\lambda_n(2\pi) - \lambda_n(0))/2$. Now if k is the number of edge-modes that cross the Fermi level, then we have $\lambda_n(2\pi) = \lambda_{n+k}(0)$ independent of n. As a result, $\lambda_n(2\pi)$ and $\lambda_{n+k}(0)$ keep getting cancelled when taking he sum over n, resulting in $\mathcal{C} = k$. This demonstrates, that the bulk Chern number of a system is equal to the number of edge-modes present in the system when the system posses an interface with vacuum.

2.4 AN EXAMPLE: THE HARPER-HOFSTADTER MODEL

The Harper-Hofstadter model is essentially a tight-binding description of free electrons on a 2-dimensional lattice in the presence of uniform perpendicular magnetic field. This model has been extensively studied in the literature on various lattices [Hof76; Ram85; Pra16]. Here, we choose to work on square lattice. The Hamiltonian is given by:

$$H_{HH} = -\sum_{<jk>} e^{-i\theta_{jk}} c_j^\dagger c_k \tag{2.16}$$

where j, k are the labels for the sites positioned at $\vec{r}_j$ and $\vec{r}_k$, $< \ldots >$ denotes nearest-neighbors, $c_j^\dagger(c_j)$ is the creation (annihilation) operator for state $|i\rangle$, and $\theta_{jk} = (2\pi e/h) \int_{\vec{r}_k}^{\vec{r}_j} \vec{A} \cdot \vec{dl}$, is the Peierl's phase associated with the bond between sites at positions $\vec{r}_j$ and $\vec{r}_k$ with the flux quantum $\phi_0 = h/e$. The physics is invariant with respect to the choice of gauge. what decides the physics is the amount of flux which is piercing through each

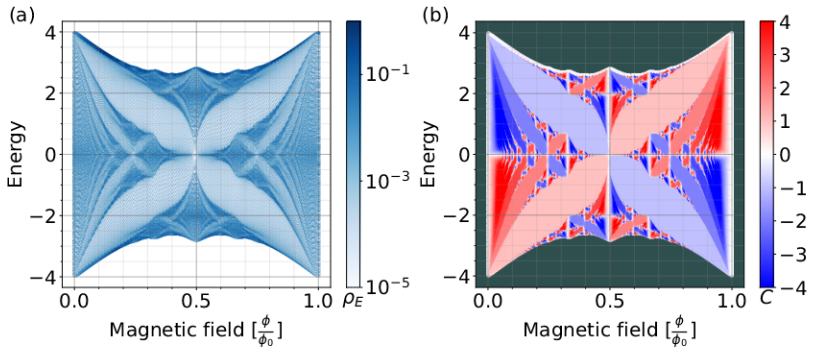

Figure 2.2: Spectra of the Harper-Hofstadter model as a function of the magnetic flux ϕ. (a) shows the normalized density of states which takes the shape of the well-known Hofstadter butterfly. (b) shows the Chern number computed for various filling as a function of the magnetic flux. The computations have been done on a square lattice with $N_{sites} = 341$.

plaquette. For all the numerical calculations, we have used the Landau gauge, $\vec{A} = (0, Bx, 0)$. We have parameterized the magnetic strength by $B = 2\pi\phi/a^2$, where a is the lattice spacing and $2\pi\phi$ is the flux piercing through the smallest triangles of the structures.

We can define a magnetic version of the Brillouin zone whenever ϕ is a rational multiple of ϕ_0, $\phi = p\phi_0/q$ for some integers p and q such that they share no common factors. The gauge invariant translation operator, T_x along the x direction, and T_y along the y direction, do not commute with each other. However, in the Landau gauge which we have chosen, T_x and T_y^q do commute with each other and the Hamiltonian. As a result, a magnetic Brillouin zone can be constructed by grouping q sites together along the y direction to form a larger unit cell. The magnetic Brillouin zone hence a torus, which is q times smaller than the original Brillouin zone, and the spectrum at $\phi = p\phi_0/q$ breaks into q sub-bands. The spectra of the model as function of ϕ results in the famous Hofstadter butterfly shown in Figure. 2.2 (a). To study the spectrum, we look at the normalized density of states ρ_E, which is given by

$$\rho_E(E) = \sum_n \frac{1}{N}\delta(E - E_n) = \sum_n \frac{1}{N\pi} \lim_{\varepsilon \to 0} \frac{\varepsilon}{(E - E_n)^2 + \varepsilon^2} \tag{2.17}$$

where N is the total number of eigenstates and n denotes the index of each eigenstate. In this case, we have used open boundary conditions as a result of which we do not see the gaps in the spectra. Instead, we see the presence of the gapless edge modes. In Fig. 2.2, the regions with low ρ_E correspond the gapless modes and the regions of high ρ_E correspond to the magnetic sub-bands. Fig. 2.2 shows the Chern number as a function of filling and magnetic field. We see that the Chern number is quantized when the Fermi level is in the regions with low ρ_E which otherwise would have been the gaps under periodic boundary conditions.

In this chapter, we looked into some of the defining aspects of topology in non-interacting condensed matter systems. We have not reviewed the role symmetries on the topological aspects of non-interacting systems which we briefly talk about in Section. 5.1. In the next chapter, we will review the tight binding models on self-similar systems, ultimately covering the study of the self-similar structures on fractals.

3

NON-INTERACTING MODELS ON FRACTALS

In this chapter, we present the concepts which are necessary to motivate the main ideas of this work and would be used in the subsequent chapters of this thesis. Specifically, we present a scheme to construct self-similar graphs from fractals, study simple tight binding models using these graphs, and show how the idea of real space renormalization can be inherently associated with these graphs. Then we specifically review two of the works form the literature: (i) properties of tight binding models on the Sierpinski triangles, and (ii) the Sierpinski-Hofstadter model and the associated self-similar chiral *edge-like* states.

We start out with presenting a description of non-interacting particles on fractals. We only choose self-similar fractals for our purpose. Non-interacting finite systems, in general, can be described using a Hamiltonian of the form:

$$\hat{H} = \sum_{jk} H_{ij} \left|i\right\rangle \left\langle j\right| \tag{3.1}$$

where, $\{\left|i\right\rangle\}$ denotes an orthonormal basis in the Hilbert space and H_{ij} are elements of a Hermitian matrix, H. Any Hamiltonian of the from given in Eq. (3.1) can be diagrammatically represented as graph, where the basis states $\left|i\right\rangle$ are represented as vertices or nodes of the graph. The edges of the graph is then defined using the matrix H; there exists an edge between $\left|i\right\rangle$ and $\left|j\right\rangle$ with weight H_{ij} if $H_{ij} \neq 0$. Such graphs often are insightful representations of non-interacting systems. For example, in the tight-binding approximation for crystalline systems, the graph of the Hamiltonian can be directly mapped onto the lattice structure when the basis of representation is chosen to be basis of atomic orbitals present in the system. This in turn allows us to correlate the lattice geometry and the Hamiltonian in such systems. In the case of fractals, presently we do not have a well-defined way to describe systems in the continuum limit. So, we would start out by assuming a tight-binding description of fractal systems, and hence shift our focus towards generating self-similar graphs from fractals.

3.1 CONSTRUCTION OF SELF-SIMILAR GRAPHS

To generate self-similar graphs from fractals, we make use of the iterative scheme of construction of fractal structures. We first explain this using the Sierpinski Gasket (SG), and later generalize it to construct a variety of graphs corresponding to fractals of different generations.

For the construction of graphs on SG, we use a recursive procedure the starting from an equilateral triangle. We divide it into four equilateral tri-

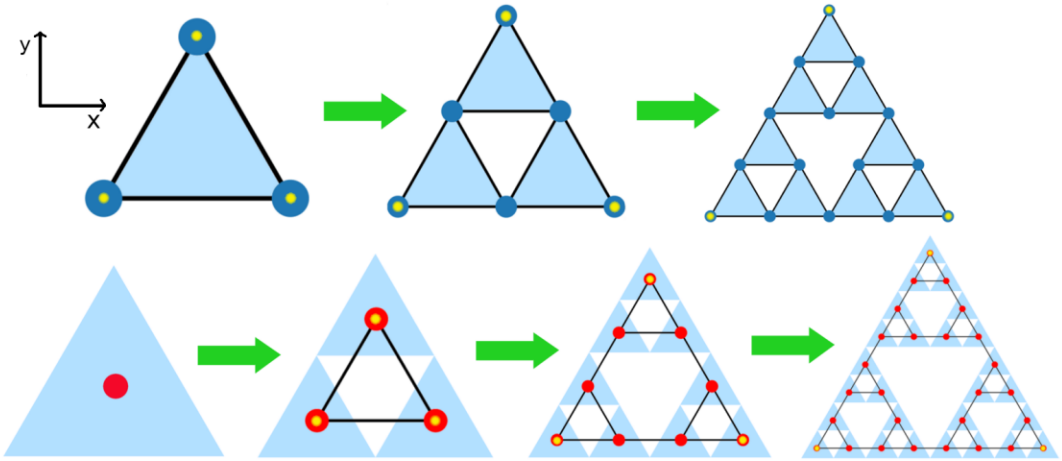

Figure 3.1: Schematics for the construction of the self-similar structures. These structures are constructed by discretizing the recursive generation scheme of the Sierpinski Gasket. The shaded regions are the finite truncations of the SG for different generations. The blue and red dots indicate the positions of the sites for the structures SG-4 and SG-3, respectively. The black solid lines represent the bonds between the sites. The three corner sites are marked with an additional yellow dot in both structures.

angles of equal area, remove the central triangle, and repeat the procedure infinitely for each of the remaining triangles. We call the structure generated after g iterations for "SG with generation g", and the triangles removed in a particular generation as the "triangles of a generation g". It is then possible to construct various graphs on the SG, but for simplicity we choose to focus on self-similar graphs which are equicoordinated, except at the corner sites. We construct self-similar graphs with coordination numbers 3 and 4 as illustrated in Figure. 3.1, but we have not found equicoordinated graphs with other coordination numbers (graph with coordination number zero is trivial).

To construct an 4-coordinated graph (shown in Figure. 3.1), we identify the vertices of the triangles in each generation of the SG with the sites, and the edges with the bonds. This gives a self-similar graph in which, all sites except the three corner sites (marked in yellow in Figure. 3.1), have coordination number 4. We denote this structure by "SG-4". Tight-binding models on this type of structure have been extensively studied using real space renormalization methods (to be discussed later in this chapter).

Similarly, for the construction of an 3-coordinated graph (also shown in Figure. 3.1), we identify the centroids of the smallest triangles in each generation of the SG with the sites, and connect the nearest neighbors. This gives a self-similar graph where, in each generation, all sites except the three corner sites, have coordination number 3. We denote this structure by "SG-3". Notice that the first generation of the SG-4 is obtained from the zeroth generation of the SG, whereas the first generation of the SG-3 is

obtained from the first generation of the SG.

We can generalize this construction scheme to generate fractals and self-similar graphs from other structures. For example, we can generate a fractals of different dimensions from a square. We take a square, divide it into L^2 equal squares, retain K of those squares and remove the rest, and recursively carry out the procedure on the retained squares. This gives a fractal of Hausdorff dimension $\log(K)/\log(L)$. Now to construct self-similar graphs, we follow the procedure as in the case of SG-3. We identify the centres of the squares are the sites and then connect the nearest neighbors with edges. Finite truncations of such structures are said to be of generation g if the recursion scheme is truncated after the g^{th} iteration. A couple of examples of self-similar graphs generated from this scheme is shown in Figure. 3.2 ((a) and (b)). We note that, not all possible fractals generated from this scheme lead to connected self-similar graphs. One of such cases is shown as an example in Figure. 3.2(c).

3.2 SELF-SIMILARITY AND REAL-SPACE RENORMALIZATION

The self-similar nature of the graphs constructed using the above construction scheme ensures that, for each graph, we can remove certain specific sites from a given generation g so that the structure with the remaining sites resembles that of generation $g-1$. For each structure, we term these specific sites as the 'sites of generation g'. One such example is illustrated in Fig. 3.3. In both structures shown in the example, in each generation, only the three corner sites of the SG-3 and the SG-4 are two coordinated, but we expect this to not affect the physics when we are far from the corner sites. In this section, we show how the self-similarity of some of these graphs, like those from the Sierpinski Gasket, leads to the construction of exact real-space renormalization and later go on to use the renormalized Hamiltonian for solving the tight-binding model on SG-4 as an example. Several works in the literature make use of these scheme for studying self-similar systems [Dom+83; RT82; BKP85; Ghe+87]. Here we will primarily follow the review of all these works by [Kim98].

Consider a Hamiltonian H represented by the self-similar graph of generation g. In some self-similar graphs, the fact that one can remove the sites of generation g to obtain a graph of generation $g-1$ implies that one can H can renormalized to a new Hamiltonian H' defined on the sites of $g-1$ with exactly the same structure. To see this, let us first denote the set of sites of generation g as the Q and the set of rest of the sites as P. Let $\mathcal{P}$ and $\mathcal{Q}$ be the projectors onto sites in P and Q respectively. So the eigenvalue equation for H can be decomposed in terms of sites in P and Q and can be written as

$$H|\Psi\rangle = \begin{bmatrix} H_{PP} & H_{PQ} \\ H_{QP} & H_{QQ} \end{bmatrix} \begin{bmatrix} \Psi_P \\ \Psi_Q \end{bmatrix} = \begin{bmatrix} H_{PP}\Psi_P + H_{PQ}\Psi_Q \\ H_{QP}\Psi_P + H_{QQ}\Psi_Q \end{bmatrix} = E \begin{bmatrix} \Psi_P \\ \Psi_Q \end{bmatrix}, \quad (3.2)$$

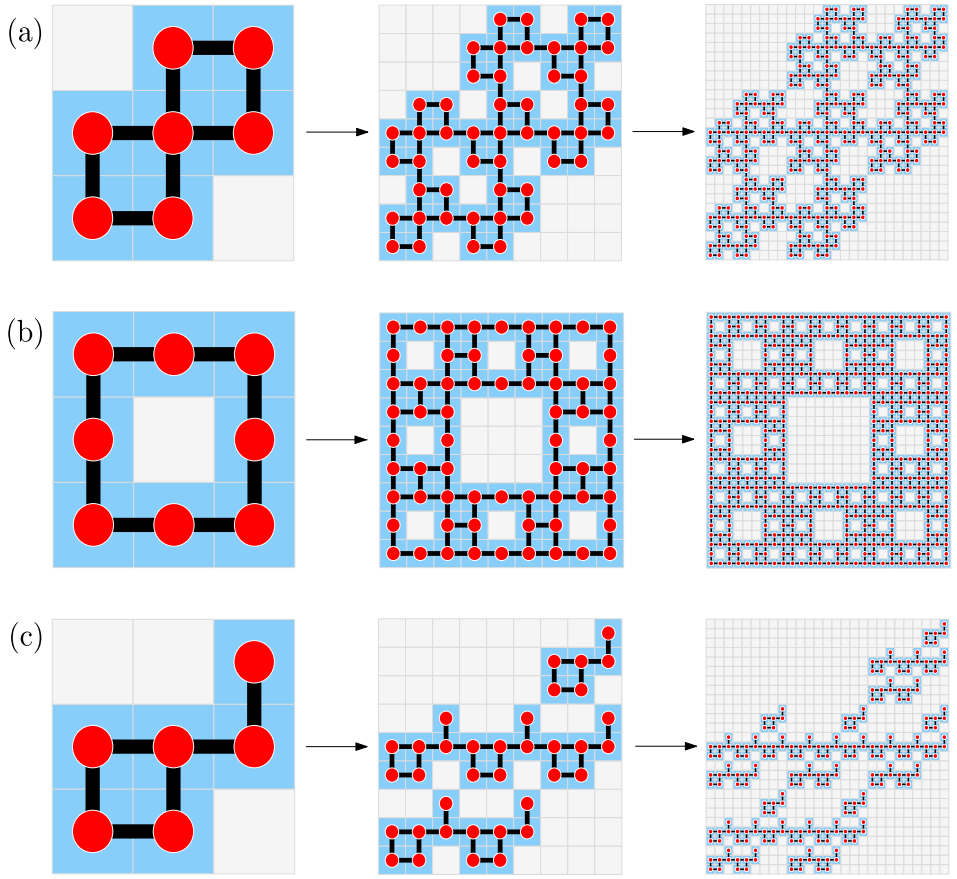

Figure 3.2: Few examples of graphs constructed using the recursive scheme on a square. (a) and (b) are examples of self-similar graphs. (a) is a graph made from a fractal with Hausdorff dimension $\frac{\log(7)}{\log(3)}$, whereas (b) is constructed from the well-known Sierpinski Carpet with Hausdorff dimension $\frac{\log(8)}{\log(3)}$. (c) is an example of a case where the applying the recursive scheme does not result in a connected graph.

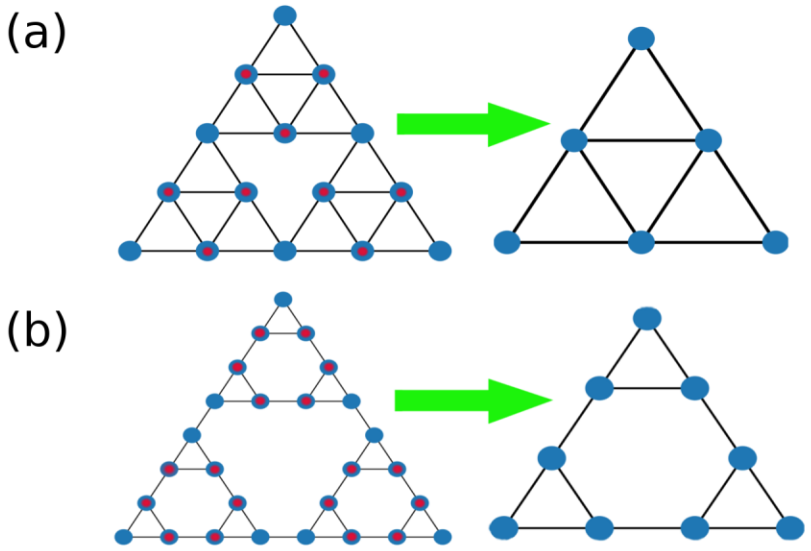

Figure 3.3: Schematics showing the self-similarity of (a) SG-4 and (b) SG-3. The sites of the third generation are marked in red for both structures. When these sites are removed, the remaining structure resembles that of the second generation.

where the eigenstate $|\Psi\rangle \equiv [\Psi_P, \Psi_Q]^T$ and E is the eigenvalue. The idea is to now eliminate Ψ_Q and rewrite the whole equation in terms of Ψ_P. This can be done by expressing Ψ_Q in terms of Ψ_P and E as following

$$\Psi_Q = (E - H_{QQ})^{-1} H_{QP} \Psi_P \tag{3.3a}$$

$$H_{PP}\Psi_P + H_{PQ}(E - H_{QQ})^{-1} H_{QP}\Psi_P = E\Psi_P \tag{3.3b}$$

. We see that Eq. (3.3b) is an eigenvalue equation written completely in terms of sites in P. So the renormalized Hamiltonian H' can be identified as

$$H' = H_{PP} + H_{PQ}(E - H_{QQ})^{-1} H_{QP}, \tag{3.4a}$$

$$\langle i_P|H'|j_P\rangle = \langle i_P|H|j_P\rangle + \sum_{l,m} \langle i_P|H|l_Q\rangle \langle l_Q|(E - H_{QQ})^{-1}|m_Q\rangle \langle m_Q|H|j_P\rangle, \tag{3.4b}$$

where $i_P, j_P \in P$ and $l_Q, m_Q \in Q$. In principle, every system can be decomposed into some set of sites, Q, and its compliment P, and one can write an effective renormalized Hamiltonian H' for sites in P. However H' does not have the same structure as H in general. What makes H' to have the same structure as H are the following additional structures of H_{QQ}. Consider the condition where the sites in Q can be regrouped in to different disjoint subsets Q_i such that there does not exist a path between $q_i \in Q_i$ and $q_j \in Q_j$ when restricted to only the sites in Q. This ensures that H_{QQ} has a block-diagonal form $H_{QQ} = \text{diag}(W_1, W_2, \ldots)$ such that W_i acts only on sites in Q_i. As a result, $(E - H_{QQ})^{-1}$ also has a block diagonal form given by $(E - H_{QQ})^{-1} = \text{diag}((E - W_1)^{-1}, (E - W_2)^{-1}, \ldots)$. This means that $(E - H_{QQ})^{-1}$ does not 'connect' sites in subset Q_i with sites in subset Q_j for any i, j. Moreover, for any subset Q_i, let the set of sites in P

which are connected to those in Q_i be named P_i. If for any two $p_x, p_y \in P_i$, there always exists an edge between them in the graph of generation $g-1$, then $\sum_{l,m} \langle i_P|H|l_Q\rangle \langle l_Q|(E-H_{QQ})^{-1}|m_Q\rangle \langle m_Q|H|j_P\rangle$ cannot generate any additional edges which are not already present in the structure of $g-1$. This implies that H' (if it exists) will have the same structure as H, except that the onsite potentials and the hopping matrix elements gets renormalized. And due to this preservation of the structure of the Hamiltonian, the renormalization can be repeated arbitrary number of times. The structures given in Fig. 3.3 are examples of the graphs which satisfy these conditions. More mathematical details on the equivalence of H and H' can be found in Ref. [Kim98]. Next we go on to solve a simple tight-binding model on SG-4 as an example.

3.2.1 *Tight-binding model on Sierpinski triangle*

Various non-interacting models have been studied in the literature using real-space renormalization method. Here, we review the properties of simplest tight-binding model on SG-4, which is referred to as 'Sierpinski triangle' in the literature. The model was studied by *Rammal* and independently by *Domanyetal.*, hence it is termed as the $R-D$ model. The graph of the Hamiltonian H is the same as SG-4 (see Fig. 3.3(a) or Fig. 3.1(a)), where $H_{jj} = u$ for all sites j, and $H_{jk} = t$ if j,k are connected by an edge or $H_{jk} = 0$ otherwise. Here, t is considered to be real.

For doing the decimation, we identify the Q sites and P sites as the ones marked in red and blue respectively in Fig. 3.3(a). The set Q can be decomposed as into union of disjoint subsets Q_i as the graph of the sites in Q clearly decomposes into disjoint triangles. So, for the renormalized Hamiltonian H', we have

$$\langle i|H'|j\rangle = \sum_{l,m\in Q_i} \langle i|H|l\rangle \ \langle l|(E-W_i)^{-1}|m\rangle \ \langle m|H|j\rangle\,, \tag{3.5a}$$

$$\langle i|H'|i\rangle = u + 2\sum_{l,m\in Q_i} \langle i|H|l\rangle \ \langle l|(E-W_i)^{-1}|m\rangle \ \langle m|H|j\rangle\,, \tag{3.5b}$$

where $i,j \in P$. The factor of 2 in front of the sum in Eq. (3.5b) is because of the fact that each site in P is present in two P_i. From Eq. (3.5), we that the renormalized hopping and onsite energies are given by

$$t' = t\frac{2-\epsilon}{(\epsilon+2)(\epsilon-1)} \tag{3.6a}$$

$$U' = U\frac{(\epsilon+3)(\epsilon-2)}{(\epsilon+2)(\epsilon-1)}, \tag{3.6b}$$

$$\epsilon' = \frac{U'}{t'} = -\epsilon(\epsilon+3) \tag{3.6c}$$

where $U = u - E$ and $\epsilon = U/t$. The spectrum and the properties of the eigenstates can be studies by inverting Eq. (3.6c) which is given by

$$\epsilon = -\frac{3}{2} \pm \sqrt{\left(\frac{3}{2}\right)^2 - \epsilon'} \tag{3.7}$$

which is referred as the decoration relation in the literature [Kim98]. The spectrum for the infinite generation of SG-4 can be generated by using the eigenvalues of the H on a triangle as seeds. These eigenvalues are 2 and 1. The eigenvalues corresponding to $\epsilon' = 1$ being used as the seed are called edge eigenvalues as this seed corresponds to an energy where the decimation is ill-defined as H' becomes singular. The eigenvalues corresponding to $\epsilon' = 2$ being used as the seed are called isolated eigenvalues. The spectrum of H at infinite generation is basically the set of all such generated eigenvalues along with their limit points. These limit points turn out to be the Julia set [Dom+83]. Important properties of the states on SG-4 in the infinite g limit include the fact that each eigenvalue is infinitely degenerate and every eigenstate can be written as a linear superposition of 'superlocalized' states which only have finite amplitude on a finite number of lattice sites [Dom+83; Kim98].

3.3 EFFECT OF MAGNETIC FIELD AND TOPOLOGY

The tight-binding graphs mentioned in the the previous sections were models to study the free particles on self-similar fractals. It is natural to ask the question: what happens to these free particles when we switch on a magnetic field. To study this problem from a tight-binding perspective on graphs, typically one makes use of the well-known Peierl's substitution. As a result, the hopping amplitudes get modified with an additional phase, $t_{jk} \to e^{i\theta_{jk}} t_{jk}$, where $\theta_{jk} = (2\pi q/h) \int_{\vec{r}_k}^{\vec{r}_j} \vec{A} \cdot \vec{dl}$, q is the charge of the particle, and $\vec{A}$ is the vector potential associated with the magnetic field. Detailed study of the spectral properties of such tight-binding models using the real-space renormalization approach can be found in references [Dom+83; BKP85; Ghe+87; Kim98]. Not only from the perspective of spectral properties, this problem is also interesting from the perspective of topology and the integer quantum Hall effect.

3.3.1 *The Sierpinski-Hofstadter model*

The Sierpinski-Hofstadter model is the application of the Harper-Hofstadter model to study non-interacting electrons on a Sierpinski fractals, in the the presence of uniform magnetic field. As we discussed in the previous section, the topological phases in non-interacting translationally invariant systems are identified by the presence of robust chiral edge(boundary) modes, and

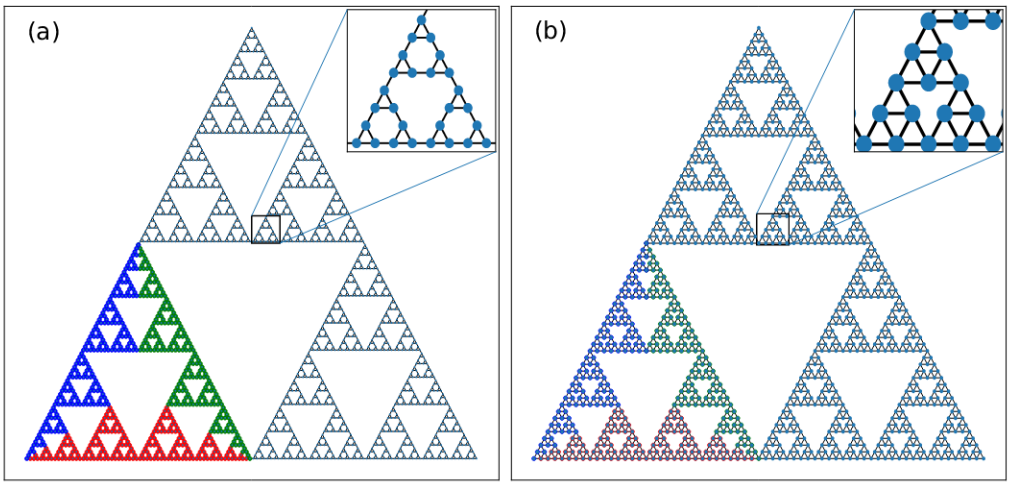

Figure 3.4: (a) SG-3 with $g = 7$, and (b) SG-4 with $g = 7$. For the calculation of the real space Chern number using Eq. (3.9), we choose a subsection of the system and divide it into three partitions. The partitions are shown with red, green and blue and the projectors onto these partitions are labeled $\mathbb{A}$, $\mathbb{B}$, and $\mathbb{C}$ respectively.

are characterized by the Chern number defined in the bulk. So, from a purely physical point of view, we see that idea of a well defined bulk and boundary plays a crucial role in identifying the topological phases in these systems. However, from a purely mathematical point of view, all the above properties are essentially the properties of the tight-binding graphs of these systems. So at this point it is natural to ask what happens if we choose a tight-binding graph of a system which lacks the distinction between bulk and boundary. And self-similar fractals are excellent examples of such systems. In an attempt to answer this, the Sierpinski-Hofstadter model was studied on SG-4 and SC in the reference [BCN18]. Later a few other works explored different properties like the Hall conductivity and robust currents which are some signatures of topological phases, on various fractals [Fis+21; Fre+20; IKY20; SN21].

We consider two different discretizations of the Sierpinski gasket (SG), namely SG-3 and SG-4, mentioned in section 3.1. These two structures have relatively slower growth in the system size N as a function of the generation g. For example, $N = 3^g$ for SG-3 and $N = (3^g + 3)/2$ for SG-4, whereas $N = 8^g$ for a self-similar structure constructed from the Sierpinski Carpet. This makes it comparatively easier to numerically access higher generations and reach closer to the limiting fractional dimension for SG-3 and SG-4. The Hamiltonian for the system is the Harper-Hofstadter Hamiltonian given in Eq. (2.16). The only difference is that, here we have parameterized the magnetic strength by $B = 2\pi\phi/(\sqrt{3}a^2/4)$, where a is the distance between nearest neighbor sites and $2\pi\phi$ is the flux piercing through the smallest triangles of the structures.

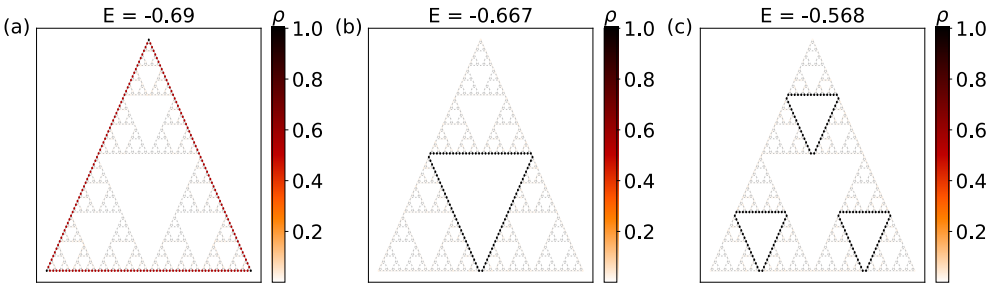

Figure 3.5: Examples of edge-like states for the Sierpinski-Hofstadter model on SG-3. Calculations have been done for $g = 6$.

To study the spectrum, we look at the normalized density of states ρ_E, which is given by

$$\rho_E(E) = \sum_n \frac{1}{N}\delta(E - E_n) = \sum_n \frac{1}{N\pi} \lim_{\varepsilon \to 0} \frac{\varepsilon}{(E - E_n)^2 + \varepsilon^2} \tag{3.8}$$

where N is the total number of eigenstates and n denotes the index of each eigenstate. Given a state $|\psi\rangle = \sum_j \psi_j |\mathbf{r}_j\rangle$, we study the localization of the state by computing the normalized onsite density, $\rho_j = |\psi_j|^2 / \max(|\psi_j|^2)$.

The Harper-Hofstadter model on the SIerpinski Gasket gives rise to some exotic states which were not present in the case of translationally invariant lattice systems [BCN18; SN23]. These states appear to be highly localized on some particular sites of SG-3 and SG-4, which seem to look like analogous to the edge states found in the topological lattice systems. A few examples of such states are shown in Figure. 3.5. However, due to self-similarity, the notion of bulk and edge is ill-defined on fractals. And due to this lack of sharp distinction between bulk and edge states in the case of fractal systems, we define "bulklike" and "edgelike" states as follows. An eigenstate is a bulklike state if it has finite probability density on sites which enclose the triangles belonging to more or less every generation of the SG. On the other hand, an eigenstate is an edgelike state, if it is localized on sites which enclose the triangles belonging entirely to a particular generation of the SG.

We also calculate the real space Chern number for different fillings using Kitaev's prescription [Kito6] given by

$$C(P) = 12\pi \mathrm{i}(\mathrm{Tr}(\mathbb{A}P\mathbb{B}P\mathbb{C}P) - \mathrm{Tr}(\mathbb{A}P\mathbb{C}P\mathbb{B}P)) \tag{3.9}$$

where $\mathbb{A}, \mathbb{B}, \mathbb{C}$ are the projections onto the three partitions shown in Fig. 3.4, and $P = \sum_{n \in occ} |n\rangle \langle n|$ is the projector onto the set of occupied eigenstates. The normalized density of states and the Chern numbers as a function of the magnetic field are shown in Fig. 3.6. It is immediately clear from Fig. 3.6 that most of the spectrum has a very low ρ_E. This is significantly different from the Hofstadter butterfly on lattices with open boundary conditions which have well-defined bulk regions (high ρ_E) and edge regions (low ρ_E) in the spectrum. Moreover, for both SG-3 and SG-4, almost the entire region

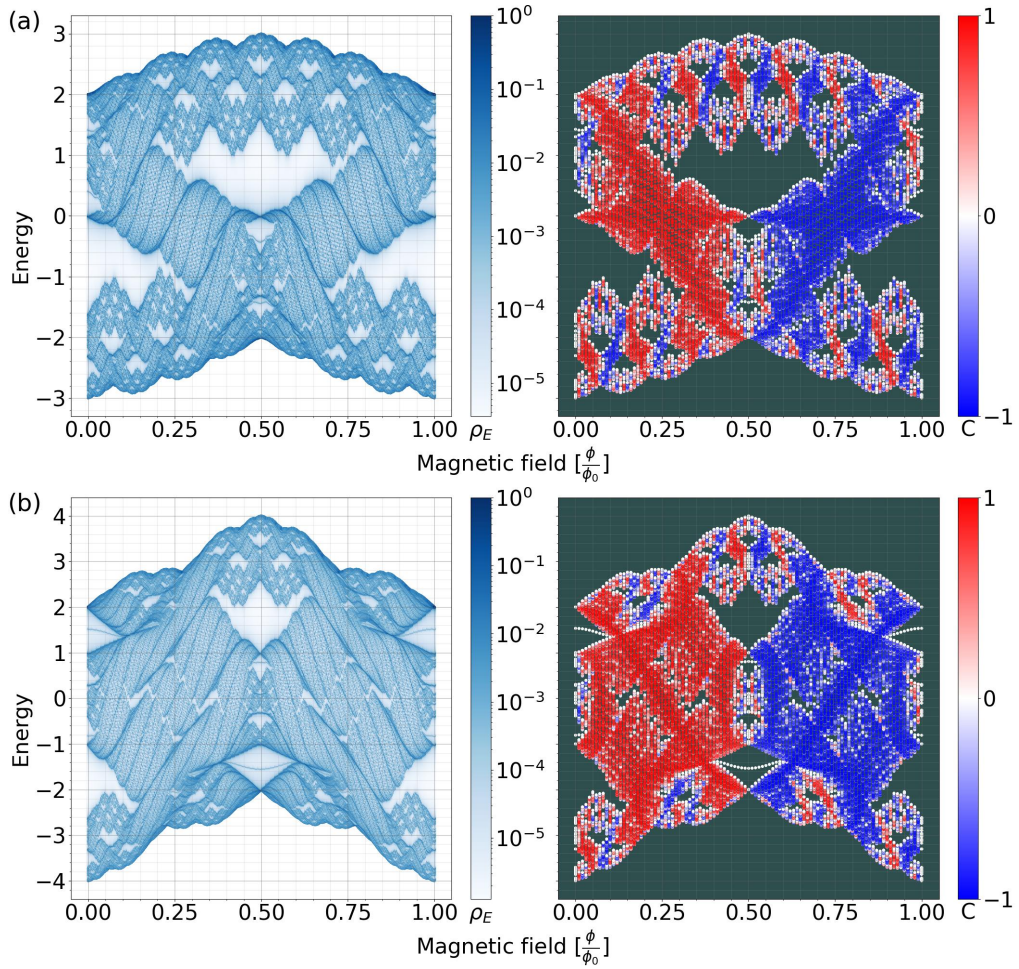

Figure 3.6: Density of states and the real space Chern number for (a) SG-3, $N = 3^6$ and, (b) SG-4, $N = (3^7 + 3)/2$. The density of states, ρ_E, is computed using Eq. (3.8) with $\varepsilon = 10^{-3}$ and the Chern number is computed using Eq. (3.9).

with low ρ_E is characterized by $C = \pm 1$.

3.4 OUTLOOK

Recently, significant developments have been made in the study of quantum fractals in photonic waveguides[Yan+20] and in the experimental realization of quantum fractals within controlled laboratory settings [Xu+21]. This has ignited a surge of theoretical studies in this domain [Iva+22; Zhe+22; MNR22] which is driven by the possibility of self-similar quantum systems to yield profound theoretical insights and unveil the potential for discovering exotic phenomena previously uncharted in conventional condensed matter physics. As we move into the next chapter, we're diving deeper into this exciting field. We'll build on what we've learned so far, zoom in on these self-similar structures and provide a way to understand the topological phases on these structures.

Part II

NON-INTERACTING MODELS

In this part, we present our study of the topological phases in non-interacting models on self-similar structures. In the first chapter of this part, we present our understanding of topological phases in terms of adiabatic charge pumping which is primarily based on our work in Ref. [SN23]. The second chapter in this part is based on our works in Ref. [SN21], we show the effect of the interplay of non-spatial symmetries and coordination on the topological phases on these structures.

4

TOPOLOGY THROUGH ADIABATIC CHARGE TRANSPORT

Topological phase diagrams of some well-known models on self-similar structures are present in the literature [Aga19; BCN18; SN21]. The Sierpinski-Hofstadter model, which we reviewed briefly in the previous chapter, is an example of one such model. However, only a limited microscopic understanding of such phases is available at present. For example, in the case of self-similar structures, understanding of these topologically nontrivial phases in terms of winding of the eigenstates over some manifold, analogous to the winding of the Bloch states in the k space for translationally invariant non-interacting systems, is not present at the moment. Given the lack of an eigenstate winding perspective for self-similar structures, we use the perspective of adiabatic charge pumping in this chapter to understand the emergence of topology in self-similar systems and the quantization of real-space indices. Adiabatic pumping in translationally invariant non-interacting systems has been thoroughly studied. These systems form multiple magnetic bands (or Landau levels in the continuum case) when subjected to a perpendicular magnetic field. When additional flux is threaded through the system using a thin long solenoid, some states flow across the band gap from one band to another. The Chern number can be expressed as the number of such states flowing across the band gap. In this chapter, we study whether similar ideas can be used to present a microscopic understanding of the topology in self-similar systems.

4.1 ADIABATIC CHARGE TRANSPORT IN TERMS OF INSTANTANEOUS PROJECTORS

We consider a finite non-interacting system, $\mathcal{S}$, with a Hamiltonian, $H(\varphi(t))$, where $\varphi(t)$ is a time dependent parameter. We assume that the Hamiltonian has no other explicit time dependence and from now on, in this section, we suppress the time dependence of the parameter. The instantaneous eigenstates can be obtained from the eigenvalue equation

$$H(\varphi)\,|n(\varphi)\rangle = E_n(\varphi)\,|n(\varphi)\rangle\,. \tag{4.1}$$

We assume that there is a time $t = T$ after which the Hamiltonian returns back to itself, up to a gauge transformation. We now consider a subsystem, $\mathcal{B}$, of the system. The rest of the system is denoted by $\mathcal{S} - \mathcal{B}$. We want to quantify the net charge, Q, leaking out of the subsystem over a time period when the system is adiabatically evolved in time. Q is given by

$$Q = \int_0^T \langle J \rangle \, dt, \tag{4.2}$$

where J is the current operator and $\langle\rangle$ is the expectation value of the operator in the many-body ground state wave-function at time t. In the adiabatic limit, each single particle eigenstate of the Hamiltonian $H(\varphi(t))$ evolves as

$$|n(\varphi(t))\rangle = e^{i\theta_n(t)} e^{i\gamma_n(t)} |n(\varphi(0))\rangle , \tag{4.3}$$

where $\theta_n(t) = -(1/\hbar)\int_0^t E_n(\varphi(t'))dt'$ is the dynamical phase and $\gamma_n(t) = \int_0^t i\langle n(\varphi(t'))|\dot{n}(\varphi(t'))\rangle\, dt'$ is the geometrical phase. So the many-body time-evolved state in the adiabatic limit, $|\Omega(t)\rangle$, is the Slater determinant of the adiabatically time-evolved occupied single particle states.

The current operator can be identified from the change of the total number operator over subsystem, $\mathcal{B}$, which is given by the von Neumann equation

$$\frac{\partial \langle n_{\mathcal{B}}\rangle}{\partial t} = -i\langle [n_{\mathcal{B}}, H(\varphi)]\rangle , \tag{4.4}$$

where $n_{\mathcal{B}} = \sum_{b\in\mathcal{B}} |\mathbf{r}_b\rangle\langle\mathbf{r}_b|$ is the total number operator over $\mathcal{B}$. Then we identify the current operator as $J = -i[n_{\mathcal{B}}, H(\varphi)]$. In the case of adiabatic evolution, the time-evolution can be generated by the adiabatic Hamiltonian, $K(t) = i[\dot{P}_I, P_I]$, instead of H [dBL22]. Here $P_I = \sum_{n(\varphi)\,\in\, occ} |n(\varphi)\rangle\langle n(\varphi)|$ is the instantaneous projector onto the set of occupied single particle states. The derivation of the adiabatic Hamiltonian, K, can be found in appendix A of Ref. [dBL22]. So, the adiabatic current operator is given by

$$\begin{aligned} J^A &= -i[n_{\mathcal{B}}, K(t)] \\ &= (n_{\mathcal{B}}\dot{P}_I P_I + P_I\dot{P}_I n_{\mathcal{B}} - n_{\mathcal{B}} P_I\dot{P}_I - \dot{P}_I P_I n_{\mathcal{B}}). \end{aligned} \tag{4.5}$$

The expectation value of the adiabatic current operator in the many-body ground state then becomes

$$\begin{aligned} \left\langle J^A \right\rangle &= \langle\Omega(t)|J^A|\Omega(t)\rangle = \mathrm{Tr}(P_I J^A) \\ &= \mathrm{Tr}(P_I n_{\mathcal{B}}\dot{P}_I P_I) + \mathrm{Tr}(P_I^2\dot{P}_I n_{\mathcal{B}}) \\ &- \mathrm{Tr}(P_I n_{\mathcal{B}} P_I\dot{P}_I) - \mathrm{Tr}(P_I\dot{P}_I P_I n_{\mathcal{B}}) \\ &= \mathrm{Tr}(n_{\mathcal{B}}\dot{P}_I P_I) + \mathrm{Tr}(P_I\dot{P}_I n_{\mathcal{B}}) \\ &- \mathrm{Tr}(n_{\mathcal{B}} P_I\dot{P}_I P_I) - \mathrm{Tr}(P_I\dot{P}_I P_I n_{\mathcal{B}}), \end{aligned} \tag{4.6}$$

where the last equality has been obtained by using the cyclic property of the trace and the fact that $P_I^2 = P_I$. Now we use the identity $P_I\dot{P}_I P_I = 0$, and we get

$$\begin{aligned} \left\langle J^A \right\rangle &= \mathrm{Tr}(n_{\mathcal{B}}\dot{P}_I P_I) + \mathrm{Tr}(P_I\dot{P}_I n_{\mathcal{B}}) \\ &= \mathrm{Tr}(n_{\mathcal{B}}\dot{P}_I P_I) + \mathrm{Tr}(n_{\mathcal{B}} P_I\dot{P}_I) \\ &= \mathrm{Tr}(n_{\mathcal{B}}\dot{P_I^2}) = \mathrm{Tr}_{\mathcal{B}}(\dot{P}_I), \end{aligned} \tag{4.7}$$

where $\mathrm{Tr}_{\mathcal{B}}(..)$ is the trace over degrees of freedom in subsystem $\mathcal{B}$. So the net charge leaking form $\mathcal{B}$ can be expressed as

$$\begin{aligned} Q &= \int_0^T \left\langle J^A \right\rangle dt = \int_0^T \mathrm{Tr}_{\mathcal{B}}(\partial_t P_I) dt \\ &= \mathrm{Tr}_{\mathcal{B}}(P_I(T) - P_I(0)). \end{aligned} \tag{4.8}$$

From Eq. (4.8) we see that, in the adiabatic limit, the net charge leaking from the subsystem can be expressed as the change in the instantaneous projector onto the occupied states over the pumping cycle, traced over the degrees of freedom of the subsystem. Now, as the parameter is assumed to get back to its initial value at time T, the Hamiltonian returns back to itself, up to a gauge transformation. So, the set of projectors onto the eigenstates of the Hamiltonian at $t = 0$, $\{|n(\varphi(0))\rangle \langle n(\varphi(0))|\}$, is the same as the set of projectors onto the eigenstates at $t = T$, $\{|n(\varphi(T))\rangle \langle n(\varphi(T))|\}$. So, if there is no spectral flow due to the change in φ in the instantaneous spectra of the Hamiltonian, $P_I(T) = P_I(0)$ and there is no adiabatic charge transport as a result. Clearly, to get a non-zero adiabatic charge transport from the region $\mathcal{B}$, there must be spectral flow in the instantaneous spectra of the system.

Now let us consider a scenario where $P_I(T) \neq P_I(0)$. Let $\mathcal{N}_i$ be the set of eigenstates which are occupied at $t = 0$ but not at $t = T$, $\mathcal{N}_f$ be the set of eigenstates which are occupied at $t = T$ but not at $t = 0$, and $\mathcal{O}$ be the set of eigenstates which remain occupied both at $t = 0$ and $t = T$. As we have assumed that the system is particle conserving, the number of states in $\mathcal{N}_i$ and $\mathcal{N}_f$ are the same, denoted by N. So, $P_I(0) = \sum_{n\in\mathcal{N}_i} |n\rangle \langle n| + \sum_{o\in\mathcal{O}} |o\rangle \langle o|$ and $P_I(T) = \sum_{m\in\mathcal{N}_f} |m\rangle \langle m| + \sum_{o\in\mathcal{O}} |o\rangle \langle o|$. So, we get

$$\begin{aligned} Q &= \mathrm{Tr}_{\mathcal{B}}(P_I(T) - P_I(0)) \\ &= \mathrm{Tr}_{\mathcal{B}}\Big(\sum_{m\in\mathcal{N}_f} |m\rangle \langle m| - \sum_{n\in\mathcal{N}_i} |n\rangle \langle n|\Big) \\ &= \sum_{m\in\mathcal{N}_f} \mathrm{Tr}_{\mathcal{B}}(|m\rangle \langle m|) - \sum_{n\in\mathcal{N}_i} \mathrm{Tr}_{\mathcal{B}}(|n\rangle \langle n|). \end{aligned} \tag{4.9}$$

If a state $|n\rangle$ is completely localized in $\mathcal{B}$, then $\mathrm{Tr}_{\mathcal{B}}(|n\rangle \langle n|) = 1$, and if it is completely localized in $\mathcal{S} - \mathcal{B}$, then $\mathrm{Tr}_{\mathcal{B}}(|n\rangle \langle n|) = 0$. So, if all states in $\mathcal{N}_f$ and $\mathcal{N}_i$ are completely localized either in $\mathcal{B}$ or in $\mathcal{S} - \mathcal{B}$, then $\sum_{m\in\mathcal{N}_f} \mathrm{Tr}_{\mathcal{B}}(|m\rangle \langle m|)$ and $\sum_{n\in\mathcal{N}_i} \mathrm{Tr}_{\mathcal{B}}(|n\rangle \langle n|)$ would be integers, giving rise to a quantized adiabatic charge Q. Now, if all states in $\mathcal{N}_i$ and $\mathcal{N}_f$ are completely localized in $\mathcal{S} - \mathcal{B}$, then $\sum_{m\in\mathcal{N}_f} \mathrm{Tr}_{\mathcal{B}}(|m\rangle \langle m|) = \sum_{n\in\mathcal{N}_i} \mathrm{Tr}_{\mathcal{B}}(|n\rangle \langle n|) = 0$ and $Q = 0$. Also, if all states in $\mathcal{N}_i$ and $\mathcal{N}_f$ are completely localized in $\mathcal{B}$, then $\sum_{m\in\mathcal{N}_f} \mathrm{Tr}_{\mathcal{B}}(|m\rangle \langle m|) = \sum_{n\in\mathcal{N}_i} \mathrm{Tr}_{\mathcal{B}}(|n\rangle \langle n|) = N$ and $Q = 0$. A non-trivial quantized contribution to the adiabatic charge transport is obtained when a pair of states, $|m\rangle \in \mathcal{N}_f$ and $|n\rangle \in \mathcal{N}_i$, are localized in such a way that one of them is completely localized in $\mathcal{B}$ and the other is completely localized in

$\mathcal{S} - \mathcal{B}$.

4.2 ADIABATIC CHARGE PUMPING IN SIERPINSKI-HOFSTADTER MODEL

We insert an infinitely long, thin solenoid through a given point (x_0, y_0). The flux, $2\pi\varphi$, through the solenoid is then varied adiabatically from 0 to 2π. We are interested in studying the response of the system to the change in flux. To study that, it is important to study the many-body ground state of the system. Since the flux is pumped adiabatically and the Hamiltonian is non-interacting in nature, the many-body ground state of the system at a given instant is the Slater determinant of the occupied single-particle eigenstates of the instantaneous Hamiltonian, $H(\varphi)$, with a dynamical and a geometric phase factor. So we first take a look at the single-particle eigenstates and eigenvalues of $H(\varphi)$. For the rest of the numerics in the text, given a state $|\psi\rangle = \sum_j \psi_j |\mathbf{r}_j\rangle$, the localization is shown by computing the normalized onsite density, $\rho_j = |\psi_j|^2 / \max(|\psi_j|^2)$.

4.2.1 *Instantaneous spectrum and spectral flow*

The form of the Hamiltonian $H(\varphi)$ is the same as in Eq. (2.16), except that an additional Peierl's phase, $\tilde{\theta}_{jk} = (2\pi e/h) \int_{\vec{r}_j}^{\vec{r}_k} \mathbf{A}_\varphi \cdot \mathbf{dl}$, gets added to each bond due to the flux-tube. Here $\mathbf{A}_\varphi$ is the vector potential due to the flux tube, and for the numerical computations, it is taken to be $\mathbf{A}_\varphi = (0, \varphi/r, 0)$ in cylindrical coordinates. The spectrum of $H(\varphi)$ at $\varphi = 0$ and $\varphi = \phi_0$ are identical as the Hamiltonian returns to itself, up to a gauge transformation. In fact, the spectrum is periodic in φ with a period of ϕ_0. But for $\varphi \neq n\phi_0, \quad n \in \mathcal{Z}$, the spectrum of the Hamiltonian changes in general resulting in the flow of the energy of individual eigenstates. We track the flow of the energies of the eigenstates as a function of φ. We say that a given state has undergone a spectral flow if the state does not return back to the same initial energy as φ is changed from 0 to ϕ_0.

Figure 4.1 shows the spectral flow of the Harper-Hofstadter model on SG-3. We would like to highlight the fact that the spectral flow here is qualitatively different from that of the Harper-Hofstadter model on a 2-dimensional lattice. In the case of a 2-dimensional lattice, spectral flow is observed across the band-gap. The states in the bulk undergoing spectral flow move in energy (up or down depending on the Chern number), from one band to the next band, across the gap. The edge states, which lie entirely in the gap, undergo spectral flow in the opposite direction to that of the bulk states (shown in Fig. 4.2(a)). In contrast, in the case of SG-3, spectral flow is observed almost throughout the entire spectrum (in the low ρ_E regions). Here, the states undergoing spectral flow go from one group of degenerate states with low

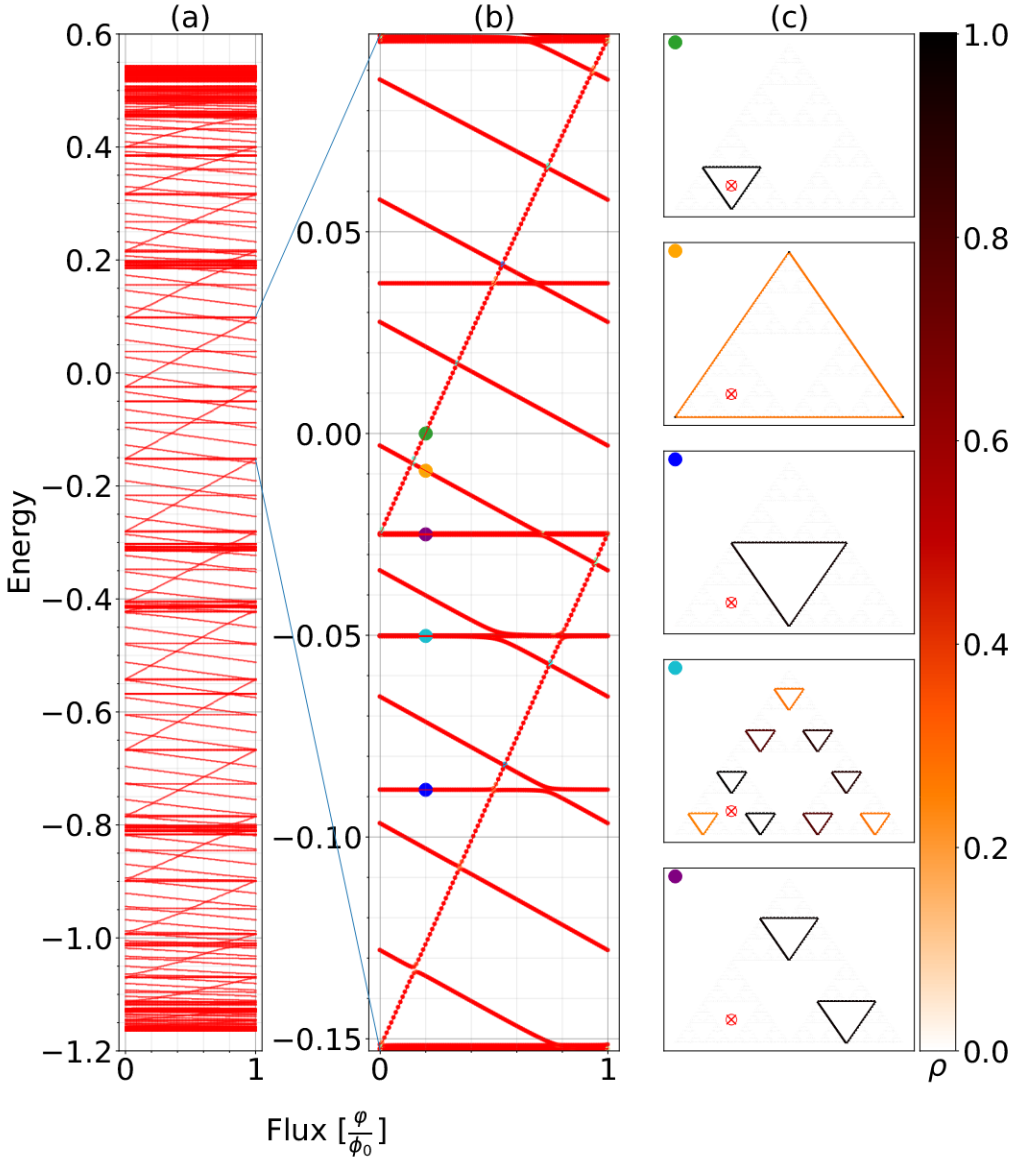

Figure 4.1: Spectral flow for SG-3, $N = 3^7$ with $\phi/\phi_0 = 0.3$. (a) shows the flow of the eigenstates as a function of φ/ϕ_0 for a part of the spectrum. (b) is a zoomed in version of the spectral flow highlighting the nature of the flow. (c) shows the localization of different edge-like states corresponding to different spectral flow (computed at $\varphi/\phi_0 = 0.2$). The coloured dots in (b) represent the points at which the states in (c), marked with corresponding colors, were computed. The position of the flux tube is marked by a red cross-hair on the plots in (c).

degeneracy in the low ρ_E region to another, as opposed to one 'band' to another or one high ρ_E region to another. This qualitative difference in the spectral flow is also observed for other self-similar structures as shown in Fig. 4.2.

The states in the low ρ_E regions of the spectrum can be qualitatively grouped into four groups (column (b) of Fig. 4.1): (I) the states which flow up in energy (positive spectral flow), (II) states which flow down in energy (negative spectral flow), (III) states with almost no change in energy, but are degenerate at $\varphi = 0$ with states undergoing spectral flow, and (IV) states with almost no change in energy and are not degenerate at $\varphi = 0$ with states undergoing spectral flow. We find that the states in group I are edge-like states localized on the sites forming a loop which encloses the flux tube. The states in group II are edge-like states localized on the outermost triangle on SG-3. The states in group III and IV, which do not undergo a spectral flow, are also edge-like states but they are localized on sites forming loops which do not enclose the flux tube. We find that the real space localization is more or less the same for all states belonging to a given group, for low values of φ and sufficiently away form the point of avoided crossings. This means that the states retain their edge-like localization away from the avoided crossings during the spectral flow. The representative real space localization of the states in the above mentioned groups, for a given position of the flux tube, are shown in column C of Fig. 4.1 for these four groups. Close to the avoided crossings, the nature of the states changes due to hybridization.

The extent of hybridization is dependent on the localization of the states; states localized nearby in real-space hybridize strongly in the absence of any symmetry. Here, the states belonging to different groups are edge-like states, localized on sites immediately enclosing triangles of different generations. Hence the extent of hybridization is not significant. This has been checked by fidelity computations, shown in the Fig. 4.3. Fidelity is defined as: $\mathcal{F}_{n,m} = \langle \psi_n(\varphi) | \psi_m(\varphi - \delta\varphi) \rangle$, where $|\psi_n(\varphi)\rangle$ and $|\psi_m(\varphi)\rangle$ are instantaneous eigenstates of the Hamiltonian ($H(\varphi)\,|\psi_n(\varphi)\rangle = E_n(\varphi)\,|\psi_n(\varphi)\rangle$), labeled by labels n, m such that $n > m \implies E_n \geq E_m$. A high value of $\mathcal{F}_{n,m} \approx 1$ means that the state $|\psi_m(\varphi - \delta\varphi)\rangle$ flows to $|\psi_n(\varphi)\rangle$ without significant hybridization when the flux φ is changed by an amount $\delta\varphi$.

Why certain states undergo spectral flow and certain states do not can be understood from their localization. For states belonging to group I and II, the states are always localized on a closed loop enclosing the flux tube. Hence, they are sensitive to flux (Aharonov-Bohm effect) and undergo spectral flow. On the other hand, the states which belong to group III and IV are localized on loops which do not enclose the flux tube. Hence, the vector potential of the flux tube can be effectively gauged out resulting in these states being not sensitive to the flux. As a result, they do not show spectral flow. This becomes further clear from Fig. 4.4 where we show the change in the spectral

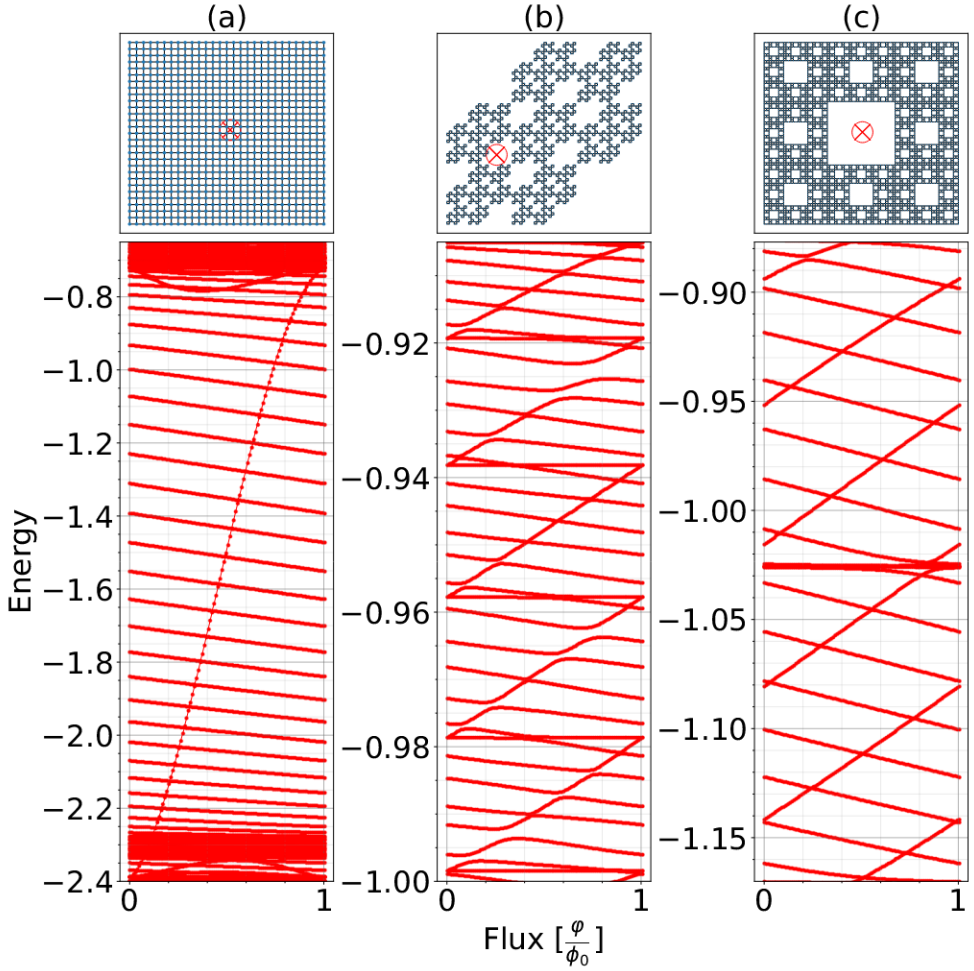

Figure 4.2: Comparison of the spectral flow of the Harper-Hofstadter model in self-similar structures to that in a square lattice. In each column, the top panel shows the position of the flux-tube with respect to the structure under consideration, and the bottom panel shows the corresponding spectral flow. (a) shows the spectral flow in a a 29×29 square lattice with open boundary conditions ($N = 841$ sites). (b) and (c) show the spectral flow in two other self-similar structures, not originating from the Sierpinski gasket, with Hausdorff dimensions $\log(7)/\log(3)$ ($N = 7^4$ sites) and $\log(8)/\log(3)$ ($N = 8^4$ sites) respectively. For the square lattice, the spectral flow is observed across the band gap. In contrast, in self-similar structures, there is no well-defined notion of bands and associated gaps. The nature of the spectral flow for these structures is similar to that of the SG-3 (Fig. 4.1); all eigenstates in the low ρ_E region of the spectra enclosing the flux-tube undergo spectral flow.

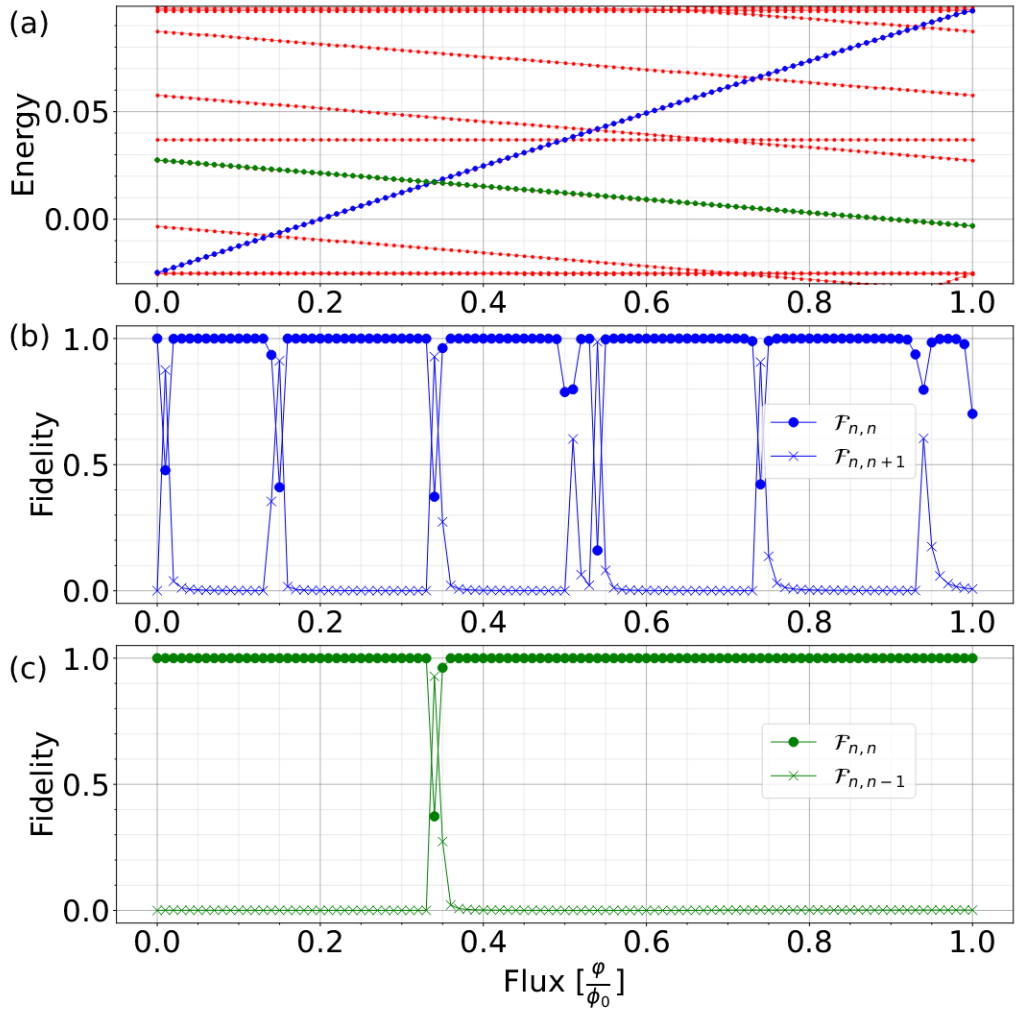

Figure 4.3: Fidelity computations for avoided crossings. Fidelity is defined here as: $\mathcal{F}_{n,m} = \langle\psi_n(\varphi)|\psi_m(\varphi - \delta\varphi)\rangle$. For the numerics, we have chosen $\delta\varphi = 0.01\phi_0$ and $N = 3^7$. (a) shows a part of the instantaneous spectrum when the flux tube is placed inside one of the triangles of the second generation (shown in Fig. 4.1(c)). The flow of two particular states, one of them being primarily localized on the sites immediately enclosing the triangle of the second generation and the other being localized on the sites of the outermost triangle of the SG, are marked in blue and green colors. (b) and (c) show the fidelity of these two states as a function of φ. Large dips in $\mathcal{F}_{n,n}$ and a correspondingly large peak in $\mathcal{F}_{n,n-1}$ ($\mathcal{F}_{n,n+1}$) are seen when the highlighted states come close in energy with another state localized on far off sites. These indicate that the state $|\psi_n\rangle$ has flowed to $|\psi_{n-1}\rangle$ ($|\psi_{n+1}\rangle$) without any significant hybridization. On the other hand, shallow dips in $\mathcal{F}_{n,n}$ and a correspondingly small peak in $\mathcal{F}_{n,n-1}$ ($\mathcal{F}_{n,n+1}$) are seen when the highlighted states come close in energy to a state localized on sites relatively close to the highlighted states. These indicate avoided crossings with significant hybridization.

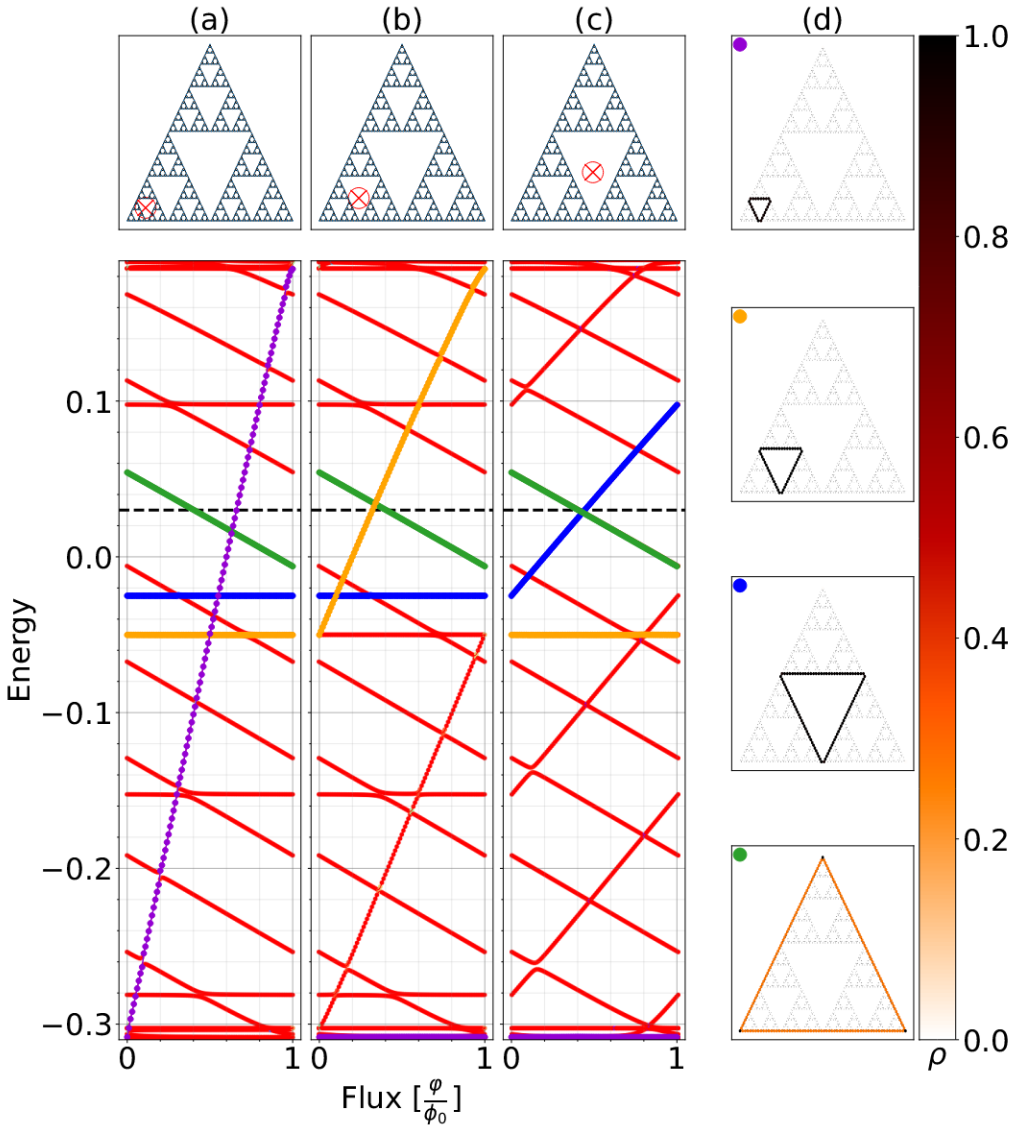

Figure 4.4: Change in the spectral flow due to the change in the position of the flux tube for SG-3 ($N = 3^6$, $\phi/\phi_0 = 0.3$). Columns (a), (b) and (c) show a portion of the spectral flow for three different positions of the flux tube. The position of the flux tube is marked by a red cross-hair in the SG-3 diagrams at the top of the respective columns. A few typical states which are localized on sites enclosing holes of different generations are chosen and their spectral flows are highlighted with different colors. Column (d) shows the localization of these typical states ($\varphi/\phi_0 = 0.2$). To mark the correspondence, we have put circles of respective colors on the top-left corner of each of the localization plots. The black dashed line shows the position of the Fermi energy, $E_F = 0.03$. The figure shows that only the edge-like states enclosing the flux tube undergo spectral flow.

flow by changing the position of the flux. Clearly, a state localized on a given loop only undergoes spectral flow when the flux tube is enclosed within the loop. Also, for a bunch of degenerate edge-like states localized on different loops, the flux tube breaks the degeneracy if enclosed by one of the loops, resulting in spectral flow of only the state enclosing the flux tube (Fig. 4.6).

There are a few other states in the spectra which we have not discussed in detail in this work. These states belong to the very few high ρ_E regions in the spectra. In terms of localization, they are predominantly bulk-like in nature. Also, they do not show a clear spectral flow, owing to the high ρ_E around them.

4.2.2 *Charge transport from the instantaneous spectrum*

Let us consider a case where we have filled our system to a certain Fermi energy, E_F (dashed black line in Fig. 4.4). At $\varphi = n\phi_0 : \ n \in \mathcal{Z}$, let us denote the set of states with positive spectral flow (group I in Sec. 4.2.1) as $\{|\psi^p{}_m\rangle\}$ with energies $\{E_m\}$, and the set of states with negative spectral flow (group II in Sec. 4.2.1) as $\{|\psi^n{}_{m'}\rangle\}$ with energies $\{E_{m'}\}$. Here, m, m' are the labels for the eigenstates localized on sites immediately enclosing a single triangle of a given generation of SG-3, such that their energies are ordered increasingly ($E_m < E_{m+1}$ for all m). Now, let us assume E_F is such that $E_m < E_F < E_{m+1}$ and $E_{m'-1} < E_F < E_{m'}$ for some m, m'.

When we vary the flux adiabatically by a unit through the flux tube, the Hamiltonian returns back to itself (up to a gauge transformation), but the states undergoing spectral flow do not return back to themselves. In the beginning of the pumping cycle, $\psi^p{}_m$, $\psi^n{}_{m'-1}$ were occupied and $\psi^p{}_{m+1}$, $\psi^n{}_{m'}$ were empty. During the pumping cycle, the filled state $\psi^p{}_m$ gets pushed up in energy across E_F and flows to $\psi^p{}_{m+1}$, and the empty state $\psi^n{}_{m'}$ flows down in energy across the E_F to $\psi^n{}_{m'-1}$. As a result of this spectral flow, at the end of the pumping cycle, $\psi^p{}_{m+1}$ is filled and $\psi^n{}_{m'-1}$ is empty. This spectral flow is observed for all m, m' such that E_m and $E_{m'}$ are away from the gaps (regions with zero ρ_E) in the energy spectrum at $\varphi = 0$. And as long as E_F is away from these gaps, exactly one state with positive spectral flow and one state with negative spectral flow cross the Fermi energy during the pumping cycle. Now, as pointed out earlier in the previous subsection, $\psi^n{}_{m'} \forall m'$ are localized on the sites on the outermost triangle and $\psi^p{}_m \forall m$ are localized on the closest sites enclosing the flux tube. So, when a unit flux is pumped, a single state localized on the outer-most sites of SG-3 is emptied and a single state localized near the flux tube gets filled, effectively pumping a unit charge radially from the outer-most loop to the loop closest to the flux tube. The mathematical details corresponding to the above arguments can be found in section 4.1.

We want to highlight the local nature of the radial charge transport happening in this case. From the instantaneous spectrum (columns (a), (b), (c) of Fig. 4.4), it is clear that edge-like states, localized on sites immediately enclosing different triangles of SG-3, undergo spectral flow and cross the Fermi energy as the position of the flux tube is changed. As described in the previous paragraph, only these states which flow across the Fermi energy contribute to the radial charge transport as a result of adiabatic pumping. So, given the position of the flux-tube and the Fermi energy, it is possible to exactly determine which edge-like states are contributing to the transport. Also, the position of the flux-tube can be used as a tuning parameter to selectively pump particles from sites immediately enclosing a particular triangle to the outermost triangle. In Sec. 4.3, we also compute the local Hall conductivity in a slightly different setting which also reveals the local nature of the transverse charge transport in greater detail.

4.3 LOCAL HALL CONDUCTIVITY AND ITS ROBUSTNESS TO DISORDER

In this section, we study local contributions to the Hall conductivity, following the approach of [dBL22]. Specifically, we look at the Hall response of the system when the system is subjected to a step-function electric potential. To do this, we consider a horizontal cross-section at some $y = y_0$ and raise the potential of the system below this cross-section by $-V_0$. Such a potential can be treated in a time dependent gauge, $\mathbf{A(t)} = (0, -A(t)\delta(y - y_0), 0)$, where $A(t) = V_0 t$. The time dependent Hamiltonian then becomes $H(t) = e^{iA(t)\vartheta(y_0)} H e^{-iA(t)\vartheta(y_0)}$, where $\vartheta(y_0) = \sum_j \theta(y_j - y_0) \left|\mathbf{r}_j\right\rangle \left\langle\mathbf{r}_j\right|$. Now, working in the adiabatic limit, we look at the transverse current across a vertical cross-section at some $x = x_0$. For a non-interacting finite system in the above mentioned setting, it has been shown that the site-resolved Hall-conductivity, $\sigma_{xy}(r)$, can be expressed as a local Chern marker in the adiabatic limit [dBL22]. We highlight here the main ideas leading to this result in the context of our system. The details of the calculation can be found in Ref. [dBL22] and references therein.

Given that we are interested in the adiabatic limit, we use the adiabatic Hamiltonian, $K(t) = i[\dot{P}_I, P_I]$, to generate the time-evolution. Here, P_I is the instantaneous projection operator onto the occupied states defined as $P_I = \sum_{E_n < E_F} \left|n(t)\right\rangle \left\langle n(t)\right|$, where $H(t) \left|n(t)\right\rangle = E_n \left|n(t)\right\rangle$. With the adiabatic Hamiltonian, the instantaneous projection operator satisfies the von Neumann equation

$$\partial_t P_I(t) = -i[K, P_I]. \tag{4.10}$$

Given the form of $H(t)$, it is clear that $P_I = e^{iV_0 t\vartheta(y_0)} P e^{-iV_0 t\vartheta(y_0)}$, and hence $K(t) = \dot{A}(P\vartheta(y_0)Q + Q\vartheta(y_0)P)$, where $P = P_I(t = 0)$ and $Q = \mathbb{1} - P$. The adiabatic transverse current operator, $J_x(t)$, can be obtained from the rate of change of the number of particles present in one side of the vertical cross-section using the instantaneous von Neumann equation, as $J_x(t) =$

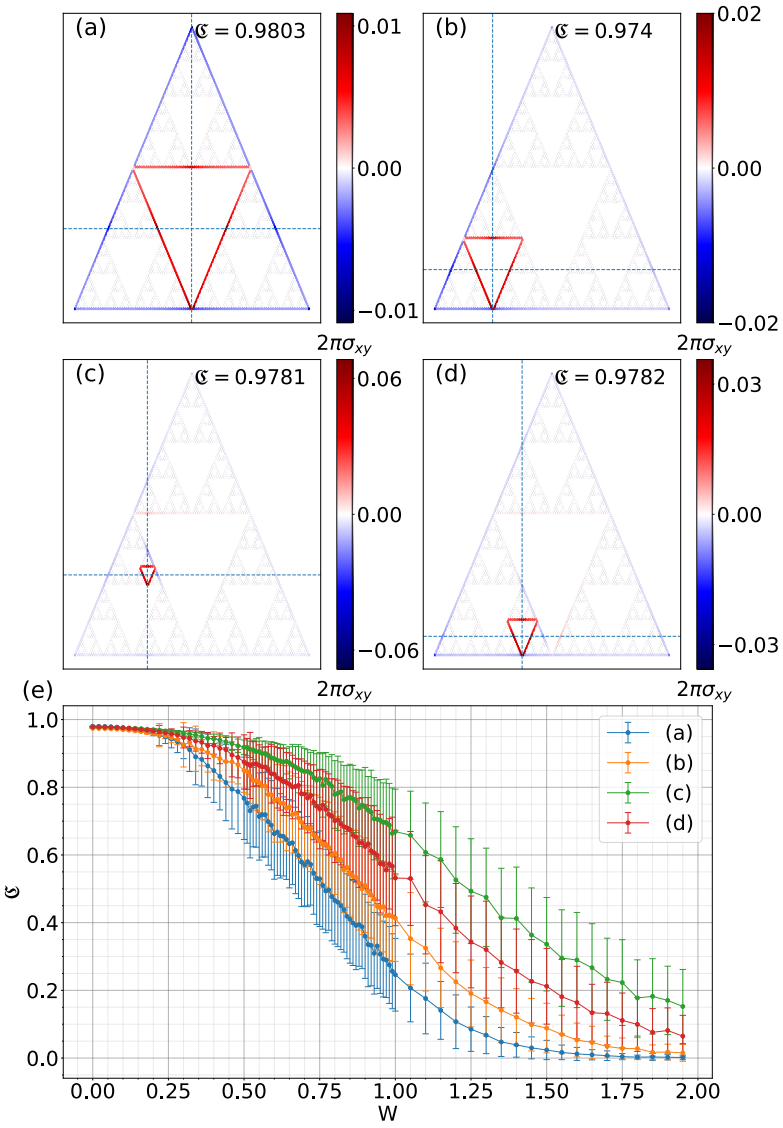

Figure 4.5: (a-d) Site-resolved Hall conductivity, σ_{xy}, for the Harper-Hofstadter model on SG-3 with $N = 3^7$, for $E_F = 0.03$. The dashed horizontal line represents the cross-section across which the potential difference is applied. The dashed vertical line represents the cross-section across which the current has been calculated. The sum over local Hall conductivity, $\mathfrak{C} = \sum_{r\in\mathcal{P}} 2\pi\sigma_{xy}(r)$, where $\mathcal{P}$ denotes the set of sites which immediately enclose the cross-hair, are mentioned on the plots up to four decimal places. (e) Variation of the local sum of Hall conductivity, $\mathfrak{C}$, as a function of disorder strength W for different positions R of the cross-hair as in (a-d), calculated for the Harper-Hofstadter model with onsite Anderson disorder on SG-3 with $N = 3^7$, for $E_F = 0.03$. Averaging has been done with, $N_w = 200$, disorder realizations. The error bars on the plot show the statistical standard deviation of $\mathfrak{C}$ over the disorder realizations.

$i[K(t), \vartheta(x_0)]$, where $\vartheta(x_0) = \sum_j \theta(x_j - x_0) \left|\mathbf{r}_j\right\rangle \left\langle\mathbf{r}_j\right|$. The site-resolved current operator can be defined as

$$J_x^A(\mathbf{r}_j, t) = \frac{1}{2}\{\delta_j, J_x^A(t)\}, \tag{4.11}$$

where $\delta_j = \left|\mathbf{r}_j\right\rangle \left\langle\mathbf{r}_j\right|$. So, the site-resolved adiabatic current, $\langle J_x^A(\mathbf{r}_j, t)\rangle = \mathrm{Tr}_{\mathbf{r}_j}(P_I J_x^A(\mathbf{r}_j, t))$, is then given by

$$\langle J_x^A(\mathbf{r}_j, t)\rangle = i\dot{A}\mathrm{Tr}_{\mathbf{r}_j}(P\vartheta(x_0)Q\vartheta(y_0)P) + h.c.. \tag{4.12}$$

Now, identifying $\dot{A} = -E$, we get the expression for Hall conductivity, $\sigma_{xy} = \langle J_x^A(\mathbf{r}_j, t)\rangle / E$, as

$$\sigma_{xy}(\mathbf{r}_j) = 2\mathrm{Im}\mathrm{Tr}_{\mathbf{r}_j}(P\vartheta(x_0)Q\vartheta(y_0)P). \tag{4.13}$$

The local Chern marker is then defined as $\mathfrak{C}(\mathbf{r}_j) = 2\pi\sigma_{xy}(\mathbf{r}_j)$. This has been referred to as the cross-hair marker in Ref. [dBL22] due to the fact that the horizontal line at $y = y_0$ and $x = x_0$ appear as a cross-hair. An important thing to note here is that the local Chern marker defined above is not unique for a given system as the way to define the site-resolved adiabatic current is not unique. The definition given in Eq. (4.11) is one simple way to define such a local quantity. Instead, the quantity which is physically relevant is the sum of the local Chern marker over some given region. This is because the sum of the local Chern marker over a region can be expressed as the Hall conductivity which is derived from the total current leaking from that given region. The current leaking from that given region is defined as the rate of change of particles over the region and does not have ambiguity in its definition as opposed to the site-resolved adiabatic current.

Figure 4.5 (a-d) shows the adiabatic site-resolved Hall conductivity calculated for our system. For the purpose of comparing to the charge pumping picture, we have kept the same Fermi energy for these computations as that for the charge pumping computations. We find that there are two significant local contributions to σ_{xy}, one positive and one negative, as $\sum_j \sigma_{xy}(\mathbf{r}_j) = 0$ due to the conservation of particle number over the entire system. Fixing the cross-section ($y = y_0$) across which the potential difference is applied, when we change the cross-section ($x = x_0$) across which the transverse current is calculated, we find numerically that the positive contributions to σ_{xy} come only from the sites close to the position of the cross-hair. More specifically, we find that, given a position of the cross-hair, the positive contributions to σ_{xy} come only from the sites which enclose the cross-hair as long as the cross-hair is not inside one of the smallest triangles of the structure. The negative contribution comes solely from the sites on the outer-most triangle of SG-3. What this suggests is that, as long as we are away from the smallest possible triangles of the structure, the contribution to the transverse current

comes primarily from the sites which immediately enclose the cross-hair, or in other terms, from the edge-like states which are localized on the sites enclosing the triangle containing the cross-hair. This shows the correspondence between the local contribution to the Hall conductivity and the local nature of the transverse charge transport in this system mentioned in Sec. 4.2.2.

The local Chern marker essentially serves as a local deconstruction of Kitaev's real space Chern number given in Eq. (3.9). The major contribution to Kitaev's real space Chern number comes from the region where the three partitions touch each other [Kito6]. Away from the triple contact point, the contribution to Kitaev's real space Chern number decreases exponentially and hence it is insensitive to the exterior of the union of the three partitions for large enough partitions. As a result, Kitaev's real space Chern number can be expressed as $C(P) = 2\pi i \mathrm{Tr}([P\vartheta(x_0)P, P\vartheta(y_0)P])$ when x_0, y_0 are chosen as the co-ordinates of the triple contact point, as mentioned in Eq. (128) of reference [Kito6]. This is also the expression for the Hall conductivity as shown in reference [ASS94]. However, this is nothing but the negative of the sum of the local Chern marker over the sites present in a large enough region around the triple contact point. Given that Kitaev's real space Chern number is expressed as a trace over sites of a region, it does not provide information about the local nature of the Hall transport. Hence, it does not tell us which single-particle states would undergo spectral flow. However, the information about the local nature of the Hall transport is captured by the local Chern marker, revealing the correspondence between the local contribution to the Hall conductivity and the local nature of the spectral flow as mentioned in the previous paragraph.

To see the quantized nature of the charge transport, we look at the sum of the local Chern marker over the sites in the proximity of the cross-hair. More specifically, we look at

$$\mathfrak{C} = \sum_{\mathbf{r}_j \in \mathcal{P}} 2\pi\sigma_{xy}(\mathbf{r}_j), \tag{4.14}$$

where $\mathcal{P}$ denotes the set of sites which immediately enclose the smallest triangle containing the cross-hair. We consider this quantity as it is physically relevant and it tells about the net charge leaking from the region containing the sites in $\mathcal{P}$. This can be expressed as the change in the projector over the occupied states, traced over the given region when the Hamiltonian is taken in a cycle [dBL22; Kito6; ASS94]. Hence, this quantity would be quantized if the change in the projector has support only in the region we trace over. In this system, we find that the value of $\mathfrak{C}$ is closely quantized to 1, as mentioned in the plots in Fig. 4.5 (a-d), suggesting again that significant contribution to the radial current comes from the edge-like states localized on sites in $\mathcal{P}$.

To see the topological nature of the charge transport, we perturb the Hamiltonian slightly by adding small on-site disorder. The new disordered Hamiltonian is then given by

$$H_{dis} = H + \sum_j \epsilon_j c_j^\dagger c_j, \tag{4.15}$$

where ϵ_j is a random number with a uniform distribution over the interval $[-W/2, W/2]$. For a given Fermi energy, we compute $\sigma_{xy}(\mathbf{r}_j)$ for various disorder realizations of the same disorder strength W. We find that, for $W \neq 0$, the contribution to σ_{xy} now not only comes from the sites in $\mathcal{P}$, but also spreads over to few other sites in the proximity of $\mathcal{P}$. This spread increases initially as we increase W until the states become Anderson localized and $\sigma_{xy}(\mathbf{r}_j)$ goes to zero. To quantify this spread and study the robustness to disorder, we then look at how $\mathfrak{C}$, averaged over several disorder realizations, changes as a function of disorder strength W. The result is shown in Fig. 4.5 (e).

We find that up to $W \approx 0.2$, the value of $\mathfrak{C}$ is pretty well quantized and robust to disorder. As we keep increasing W, the average value of $\mathfrak{C}$ starts decreasing and the standard deviation, shown as error bars in Fig. 4.5 (e), starts increasing. The initial decrease in the average value of $\mathfrak{C}$ is a consequence of the increase of the contribution to σ_{xy} coming from the sites not present in $\mathcal{P}$. The standard deviation can be considered as an indicator of the amount of variation of the contribution to σ_{xy} is coming from the sites not present in $\mathcal{P}$, which are found to be random in nature. This spread can be understood by the fact that in the presence of weak disorder, the edge-like states start to lose their property of being primarily localized on the sites in $\mathcal{P}$. It is natural to ask if there is a better quantization at higher W, by redefining $\mathfrak{C}$ to take into account the contributions of a few additional layers of sites apart form those in $\mathcal{P}$ to σ_{xy}. However, for this structure, there is no natural way to determine how to select sites to define a layer of sites and how many additional layers of sites to take into account. Also, because of the non-uniformity in the spread of the edge-like states to the nearby sites in the presence of weak random disorder, it is not clear how to determine a length scale by quantifying their loss of localization.

4.4 EDGE-LIKE STATES IN SIERPINSKI-HOFSTADTER MODEL

Pumping flux through a flux-tube at a given position not only makes it possible to determine how the states contribute to the transport, but it also makes it possible to numerically study each edge-like state individually. The edge-like state localized on sites immediately enclosing triangles of a given generation are usually degenerate in energy as there are often multiple triangles of a given generation in SG-3. One example is shown in Fig. 4.6(a), where three states are degenerate, because there are three triangles of the second generation. The number of triangles of a given generation increases

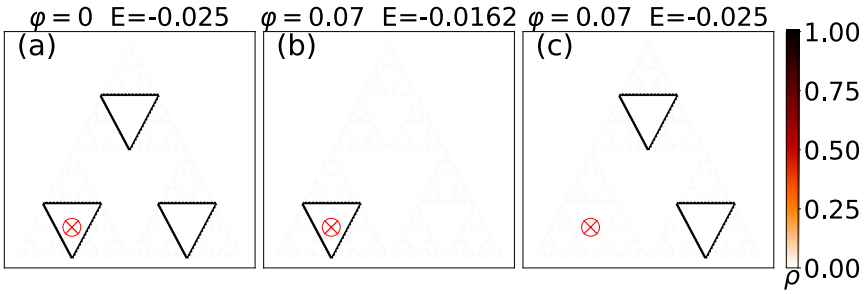

Figure 4.6: The figure shows the degeneracy between edge-like states of SG-3 ($N = 3^7$) at $\phi = 0.3\phi_0$, highly localized on sites immediately enclosing triangles of the second generation, being lifted when the flux through the tube, φ, is changed from 0 to $0.07\phi_0$. (a) shows the localization of a single eigenstate from a bunch of triply degenerate edge-like states at $\varphi = 0$. Upon increasing φ to $\varphi = 0.07\phi_0$, the degeneracy breaks. One of the states, shown in (b), is lifted up in energy. The other two remain at the same energy as $\varphi = 0$, one of which is shown in (c).

exponentially with the generation. So, it becomes hard to isolate a single edge-like state localized on the sites immediately enclosing a single triangle of high enough generation. Now, by positioning the flux tube in a given triangle, the energy of the edge-like state localized on sites enclosing that particular triangle increases as we pump flux through the tube (grouped into group I in Sec. 4.2.1). The energy of the remaining degenerate partners of that edge-like state does not change with flux as they localize on sites which do not enclose the flux-tube (grouped into group IV in Sec. 4.2.1). One such instance of degeneracy breaking is shown in Fig. 4.6(b,c).

Now that we are able to break the degeneracy, we can study the properties of a single edge-like state. An edge-like state on SG-3, by definition, is highly localized on the sites immediately enclosing a triangle of a given generation (Fig. 4.7). Let us denote the set of such sites by $\mathcal{P}$. Notice that the sites in $\mathcal{P}$, together with the bonds with their respective nearest neighbors in $\mathcal{P}$, form a ring and hence they can be indexed linearly from 1 to $N_\mathcal{P}$, where $N_\mathcal{P}$ is the total number of sites in $\mathcal{P}$. Now, given an edge-like state, $|\psi^p_m\rangle = \sum_j \psi^m_j |\mathbf{r}_j\rangle$, we construct a state $|\psi_m\rangle = \sum_{\mathbf{r}_j \in \mathcal{P}} \psi^m_j |\mathbf{r}_j\rangle$. $|\psi_m\rangle$ is easy to study due to its one dimensional nature and can be considered a good approximation for $|\psi^p_m\rangle$ for large system sizes.

The exact expression of the edge-like states is gauge dependent. So to study $|\psi_m\rangle$, we first transform to a different gauge where the Hamiltonian, H, becomes translationally invariant on the sites in $\mathcal{P}$. The gauge transformation is given by: $c^\dagger_j \to e^{-i\Theta_j} c^\dagger_j$, where $\Theta_1 = 0$, $\Theta_j = \sum_{n=2}^{n=j} \theta_{n-1,n} - (j-1)2\pi\Phi/N_\mathcal{P}\phi_0$ for $j \in \{2, 3, \ldots, N_\mathcal{P}\}$, where $2\pi\Phi$ is the total flux threaded through the area enclosed by the sites in $\mathcal{P}$. Let us call this the 'translationally invariant' gauge. Let the transformed state be denoted by $|\psi'_m\rangle = \sum_j \psi'^m_j |\mathbf{r}_j\rangle$. We do a Fourier transform, $\psi^m_\kappa = \sum_j e^{i2\pi\kappa j/N_\mathcal{P}} \psi'^m_j$, to go into the angular momentum

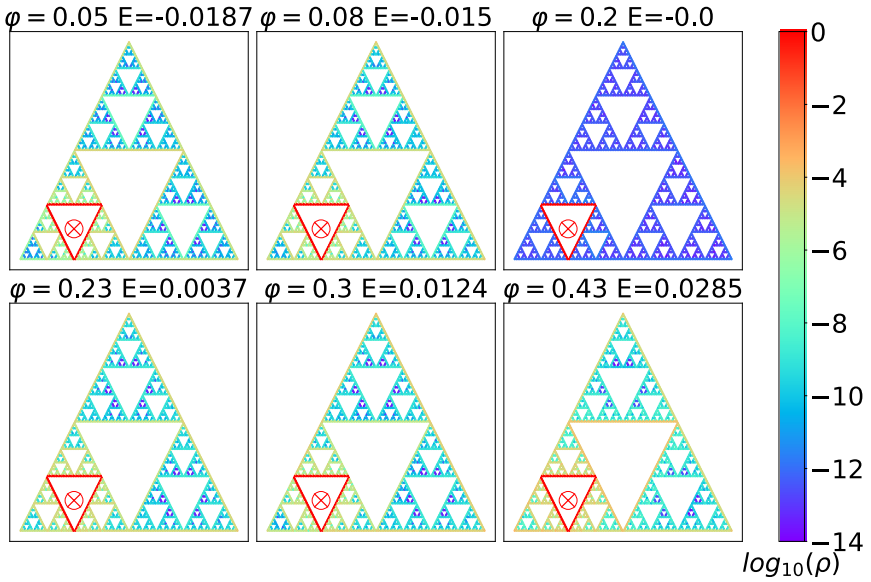

Figure 4.7: Localization of a single edge-like state at different values of φ. The colorbar shows $\log_{10}(\rho_j)$. The values of φ in the plots are given in units of ϕ_0 and the values of the φs for this figure are chosen as such to remain significantly away from the avoided crossing points. We see that the weight of the eigenstate on sites not in $\mathcal{P}$ (defined in Sec. 4.4) is at least 3 orders of magnitude less than that of the sites in $\mathcal{P}$. $\varphi = 0.2\phi_0$ is a special case where the edge-like state is completely localized on the sites in $\mathcal{P}$.

basis. We find that, for a given m, ψ^m_κ has two sharp peaks at κ and $N_\mathcal{P}/2+\kappa$, (one peak being significantly greater than the other) for some value of $\kappa = \kappa_0$ (Fig. 4.8), as long as we are sufficiently away from an avoided crossing. The peaks change from $\kappa_0 \to \kappa_0 + 1$ and $N_\mathcal{P}/2 + \kappa_0 \to N_\mathcal{P}/2 + \kappa_0 + 1$ as the flux, φ/ϕ_0, is changed from 0 to 1 (Fig. 4.8 (a)). Moreover, we also find that the position of the peaks changes linearly as we change m (Fig. 4.8 (b)). These features are reminiscent of eigenstates of a particle on an $N_\mathcal{P}$-polygon with a flux threaded through it, or in other words, eigenstates of the discretized angular momentum operator [ABA04]. In fact, these properties are captured by approximating, $|\psi'_m\rangle \approx |\tilde{\psi}_m\rangle = \psi^m_{\kappa_0}|\kappa_0\rangle + \psi^m_{\kappa_0+N_\mathcal{P}/2}|\kappa_0 + N_\mathcal{P}/2\rangle$, where $|\kappa_0\rangle$ and $|\kappa_0 + N_\mathcal{P}/2\rangle$ are eigenstates of the discretized angular momentum operator with eigenvalues κ_0 and $\kappa_0 + N_\mathcal{P}/2$ respectively. $|\tilde{\psi}_m\rangle$ also captures the chiral nature of the edge-like states as shown in Fig. 4.9.

For a given magnetic field parameterized by ϕ, there are some special values of the flux φ for which an edge-like state can be completely localized on the sites in $\mathcal{P}$ (for example, $\varphi = 0.2\phi_0$ in Fig. 4.7). For such values of φ, the edge-like state exactly becomes an eigenstate of the discretized angular momentum operator in the 'translationally invariant' gauge. This shows that the flux through the flux-tube can also be used as a tuning parameter to completely localize an edge-like state on a ring and host exact eigenstates of the angular momentum operator on SG-3. The details of the condition which

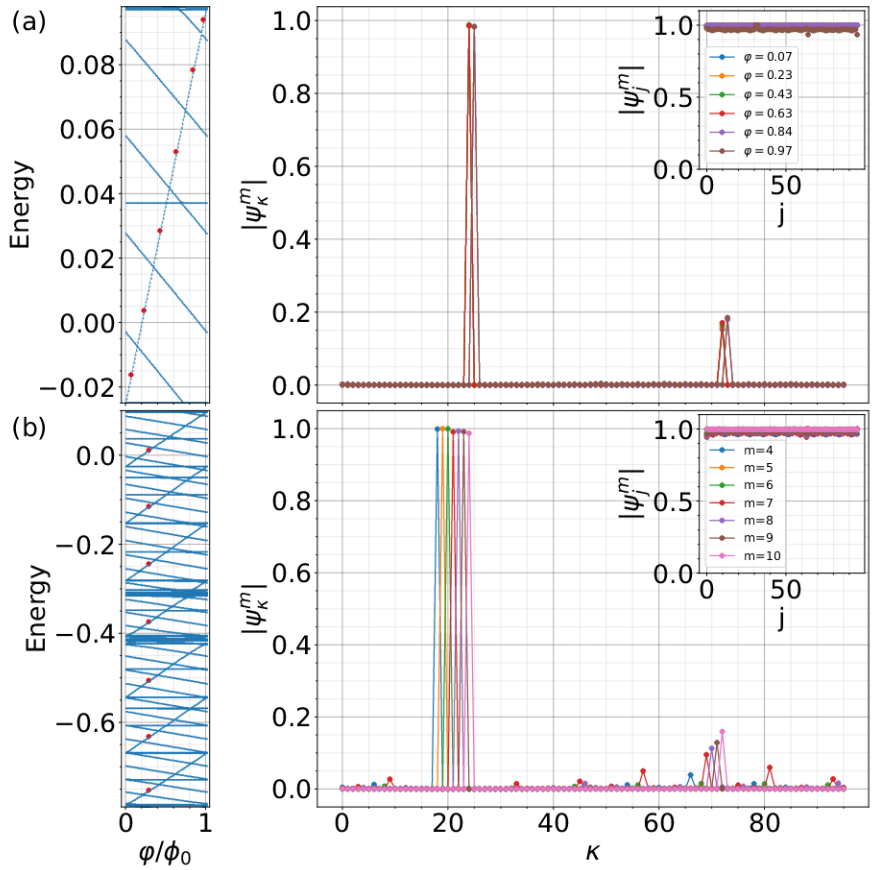

Figure 4.8: The variation in Fourier amplitudes of edge-like states, ψ_κ^m vs κ, for different values of φ and different values of m. In this case, $N = 3^7$ and $N_\mathcal{P} = 96$. Row (a) shows ψ_κ^m vs κ for a single edge-like state ($m = 10$). As φ/ϕ_0 is varied from 0 to 1, the peaks at $\kappa = 24$ and $N_\mathcal{P}/2 + \kappa = 72$ shift by one unit to $\kappa = 25$ and $N_\mathcal{P}/2 + \kappa = 73$. Row (b) shows ψ_κ^m vs κ for different edge-like states which are primarily localized on the sites in $\mathcal{P}$. The insets in both (a) and (b) show how strongly the states are localized on the sites in $\mathcal{P}$. The states whose Fourier components are shown are marked with red on the instantaneous spectra. In both (a) and (b), the values of ψ_κ^m have been normalized such that $\sum_\kappa |\psi_\kappa^m|^2 = 1$.

must be satisfied to generate such an edge-like state is given in section 4.4.1.

4.4.1 *Condition for strict localization of edge-like states on SG-3*

We start with the Harper-Hofstadter Hamiltonian on SG-3, given by

$$\hat{H} = \sum_{\langle jk \rangle} H_{jk} c_j^\dagger c_k, \tag{4.16}$$

where $H_{jk} = -e^{-i\theta_{jk}}$, when the sites labeled by the indices j and k are nearest neighbors and 0 otherwise. θ_{jk} is the same as defined in Eq. (2.16) of the main text. Let H denote the Hamiltonian matrix whose elements are H_{ij}. Consider a triangle of a given generation of SG-3. We put a flux tube, carrying flux $2\pi\varphi$, through this triangle. Let us denote the set of all sites immediately

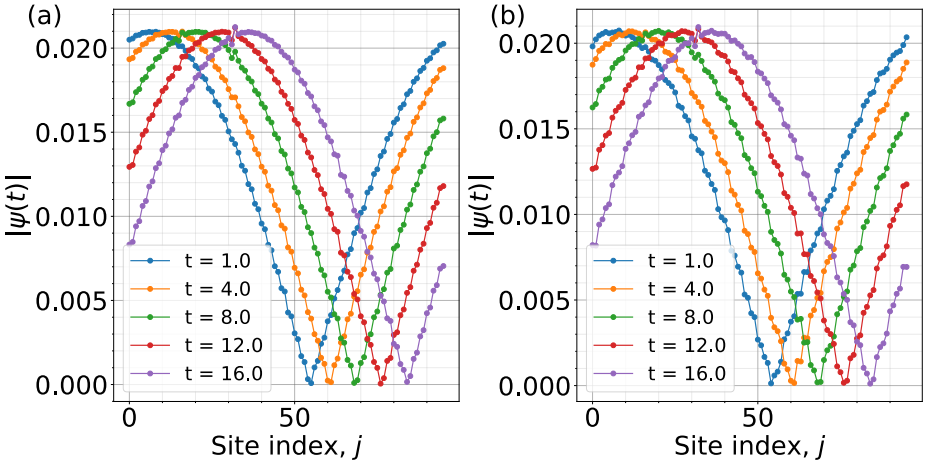

Figure 4.9: Time evolution under the action of (a) the approximate time evolution operator and (b) the exact time evolution operator, projected onto a given energy window $(E_{\min}, E_{\max})$. The initial state is localized on a site in $\mathcal{P}$. The exact time evolution operator, projected onto the energy window, is given by $U(t) = \sum_{E_{\min}<E_n<E_{\max}} \exp(-iE_n t) \left|n\right\rangle \left\langle n\right|$, where $\left|n\right\rangle$ is the set of single particle eigenstates of the Hamiltonian H, with energy E_n. The approximate time evolution operator is given by $\tilde{U}(t) = \sum_{E_{\min}<\tilde{E}_n<E_{\max}} \exp\left(-i\tilde{E}_n t\right) \left|\tilde{n}\right\rangle \left\langle \tilde{n}\right|$. $\left|\tilde{n}\right\rangle = \left|\tilde{\psi}_n\right\rangle$ for edge-like states localized primarily on $\mathcal{P}$, where $\tilde{\psi}_n$ is the approximation of the state using its first largest two Fourier components as mentioned in Sec. 4.4, and $\left|\tilde{n}\right\rangle = \left|n\right\rangle$ otherwise. $\tilde{E}_n = \left\langle \tilde{n}\right|H\left|\tilde{n}\right\rangle$. Note that, at $t = 0$, both U and $\tilde{U}$ act as a projection operator onto the set of states in the energy window. Comparing (a) and (b), we find that the chiral nature of the edge-like states is well captured by the approximate states mentioned in Sec. 4.4. For this calculation, we have taken $N = 3^7$, $N_{\mathcal{P}} = 96$, $E_{\min} = -0.3$ and $E_{\max} = 0$.

enclosing the triangle to be $\mathcal{P}$, and the set containing the rest of the sites to be $\mathcal{Q}$. Now consider an edge-like state $|\psi\rangle = \sum_j \psi_j |\mathbf{r}_j\rangle$. By breaking into sectors of $\mathcal{P}$ and $\mathcal{Q}$, the Hamiltonian can be represented in the matrix form as follows

$$H = \begin{bmatrix} H_{\mathcal{P}} & H_{\mathcal{PQ}} \\ H_{\mathcal{QP}} & H_{\mathcal{Q}} \end{bmatrix}, \tag{4.17}$$

where $H_{\mathcal{P}_{jk}} = H_{jk}$, $\forall j,k \in \mathcal{P}$; $H_{\mathcal{PQ}_{jk}} = H_{jk}$, $\forall j \in \mathcal{P}$, $k \in \mathcal{Q}$; $H_{\mathcal{QP}_{jk}} = H_{jk}$, $\forall j \in \mathcal{Q}$, $k \in \mathcal{P}$; and $H_{\mathcal{Q}_{jk}} = H_{jk}$, $\forall j,k \in \mathcal{Q}$. Similarly the state $|\psi\rangle$ can be expressed as

$$|\psi\rangle = \left|\psi^{\mathcal{P}}\right\rangle + \left|\psi^{\mathcal{Q}}\right\rangle, \tag{4.18}$$

where $\left|\psi^{\mathcal{P}}\right\rangle = \sum_{p\in\mathcal{P}} \psi_p |\mathbf{r}_p\rangle$ and $\left|\psi^{\mathcal{Q}}\right\rangle = \sum_{q\in\mathcal{Q}} \psi_q |\mathbf{r}_q\rangle$. In the vector form, let $\Psi^{\mathcal{P}} = [\psi_{p_1}\ \psi_{p_2}....\psi_{p_{N_p}}]^{\mathrm{T}}\ \forall\{p_i\} \in \mathcal{P}$ and $\Psi^{\mathcal{Q}} = [\psi_{q_1}\ \psi_{q_2}....\psi_{q_{N_q}}]^{\mathrm{T}}\ \forall\{q_i\} \in \mathcal{Q}$ be the representations for $\left|\psi^{\mathcal{P}}\right\rangle$ and $\left|\psi^{\mathcal{Q}}\right\rangle$ respectively.

If the state is completely localized on sites in $\mathcal{P}$, then $\Psi^{\mathcal{Q}} = 0$. Now, given that $\Psi = [\Psi^{\mathcal{P}}\ \Psi^{\mathcal{Q}}]^{\mathrm{T}}$ is an eigenstate of H, we get that

$$H\Psi = \begin{bmatrix} H_{\mathcal{P}} & H_{\mathcal{PQ}} \\ H_{\mathcal{QP}} & H_{\mathcal{Q}} \end{bmatrix} \begin{bmatrix} \Psi^{\mathcal{P}} \\ 0 \end{bmatrix} = \begin{bmatrix} H_{\mathcal{P}}\Psi^{\mathcal{P}} \\ H_{\mathcal{QP}}\Psi^{\mathcal{P}} \end{bmatrix} = E_m \begin{bmatrix} \Psi^{\mathcal{P}} \\ 0 \end{bmatrix}. \tag{4.19}$$

This implies that $\Psi^{\mathcal{P}}$ must be an eigenstate of $H_{\mathcal{P}}$ and $H_{\mathcal{QP}}\Psi^{\mathcal{P}} = 0$. $\Psi_{\mathcal{P}}$ can be analytically determined. To do that, we first point out that the sites in $\mathcal{P}$, together with the bonds with their respective nearest neighbors in $\mathcal{P}$, form a ring. They can be indexed linearly from 1 to $N_{\mathcal{P}}$, where $N_{\mathcal{P}}$ is the total number of sites in $\mathcal{P}$. So $\Psi^{\mathcal{P}}$ can be written as $\Psi^{\mathcal{P}} = [\psi_1\ \psi_2...\psi_p...\psi_{N_p}]^{\mathrm{T}}$. We do a gauge transformation given by $c_j^\dagger \to c'^\dagger_j = e^{-i\Theta_j} c_j^\dagger$, where $\Theta_1 = 0$, $\Theta_j = \sum_{n=2}^{j} \theta_{n-1,n} - (j-1)2\pi\Phi/N_{\mathcal{P}}\phi_0$ for $j \in \{2,3,\ldots,N_{\mathcal{P}}\}$, where $2\pi\Phi$ is the total flux threaded through the area enclosed by the sites in $\mathcal{P}$. Under this transformation, $\Psi^{\mathcal{P}} \to \Psi'^{\mathcal{P}}$ and $H_{\mathcal{P}} \to H'_{\mathcal{P}}$, where $H'_{\mathcal{P}}$ is a Hermitian circulant matrix given by

$$H'_{\mathcal{P}} = \begin{bmatrix} 0 & t & 0 & \cdots & 0 & t^* \\ t^* & 0 & t & \cdots & 0 & 0 \\ 0 & t^* & 0 & t & \cdots & 0 \\ \vdots & \vdots & \vdots & \ddots & \vdots & \vdots \\ t & 0 & 0 & \cdots & t^* & 0 \end{bmatrix}, \tag{4.20}$$

and $t = e^{-i2\pi\Phi/N_{\mathcal{P}}\phi_0}$. The eigenvectors of $H'_{\mathcal{P}}$ are given by

$$\psi(\kappa) = [\ \omega^{\kappa}\ \omega^{2\kappa}\ \omega^{3\kappa} \ldots \omega^{p\kappa} \ldots \omega^{N_{\mathcal{P}}\kappa}]^{\mathrm{T}}\ \forall \kappa \in \{0,1,\ldots,N_{\mathcal{P}}-1\},$$

where $\omega = e^{i2\pi/N_{\mathcal{P}}}$. So, $\Psi'^{\mathcal{P}}$ must be equal to $\psi(\kappa)$ for some $\kappa \in \{0, 1, \ldots, N_{\mathcal{P}} - 1\}$. Now, $\Psi^{\mathcal{P}}$ can be obtained by inverting the gauge transform and so we get

$$\Psi^{\mathcal{P}}(\kappa) = [\psi_1(\kappa)\ \psi_2(\kappa)....\psi_{N_p}(\kappa)]^{\mathrm{T}}, \tag{4.21}$$

$$\psi_p(\kappa) = e^{i\Theta_p}\omega^{p\kappa} = e^{i\Theta_p}e^{i2\pi p\kappa/N_{\mathcal{P}}}. \tag{4.22}$$

Given the analytical form of $\Psi^{\mathcal{P}}$, we can plug Eq. (4.21) into the equation, $H_{\mathcal{QP}}\Psi^{\mathcal{P}} = 0$, and get

$$\sum_{p\in\mathcal{P}} H_{\mathcal{QP}_{q,p}}\psi_p = 0,\ \forall q \in \mathcal{Q}. \tag{4.23}$$

Notice that every site $q \in \mathcal{Q}$ either has exactly two consecutive nearest neighbors in $\mathcal{P}$ or zero nearest neighbors in $\mathcal{P}$. For the sites in $\mathcal{Q}$ which have zero nearest neighbors in $\mathcal{P}$, $H_{\mathcal{QP}_{q,p}} = 0\ \forall p \in \mathcal{P}$ and Eq. (4.23) is trivially satisfied. For the rest of the sites $q_0 \in \mathcal{Q}$, let us say sites $p_0 \in \mathcal{P}$ and $p_0 + 1 \in \mathcal{P}$ are its nearest neighbors. Then we have $H_{\mathcal{QP}_{q_0,p_0}}\psi_{p_0} + H_{\mathcal{QP}_{q_0,p_0+1}}\psi_{p_0+1} = 0$, which implies

$$e^{-i\theta_{q_0,p_0}}e^{i\Theta_{p_0}}\omega^{p_0\kappa} + e^{-i\theta_{q_0,p_0+1}}e^{i\Theta_{p_0+1}}\omega^{(p_0+1)\kappa} = 0. \tag{4.24}$$

Simplifying Eq. (4.24), we get the following condition

$$1 + \omega^{\kappa}e^{i(\Theta_{p_0+1}-\Theta_{p_0})}e^{-i(\theta_{q_0,p_0+1}-\theta_{q_0,p_0})} = 0. \tag{4.25}$$

From the choice of $\{\Theta_j\}$, we get $\Theta_{p_0+1} - \Theta_{p_0} = \theta_{p_0,p_0+1} - 2\pi\Phi/N_{\mathcal{P}}\phi_0$. Also, $\theta_{q_0,p_0} + \theta_{p_0,p_0+1} - \theta_{q_0,p_0+1} = \theta_{q_0,p_0} + \theta_{p_0,p_0+1} + \theta_{p_0+1,q_0} = -2\pi\phi/\phi_0$, which is nothing but the flux through the triangle whose vertices are sites $q_0,\ p_0$ and $p_0 + 1$. Plugging this in Eq. (4.25), we get

$$1 + \omega^{\kappa}e^{-i2\pi\Phi/\phi_0 N_{\mathcal{P}}}e^{-i2\pi\phi/\phi_0} = 0 \tag{4.26}$$

$$\implies \frac{i2\pi\kappa}{N_{\mathcal{P}}} - \frac{i2\pi\Phi}{N_{\mathcal{P}}\phi_0} - \frac{i2\pi\phi}{\phi_0} = (2n+1)i\pi \tag{4.27}$$

$$\implies \kappa - \frac{\Phi}{\phi_0} - N_{\mathcal{P}}\frac{\phi}{\phi_0} = \frac{(2n+1)}{2}N_{\mathcal{P}}, \tag{4.28}$$

where $n \in \mathbb{Z}$. We can express the total flux though the area enclosed by the $\mathcal{P}$ sites as the sum of the flux due to the magnetic field and the flux through the flux tube, $2\pi\Phi/\phi_0 = 2\pi\phi\Delta/\phi_0 + 2\pi\varphi/\phi_0$, where Δ is the ratio of the area of the region enclosed by the $\mathcal{P}$ sites and the area of the triangle whose vertices are the sites $q_0,\ p_0$ and $p_0 + 1$. Plugging this into Eq. (4.28), we get

$$\kappa = \frac{(2n+1)}{2}N_{\mathcal{P}} + (\Delta + N_{\mathcal{P}})\frac{\phi}{\phi_0} + \frac{\varphi}{\phi_0}. \tag{4.29}$$

For SG-3, we notice that $N_{\mathcal{P}} = 3z$, where z is the number of sites on one side of the triangle enclosed by the $\mathcal{P}$ sites, and z is always an even number. Δ is a natural number as it can be expressed in terms of z as, $\Delta = z^2 + 2z - 2$. Therefore, we must have

$$(\Delta + N_{\mathcal{P}})\frac{\phi}{\phi_0} + \frac{\varphi}{\phi_0} = Z \tag{4.30}$$

$$\kappa = \frac{(2n+1)}{2} N_{\mathcal{P}} + Z, \tag{4.31}$$

where Z is an integer. From Eqs. (4.30) and (4.31), we conclude that the state labeled by κ is completely localized on the sites in $\mathcal{P}$ if we choose φ such that Eq. (4.30) is fulfilled for the value of Z that produces the right κ in Eq. (4.31). The resulting state is an eigenstate of the angular momentum operator with eigenvalue κ.

4.5 SUMMARY

In this chapter, we present an understanding of topological phases on self-similar systems from the perspective of adiabatic charge pumping. We numerically investigate the spectral flow and the associated charge pumping when a flux tube is inserted through the structure and the flux through the tube is varied adiabatically. We find that the nature of the spectral flow is qualitatively different from that of translationally invariant non-interacting systems with a perpendicular magnetic field. We show that the instantaneous eigenspectra can be used to understand the quantization of the charge pumped over a cycle, and hence to understand the topological character of the system. We show the correspondence between the local contributions to the Hall conductivity and the spectral flow of the edgelike states. We also show that the edgelike states can be approximated by eigenstates of the discrete angular-momentum operator, their chiral nature being a consequence of this. In the next chapter, we go on to look into the role of symmetries on the topological phases in these systems.

5 INTERPLAY OF SYMMETRIES AND COORDINATION

In the previous chapters, we developed an understanding of the topological phases in self-similar systems. However, the systems considered there were simple tight-binding systems on self-similar structures in the presence of an external magnetic field, which did not possess any additional symmetries. In this chapter, we study the effect of symmetries on the topological phases in self-similar systems.

The symmetries (non-spatial and crystal) play an important role in determining which topological phases a lattice can host. For non-interacting translationally invariant systems, the classification of the topological phases has been done in terms of the ten-fold classification of the non-spatial symmetries. A comprehensive review on this can be found in reference [Chi+16]. The presence of crystal symmetries further diversifies and enriches the classification of the topological phases [Fu11].

In lattices, the way in which the sites are coordinated locally, plays an important role in determining the topological phases on a lattice which can be demonstrated with the following example. Consider a general two-orbital nearest-neighbor tight-binding model on a 2D Bravais lattice, similar to what is considered in [Fu11], given by

$$H_{tb} = \sum_{\mathbf{R},<\mathbf{r}>,\alpha,\beta} t(\mathbf{r})(\psi_\alpha^\dagger(\mathbf{R}) f(\theta_\mathbf{r}) \psi_\beta(\mathbf{R}+\mathbf{r})), \tag{5.1}$$

where $\mathbf{R}$ specifies the position vectors for the sites, $\mathbf{r}$ specifies the relative vectors between two sites, $\{\alpha, \beta\}$ label the two orbitals, and $(\cos(\theta_\mathbf{r}), \sin(\theta_\mathbf{r})) = \mathbf{r}/|\mathbf{r}|$. The function $f(\theta_\mathbf{r})$ is any function such that H_{tb} is Hermitian. The matrix elements of the corresponding Bloch Hamiltonian $H_{tb}(\mathbf{k})$, which essentially determine the band topology, encode the information about the local structure of the lattice as they involve a sum over all nearest neighbors. This is how local properties like coordination comes into the picture. As the form of H_{tb} is entirely determined by the crystal symmetry of the underlying lattice [Fu11], crystal symmetries are used for topological classification of such systems. Also, crystal symmetries are known to put constraints on bulk topological invariants [FGB12]. On some two dimensional lattices, the graph of the model, formed by identifying the sites as the vertices and the non-zero hoppings as the edges, forms a regular tiling of the two dimensional space. For such cases, the coordination number is uniquely determined by the crystal symmetry and the coordination number is hence not a separate variable that could influence the topological properties. Examples of such cases are nearest neighbor models on triangular, square and hexagonal

lattices. But on self-similar structures, to the best of our knowledge, no such correspondence has been established between coordination and spatial symmetries. It is hence important to investigate whether a change only in the local coordination of the sites can affect the topological phases on self-similar structures.

The idea of coordination is also crucial for the distinction between "bulk" and "boundary" on regular lattices. But, self-similar structures lack a clear distinction between bulk and boundary. However coordination number, and hence the notion of coordination, is well defined for self-similar structures, as those are special graphs like regular lattices. For this study, we first construct two different self-similar structures from the Sierpinski Gasket (SG), namely SG-3 and SG-4 with coordination numbers 3 and 4 respectively. These two structures, having originated from the SG, have the same Hausdorff dimension. The schematics for the construction of these structures are shown in Fig. 3.1. We then numerically study a geometry dependent non-interacting nearest neighbor Hamiltonian on both structures by looking at certain observables of interest.

Before going further into studying the role of non-spatial symmetries and coordination on the topological phases in self-similar systems, we briefly review the structures which different non-spatial symmetries impose on the Hamiltonian of a non-interacting fermionic system, following the reference [Chi+16] primarily. We do not discuss the topological classification corresponding to the symmetry classes. For details on the topological classification, one can refer to reference [Chi+16] and the references therein.

5.1 NON-SPATIAL SYMMETRIES AND THE TENFOLD CLASSIFICATION

Consider a generic non-interacting fermionic Hamiltonian $\hat{H}$. In the framework of the second quantization, $\hat{H}$ can be expressed as

$$\hat{H} = \sum_{JK} \psi_J^\dagger H_{JK} \psi_J, \tag{5.2}$$

where J, K refer to the combined labels of all the quantum numbers defining the basis states of the Hilbert space, and the $\{\psi_J^\dagger\}(\{\psi_K\})$ refer to the set of creation (annihilation) operators corresponding to the basis states. H_{JK} are the elements of a Hermitian matrix, H, which is the first quantized representation of $\hat{H}$. Any symmetry transformation in quantum mechanics can be represented by the action of an operator on the Hilbert space, which is either linear and unitary, or anti-linear and anti-unitary (Wigner's symmetry representation theorem). We introduce symmetry transformations in terms

of their actions on the fermionic creation and annihilation operators. Let us, for example, consider a linear transformation

$$\psi_J \to \psi'_J = \mathcal{U}\psi_J\mathcal{U}^{-1} = \sum_K U_{JK}\psi_K \tag{5.3}$$

where $\mathcal{U}$ is a second quantized operator acting on creation and annihilation operators whose action is represented by a linear superposition of ψ_K (for different K labels) with coefficients U_{JK} respectively. For $\mathcal{U}$ to be a symmetry operator, the system must satisfy the following invariance relations: (i) the canonical commutation relations must be preserved, and (ii) the Hamiltonian must be invariant. That is, the operator must satisfy equations

$$\{\psi_J^\dagger, \psi_K\} = \mathcal{U}\{\psi_J^\dagger, \psi_K\}\mathcal{U}^{-1} \tag{5.4a}$$

$$\mathcal{U}\hat{H}\mathcal{U}^{-1} = \hat{H} \tag{5.4b}$$

In this example, the invariance of canonical anti-commutation relations implies that U_{JK} must be elements of a unitary matrix U, and the invariance of the Hamiltonian implies that $U^\dagger H U = H$. When the action of $\mathcal{U}$ can be factorized in terms of its action on individual sites, that is when $\mathcal{U} = \Pi_j \mathcal{U}_j$ for site labels j, then we call $\mathcal{U}$ a *non-spatial* symmetry. Such symmetries are also often referred to as 'internal' symmetries as they independently act on the internal degrees of freedom of each site. Here we will briefly discuss three such symmetries, such as the time-reversal symmetry, the particle-hole symmetry, and the chiral symmetry.

5.1.0.1 *Time-reversal (TR) symmetry*

The time-reversal is an anti-unitary operator $\mathcal{T}$, whose action on fermionic creation and annihilation operators are defined by

$$\mathcal{T}\psi_J\mathcal{T}^{-1} = \sum_{JK} T_{JK}\psi_K, \quad \mathcal{T}i\mathcal{T}^{-1} = -i. \tag{5.5}$$

If a system is invariant under time-reversal symmetry, it must satisfy Eq. (5.4). For non-interacting systems, this translates to $T^\dagger H^* T = H$. The H^* appearing in the transformation in the previous line is an artifact of the anti-unitary nature of $\mathcal{T}$. The name time-reversal comes from the fact the if any operator $\hat{O}$ is invariant under TR, then $\mathcal{T}\hat{O}(t)\mathcal{T}^{-1} = \mathcal{T}e^{i\hat{H}t}\hat{O}e^{-i\hat{H}t}\mathcal{T}^{-1} = \hat{O}(-t)$ as $\mathcal{T}i\mathcal{T}^{-1} = -i$.

Eq. (5.4b) puts additional constraints on the matrix T. This can be seen by applying the TR symmetry operator twice which leads to $(T^*T)^\dagger H(T^*T) = H$. Since, H is an irreducible representation, we have $T^*T = e^{i\theta}\mathbb{1}$ as a result of Schur's lemma and T being a unitary matrix. Also, as T is unitary, we have $T^{\mathrm{T}} = e^{i\theta}\mathbb{1}$, which implies $e^{2i\theta} = 1$. This results in two possibilities, $e^{i\theta} = \pm 1$ and hence $T^*T = \pm\mathbb{1}$. What this means in terms of the action of the TR operator on a given state is that, $\mathcal{T}^2\psi_J\mathcal{T}^{-2} = (T^*T\psi)_J = \pm\psi_J$. For systems with $\mathcal{T}^2 = -1$, invariance under TR symmetry leads to the famous Kramer's degeneracy.

5.1.0.2 *Particle-hole (PH) symmetry*

The particle-hole is a unitary operator $\mathcal{P}$, which maps the fermionic creation operators onto a superposition of fermionic annihilation operators and vice-versa. Its action is defined by

$$\mathcal{P}\psi_J\mathcal{P}^{-1} = \sum_{JK} P^*_{JK}\psi_K. \tag{5.6}$$

The Hamiltonian of a non-interacting system invariant under PH transformation would satisfy the following:

$$\begin{aligned}
\mathcal{P}\hat{H}\mathcal{P}^{-1} &= \sum_{JK} H_{JK}\mathcal{P}\psi^\dagger_J\mathcal{P}^{-1}\mathcal{P}\psi_K\mathcal{P}^{-1} \\
&= \sum_{JKXY} H_{JK}P_{JX}\psi_X P^*_{KY}\psi^\dagger_Y \\
&= \sum_{XY}(\sum_{JK} P^\dagger_{YK}H^{\mathrm{T}}_{KJ}P_{JX})(\delta_{XY} - \psi^\dagger_Y\psi_X) \\
&= \mathrm{Tr}(H) - \sum_{YX}(P^\dagger H^{\mathbf{T}}P)_{YX}\psi^\dagger_Y\psi_X) = \sum_{YX} H_{YX}\psi^\dagger_Y\psi_X
\end{aligned} \tag{5.7}$$

where the last equality is due to Eq. (5.4b). This implies that $P^\dagger H^{\mathrm{T}}P = -H$ and $\mathrm{Tr}(H) = 0$. Also, applying PH twice and repeating the same arguments as in the case of applying TR symmetry twice, we get that here also we have two possibilities $P^*P = \pm\mathbb{1}$. But, in this case, $P^*P = -1$ does not lead to any degeneracy like that of the Kramer's degeneracy. Instead, if ψ_N is an eigenstate of a PH symmetric non-interacting Hamiltonian H with energy ϵ_N, then by Eq. (5.7), ψ^*_N is an eigenstate of H with energy $-\epsilon_N$.

5.1.0.3 *Chiral symmetry*

Chiral symmetry is the combination of TR and PH symmetry, $\mathcal{S} = \mathcal{T}\cdot\mathcal{P}.$, whose action is defined as

$$\mathcal{S}\psi_J\mathcal{S}^{-1} = \sum_K (PT)_{JK}\psi^\dagger_K. \tag{5.8}$$

The invariance of the Hamiltonian (Eq. (5.4b)) under chiral symmetry results in $S^\dagger HS = -H$, with $S = P^*T^*$. Applying the chiral symmetry twice and following the same reasoning as in the previous two cases of applying the TR and PH twice, we get that $S^2 = e^\theta\mathbb{1}$. So we can absorb half the phase into S and redefine $S \to e^\theta S$, and we have $S^2 = \mathbb{1}$ for the redefined matrix S. This results in the chiral symmetry operator having eigenvalues ± 1. Invariance under chiral symmetry results in symmetric spectra of non-interacting first quantized Hamiltonian H; if ψ_N is an eigenstate of H with eigenvalue ϵ_N, then $S\psi_N$ is also an eigenstate of H but with eigenvalue $-\epsilon_N$.

5.1.0.4 *The tenfold symmetry classes*

In the previous section, we defined the non-spatial symmetries and determined the structural constraints imposed on the matrices that act on the

first-quantized non-interacting Hamiltonian, denoted as H. Now, we will delve into a discussion on the general classification of symmetries. It is crucial to highlight that the action of these non-spatial symmetries on H deviates from the standard definition of symmetry, where the first-quantized non-interacting Hamiltonian H commutes with a unitary operator. The standard unitary symmetries, which commute with the Hamiltonian, lead to a block diagonal form of the Hamiltonian. However, these non-standard symmetries play a pivotal role in classifying the symmetry properties of these irreducible blocks that lack further unitary symmetries. The original classification of these symmetries was accomplished by Altland and Zirnbauer [AZ97], and thus, it is commonly referred to as the 'Altland-Zirnbauer' symmetry classes.

To account for the complex conjugation present in the action of time reversal (TR) and particle-hole (PH) symmetries on H, we redefine $T \to T\mathcal{K}$ and $P \to P\mathcal{K}$, where $\mathcal{K}$ is the complex conjugation operator. Using these definitions, we can express the following three equations, denoted as (5.9), which describe the behavior of these non-standard symmetry operators on H:

$$T^{-1}HT = H, \quad T^2 = \pm\mathbb{1}, \tag{5.9a}$$

$$P^{-1}HP = -H, \quad P^2 = \pm\mathbb{1}, \tag{5.9b}$$

$$S^{-1}HS = -H, \quad S^2 = \mathbb{1}, \tag{5.9c}$$

For a given irreducible block of H, there exists only one TR symmetry and one PH symmetry. This can be justified as follows: Suppose there are two time reversal symmetries associated with a particular irreducible block of H. This implies that the product of these symmetries would be a unitary operator that commutes with H. Consequently, it would be possible to further reduce the blocks of H into sub-blocks, contradicting the initial assumption of having an irreducible block of H. Therefore, it is evident that there can be only 10 possible combinations of these symmetries for a system. We denote the absence of a symmetry by 0 and the presence of a symmetry by $+$ or $-$, depending on the sign of the square of the symmetry operator. Thus, for a given H, both TR and PH can each have 3 possibilities $(0, +, -)$, resulting in 9 possibilities. Additionally, there exists one more possibility where a system can have a chiral symmetry even in the absence of both TR and PH symmetries, denoted by 1. These 10 symmetry classes are summarized in Table 5.1.

5.2 THE GENERALIZED BERNEVIG-HUGHES-ZHANG MODEL

Equipped with the knowledge of the structures which are imposed by the non-spatial symmetries on the single-particle Hamiltonian of a non-interacting system, we investigate the role of symmetries on the topological

Class	T	C	S
A	0	0	0
AIII	0	0	1
AI	+	0	0
BDI	+	+	1
D	0	+	0
DIII	-	+	1
AII	-	0	0
CII	-	-	1
C	0	-	0
CI	+	-	1

Table 5.1: The ten-fold symmetry classes.

phases in fractals. To do this, we study the fermionic, generalised Bernevig-Hughes-Zhang (*BHZ*) model. We choose to study this model because of the following reasons: (i) it allows us to look into different symmetry sectors by tuning the parameters, and (ii) it allows us to examine and immediately compare the physics with that in lattice systems as the *BHZ* model is known to host topologically non-trivial quantum spin Hall insulating phases on translationally invariant lattice systems [BHZ06]. Also, this model can be easily generalized to make it depend on the geometry of the underlying motif [AS17; Aga19], hence can easily be generalised to accommodate the structural differences across self-similar graphs with different coordination numbers.

We define the model in the following way. Each site has two orbital degrees of freedom, denoted by $\alpha = \{c, d\}$, and two spin degrees of freedom, denoted by $\sigma = \pm 1$. We consider only nearest neighbor hopping. The Hamiltonian is given by

$$\hat{\mathbb{H}}_{BHZ} = M \sum_{j\sigma} \hat{\psi}^{\dagger}_{j\sigma} \tau_z \hat{\psi}_{j\sigma} - t \sum_{<jk>,\sigma} \hat{\psi}^{\dagger}_{j\sigma} \tau_z \hat{\psi}_{k\sigma} - \lambda \sum_{<jk>,\sigma} \hat{\psi}^{\dagger}_{j\sigma} \sigma \tilde{\mathcal{T}}_{jk,\sigma} \hat{\psi}_{k\sigma} \quad (5.10)$$

where $\hat{\psi}^{\dagger}_{j\sigma} = (\hat{c}^{\dagger}_{j\sigma}, \hat{d}^{\dagger}_{j\sigma})$, $\{\tau_x, \tau_y, \tau_z\}$ are the Pauli matrices for the orbital degrees of freedom, and $\tilde{\mathcal{T}}_{jk,\sigma}$ is given by

$$\tilde{\mathcal{T}}_{jk,\sigma} = \begin{pmatrix} 0 & ie^{-i\sigma\theta_{jk}} \\ ie^{i\sigma\theta_{jk}} & 0 \end{pmatrix}.$$

Here θ_{jk} denotes the angle made by the vector from the jth site to the kth site, with the x axis. M denotes the on-site energy. The real, non-negative numbers t and λ denote the hopping strengths for hopping between the same orbitals and different orbitals of nearest neighbor sites, respectively.

The two σ sectors are decoupled from each other and are time reversal partners of each other, so it suffices to study the model for one value of σ. Here we look only at the $\sigma = 1$ sector and hence the respective two-orbital Hamiltonian is given by

$$\hat{\mathbb{H}} = M \sum_j \hat{\psi}_j^\dagger \tau_z \hat{\psi}_j - t \sum_{<jk>} \hat{\psi}_j^\dagger \tau_z \hat{\psi}_k - \lambda \sum_{<jk>} \hat{\psi}_j^\dagger \mathcal{T}_{jk} \hat{\psi}_k, \tag{5.11}$$

$$\mathcal{T}_{jk} = \begin{pmatrix} 0 & ie^{-i\theta_{jk}} \\ ie^{i\theta_{jk}} & 0 \end{pmatrix}.$$

The model in Eq. (5.11) is the generalized *half-BHZ* model and is known to host topological phases on square and triangular lattices. For $\lambda = t$, this model hosts two distinct topological phases on a square lattice with Chern number 1 and -1 [BHZ06; AOP16]. However, on a triangular lattice, this model hosts a different topological phase with Chern number -2, along with a trivial phase and a topological phase with Chern number 1 [Aga19]. This is a classic example where different coordination numbers in different lattices result in emergence of different topological phases. Also, for $t = \lambda = 1/2$, this model has been studied on a fractal structure which is closely related to SG-4, but with different boundary conditions [Aga19].

We numerically study the systems by primarily looking at the localization, dynamics and the topological nature of the single-particle states at half-filling. For the numerical computations, we use KWANT code [Gro+14]. A single particle state denoted by label n can be written as

$$|\psi_n\rangle = \sum_{j\alpha} \varphi_{n,j\alpha} \, |j\alpha\rangle \tag{5.12}$$

where $\{|j\rangle\}$ denotes the basis vectors in the site basis. We study the localization of single particle states by looking at the density at any site j, given by

$$\rho_n(j) = \sum_\alpha \left|\varphi_{n,j\alpha}\right|^2. \tag{5.13}$$

Given that it is unclear how to have a sharp distinction between bulk and edge states in the case of fractal systems, we define 'bulk-like' and 'edge-like' states as follows. An eigenstate is a bulk-like state if it has finite probability density on sites which enclose the triangles belonging to more or less every generation of the SG. On the other hand, an eigenstate is an edge-like state, if it is localized on sites which enclose the triangles belonging entirely to a particular generation of the SG.

We use Kitaev's topological index to study the topological properties of the systems, which relies solely on the real space description of the system [Kit06]. This has been used in the literature to study the topological phases on self-similar structures [BCN18; Fre+20]. We first choose a subsection $\mathbf{X}$ of

Figure 5.1: Partitions of the 6th generation of **(a)** SG-4 and **(b)** SG-3, for the real space Chern number calculation. The regions **A**,**B** and **C** are marked in red, green, and blue respectively. The subsection is **X**=**A**∪**B**∪**C**

the fractal and divide it into three parts, **A**, **B** and **C**. We use the following expression for the real space Chern number

$$\nu(P) = 12\pi i(\mathrm{Tr}(APBPCP) - \mathrm{Tr}(APCPBP)) \tag{5.14}$$

where $P = \sum_k |\psi_k\rangle \langle\psi_k|$ is the projector onto the desired eigenstates. A, B, C are diagonal matrices with

$$A = \tilde{A} \otimes \mathbb{1}_{N_{orb}} \quad B = \tilde{B} \otimes \mathbb{1}_{N_{orb}} \quad C = \tilde{C} \otimes \mathbb{1}_{N_{orb}} \tag{5.15}$$

where $\tilde{A}, \tilde{B}, \tilde{C}$ denote the projectors into the sectors **A**,**B**,**C** (as shown in Fig. 5.1) respectively, and N_{orb} is the number of orbitals per site which is 2 in this case.

We also check the dynamics of the states close to the Fermi energy. To do this, we project a single particle state, initially localized in the c orbital of one of the sites of the fractal, onto a part of the eigenbasis defined by $E_{min} < E < E_F$, and then time evolve under $\mathbb{\hat{H}}$. Here, E denotes the eigenenergies of the Hamiltonian and E_F denotes the Fermi energy. E_{min} is chosen such that the energy range, (E_{min}, E_F), is small enough to look at the states near the Fermi energy but also large enough to encompass all the edge-like states below the Fermi energy. All the computations have been done with $E_{min} = -0.5$. Apart from this, we check whether the dynamics change in the presence of disorder. To do this we add an extra onsite Anderson disorder term to the Hamiltonian of the form

$$\hat{\mathbb{W}} = \sum_j \hat{\psi}_j^\dagger \tilde{W}_j \hat{\psi}_j \tag{5.16}$$

where $\tilde{W}_j = \mathrm{diag}(\epsilon_j^c, \epsilon_j^d)$ and $\epsilon_j^c, \epsilon_j^d$ are random numbers drawn from a uniform random distribution with mean $\mu = 0$ and variance W. The total Hamiltonian under which the system is time evolved then becomes $\hat{\mathbb{H}}_{dis} = \hat{\mathbb{H}} + \hat{\mathbb{W}}$.

5.3 INTERPLAY OF NON-SPATIAL SYMMETRIES AND COORDINATION NUMBER

The Hamiltonian in Eq. (5.11), can be rewritten in the following block form in *orbital* $\otimes$ *site* notation

$$\hat{\mathbb{H}} = \hat{\Psi}^\dagger \mathbb{H} \hat{\Psi}, \tag{5.17}$$

$$\hat{\Psi} = \begin{pmatrix} \hat{C} \\ \hat{D} \end{pmatrix}, \quad \mathbb{H} = \begin{pmatrix} M - tH & \lambda\Delta \\ \lambda\Delta^\dagger & -(M - tH) \end{pmatrix}.$$

Here, $\hat{C}=(\hat{c}_1, \hat{c}_2, ..., \hat{c}_{N_s})^{\mathrm{T}}$ and $\hat{D}=(\hat{d}_1, \hat{d}_2, ..., \hat{d}_{N_s})^{\mathrm{T}}$, where N_s is the total number of sites. $\Delta_{jk} = -ie^{-i\theta_{jk}}$ and $H_{jk} = 1$, if j, k are nearest neighbors connected by a bond as shown in Fig. 3.1, and otherwise zero. From Eq. (5.17), it is easy to see that this model has a charge-conjugation symmetry for all values of M, t, and λ, given by

$$P^{-1}\mathbb{H}P = -\mathbb{H}. \tag{5.18}$$

Here $P = \tau_x \mathcal{K}$, where $\mathcal{K}$ is the complex conjugation operator. A consequence of this symmetry is the spectra being symmetric around zero energy. Apart from this, the Hamiltonian has other non-spatial symmetries for certain specific parameter values. So we break our results into three parts, specifically focusing on three particular parameter regimes, each belonging to a different symmetry class.

5.3.1 *Trivial case:* $t \neq \lambda = 0$

For $\lambda = 0$, the Hamiltonian in Eq. (5.17) becomes

$$\mathbb{H} = \tau_z \otimes (M - tH) \tag{5.19}$$

which is block diagonal and decouples into two single orbital tight-binding models. This is well studied in the literature on the SG-4 [Dom+83; Kim98; RT82]. The spectrum of the model (shown in Fig. 5.2) is symmetric about $E = 0$, as expected, due to the charge-conjugation symmetry (5.18) of the model. In this regime, by definition, the model has the symmetry that τ_z commutes with the Hamiltonian (5.19). As a result, even if $P^{-1}\mathbb{H}P = -\mathbb{H}$, the Hamiltonian is not considered to belong to class D of the symmetry classification as the Hamiltonian block diagonalizes into sub-blocks, each of them being belonging to class A due to absence of any other symmetries. It is already known for SG-4 that the spectrum is self similar and has infinitely many gaps in the infinite g limit. We find that the spectrum of SG-3 is also self-similar with infinitely many gaps in the infinite g limit. We confirm this numerically by computing the spectrum for different g values, and analytically by following the renormalization procedure done in [Dom+83; Kim98]. For $M = 0$, as seen in Fig. 5.2(b), we see a very high degeneracy at zero energy in case of SG-3, which is not seen in case of SG-4. The symmetry that τ_z commutes with the Hamiltonian (5.19) only gives rise to a twofold

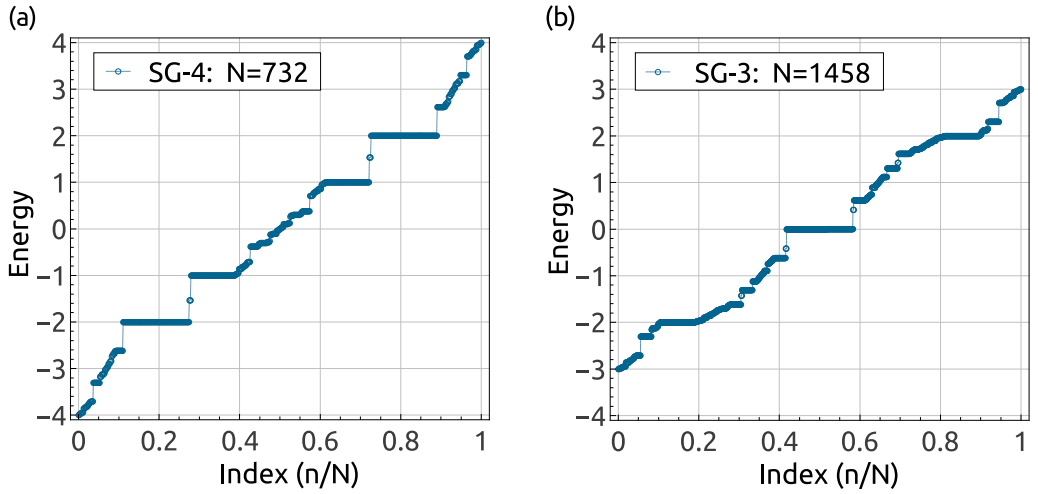

Figure 5.2: Spectrum of $\mathbb{H}$ for $\lambda = 0$, $M = 0$, and $t = 1$ on (a) SG-4 with $g = 6$ and (b) SG-3 with $g = 6$. $\mathrm{N} = 2N_s$ denotes the total number of eigenstates where N_s is the total number of sites.

degeneracy. The large degeneracy is hence a consequence of the spatial arrangement of the sites in the underlying structure and not due to any non-spatial symmetry of the Hamiltonian. In this particular regime, however, the Hamiltonian does not host any topological phases on either of the structures as H does not host any topological phase. A nonzero mass term M, simply opens up a trivial gap in the spectra.

5.3.2 *Class DIII:* $\lambda \neq t = 0$

Now we consider the case when we only have the on-site term, $c \to d$ hoppings, and $d \to c$ hoppings. Then the Hamiltonian matrix $\mathbb{H}$ in Eq. (5.17) reduces to

$$\mathbb{H} = M\tau_z + \lambda \begin{pmatrix} 0 & \Delta \\ \Delta^\dagger & 0 \end{pmatrix} \overset{def}{=} M\tau_z + \lambda H_{xy}. \tag{5.20}$$

We start by studying $\mathbb{H}$ for $M = 0$. We see that every energy level is at least doubly degenerate on both the structures. This is because H_{xy} has an additional orbital symmetry given by $\tau_z H_{xy} \tau_z = -H_{xy}$ along with the charge-conjugation symmetry (5.18). Hence, the system possesses time-reversal symmetry given by $T^{-1} H_{xy} T = H_{xy}$, where $T = i\tau_y \mathcal{K}$. So, H_{xy} then belongs to the symmetry class $DIII$. The presence of time-reversal symmetry with $T^2 = -1$ results in the Kramer's degeneracy. If $|\psi\rangle = (C, D)^{\mathrm{T}}$, where $C = (c_1, c_2, .., c_{N_s})^{\mathrm{T}}$ and $D = (d_1, d_2, .., d_{N_s})^{\mathrm{T}}$, is an eigenstate of H_{xy}, then $T|\psi\rangle = (-D^*, C^*)^{\mathrm{T}}$ is also an eigenstate of H_{xy}. As $T^2 = -1$, ψ and $T\psi$ distinct states which are orthogonal to each other ($\langle\psi|T\psi\rangle = 0$), hence leading to a two-fold degeneracy.

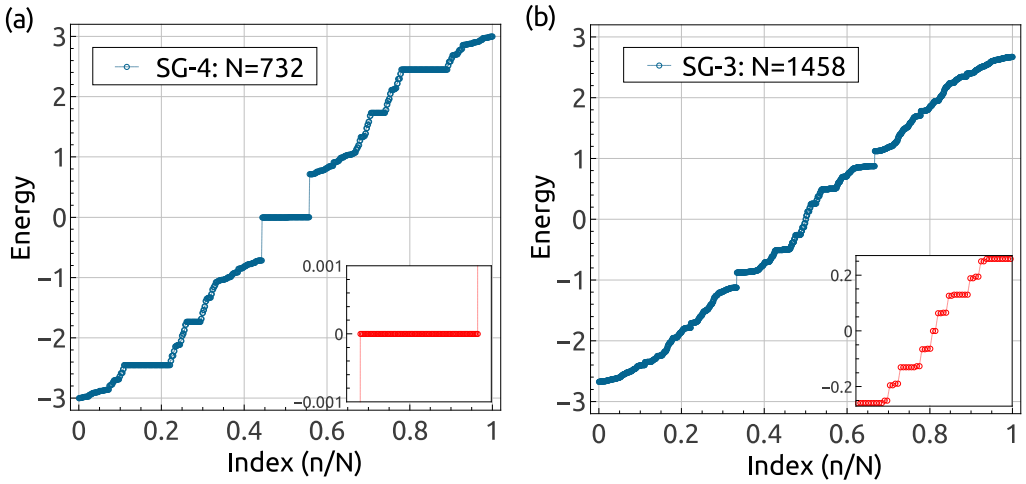

Figure 5.3: Spectrum of H_{xy} on (a) SG-4 with $g = 6$ and (b) SG-3 with $g = 6$. $N = 2N_s$ denotes the total number of eigenstates where N_s is the total number of sites. For (a), the inset shows the highly degenerate levels (flat band) at $E = 0$. For (b), the inset shows the whole range of edge-like states near zero energy.

We find that the spectrum of H_{xy} on SG-4 hosts highly degenerate levels at the Fermi energy (Fig. 5.3(a)), which is not present in the case of SG-3. The Chern number for the collection of degenerate levels at E_F turns out to be zero, when computed using Eq. (5.14). On SG-3, H_{xy} hosts doubly degenerate zero energy states. Interestingly, these zero energy states are edge-like states, completely localized on the sites present on the triangle of the 1st generation. In fact, we observe that all states close to zero energy, shown in the inset of Fig. 5.3(b), are edge-like states. A few examples of such states are shown in Fig. 5.5. In this case also, we find the Chern number to be zero, when computed by projecting onto the filled states (half-filling). However, looking at the dynamics of the edge-like states close to the Fermi energy, we find two modes of opposite chirality being present in the system (shown in Fig. 5.6). We also check the wave-packet dynamics in presence of weak Anderson disorder (shown in Fig. 5.7) and find this characteristic in the dynamics being robust to weak disorders. The presence of robust edge-states is a signature of a topologically non-trivial phase. So, H_{xy} is topologically non-trivial on SG-3 and the Chern number being zero is merely a consequence of the time-reversal symmetry in the system.

We verify this by looking at the spectral flow by threading a flux tube through the structures as was done in chapter 4. One such example of the positions flux tube in the structures SG-3 and SG-4 is shown in Fig. 5.4(a,b). For SG-3, we find that indeed the system undergoes spectral flow at half-filling (Fig. 5.4(c)). In fact, we find that system is topological for a wide range fillings around $E = 0$. The Kramer's pair break their degeneracy as the flux is threaded thorough the loop, resulting in the positive and negative spectral flow for a states initially degenerate at $\phi = 0$. This shows that the topological classification here would correspond to that of the Z_2 classification which

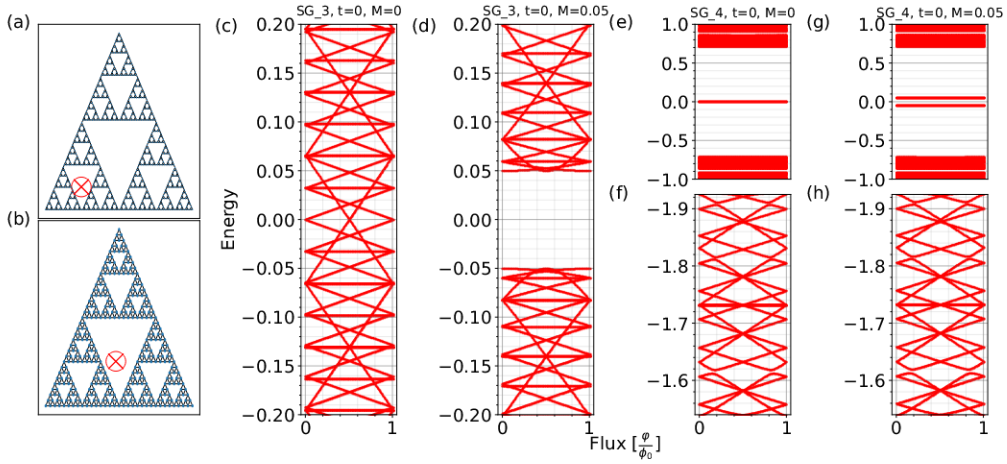

Figure 5.4: Spectral flow of the system in the regime $t = 0$. The position of the flux tubes are shown for SG-3 and SG-4 are shown in (a) and (b) respectively. The spectral flow for SG-3 for $M/\lambda = 0$ and $M/\lambda = 0.05$ are shown in (c-d). The spectral flow for SG-4 for $M/\lambda = 0$ and $M/\lambda = 0.05$ are shown in (e-h).

one expects for gapped topological system of class $DIII$ in both one and two dimensional systems. For SG-4, we find that the states in the zero energy manifold do not undergo any spectral flow showing that they are indeed topologically trivial (shown in Fig. 5.4(e)). These states are gapped from the rest of the spectrum. Interestingly, we find that the states in the rest of the spectrum do undergo spectral flow as shown in Fig. 5.4(f).

Here, we would like to point out that H_{xy} has a gapless spectrum on the square lattice and the triangular lattice, with Dirac cones at the high symmetry points of their respective Brillouin zones. Their corresponding Bloch Hamiltonians are given by,

$$H_{xy}^{sq}(\vec{\mathbf{k}}) = \sin(k_x)\sigma_x + \sin(k_y)\sigma_y$$

for the square lattice, and

$$\begin{aligned} H_{xy}^{tri}(\vec{\mathbf{k}}) &= 2(\sin(k_x) + \sin(k_x/2)\cos\left(\sqrt{3}k_y/2\right))\sigma_x \\ &+ 2\sqrt{3}\cos(k_x/2)\sin\left(\sqrt{3}k_y/2\right)\sigma_y \end{aligned}$$

for the triangular lattice. As these systems are not gapped, these do not fall under the usual classification of gapped topological phases in terms of the tenfold symmetry classes. The system has time-reversal symmetry ($T^2 = -1$) and hence has Kramer's degeneracy, thus preventing chiral dynamics in the system.

In 2-dimensional two band Chern insulators (absence of time-reversal symmetry), the forward and the backward moving modes are localized on edges which are spatially separated and this prevents the possibility of scattering between them. However, in the presence of Kramer's degeneracy, each

edge-mode is accompanied by its Kramer's degenerate counterpart which moves in the opposite direction on the same edge. So the scattering between the Kramer's pairs cannot be prevented unless there is an additional spin (or spin-like) degree of freedom to couple to the edge-modes, thus making them helical. Considering H_{xy} on 2-dimensional translationally invariant systems, H_{xy} puts two orbitals on each lattice site, thus making it a two band model if the underlying motif is a Bravias lattice. Hence, H_{xy} does not have any additional spin (or spin-like) degree of freedom and no chiral or helical edge dynamics can be observed for H_{xy} on square or triangular lattices. In this context, the wavepacket dynamics of H_{xy} on SG-3 is particularly interesting. Here, the two counter propagating edge-like modes shown in Fig. 5.6 do not scatter among themselves even in the presence of disorder (Fig. 5.7). Notice that the arguments used earlier to describe the edge-state dynamics of H_{xy} on square and triangular lattices are no longer valid for self-similar systems due to lack of an equivalent picture for the band structure in this case. The fact that H_{xy} neither shows such dynamics on 2-dimensional lattices nor on the other self similar structure, SG-4, but only on SG-3, suggests that such dynamics is due to the interplay between the self-similarity and the local coordination of SG-3.

The $M\tau_z$ term creates a gap in the spectra of $\mathbb{H}$ (shown in Fig. 5.8) on both the structures. Spectral flows for SG-3 and SG-4 in the presence of a non-zero M are shown in Fig. 5.4(d) and Fig. 5.4(g,h) respectively. For SG-4, the flatband at zero energy splits into two flatbands with energies M and $-M$. Addition of a $M\tau_z$ term breaks the time-reversal symmetry of $\mathbb{H}$, since $T^{-1}(M\tau_z + H_{xy})T = (-M\tau_z + H_{xy})$. However, we still find the spectra of $\mathbb{H}$ on SG-3 to consist of doubly degenerate states as in the case of H_{xy}. This double-degeneracy is independent of the fractal structure and is due to non-spatial symmetries of H_{xy} as shown in subsection 5.3.2.1.

5.3.2.1 *Two-fold Degeneracy in $M\tau_z + H_{xy}$*

The two-fold degeneracy in H_{xy} is a consequence of the fact that $T^{-1}H_{xy}T = H_{xy}$. Adding a mass term, $M\tau_z$, breaks this symmetry. However, eigenstates of $M\tau_z + H_{xy}$ still form degenerate pairs. Consider an eigenstate $|\psi\rangle$ of H_{xy} with eigenvalue ϵ. Due to the symmetry $\tau_z H_{xy}\tau_z = -H_{xy}$, we have that $\tau_z|\psi\rangle$ is also an eigenstate of H_{xy} but with eigenvalue $-\epsilon$. Notice that addition of the $M\tau_z$ term also breaks this symmetry. Here, we analytically show that the effect of the $M\tau_z$ term is to hybridize $|\psi\rangle$ and $\tau_z|\psi\rangle$.

We assume an ansatz eigenstate of $M\tau_z + H_{xy}$ of the form $\alpha|\psi\rangle + \beta\tau_z|\psi\rangle$, with eigenvalue E. We have the following equation

$$\Big(M\tau_z + H_{xy}\Big)(\alpha|\psi\rangle + \beta\tau_z|\psi\rangle) = \Big(\beta M + \alpha\epsilon\Big)|\psi\rangle + \Big(\alpha M - \beta\epsilon\Big)\tau_z|\psi\rangle = E(\alpha|\psi\rangle + \beta\tau_z|\psi\rangle). \quad (5.21)$$

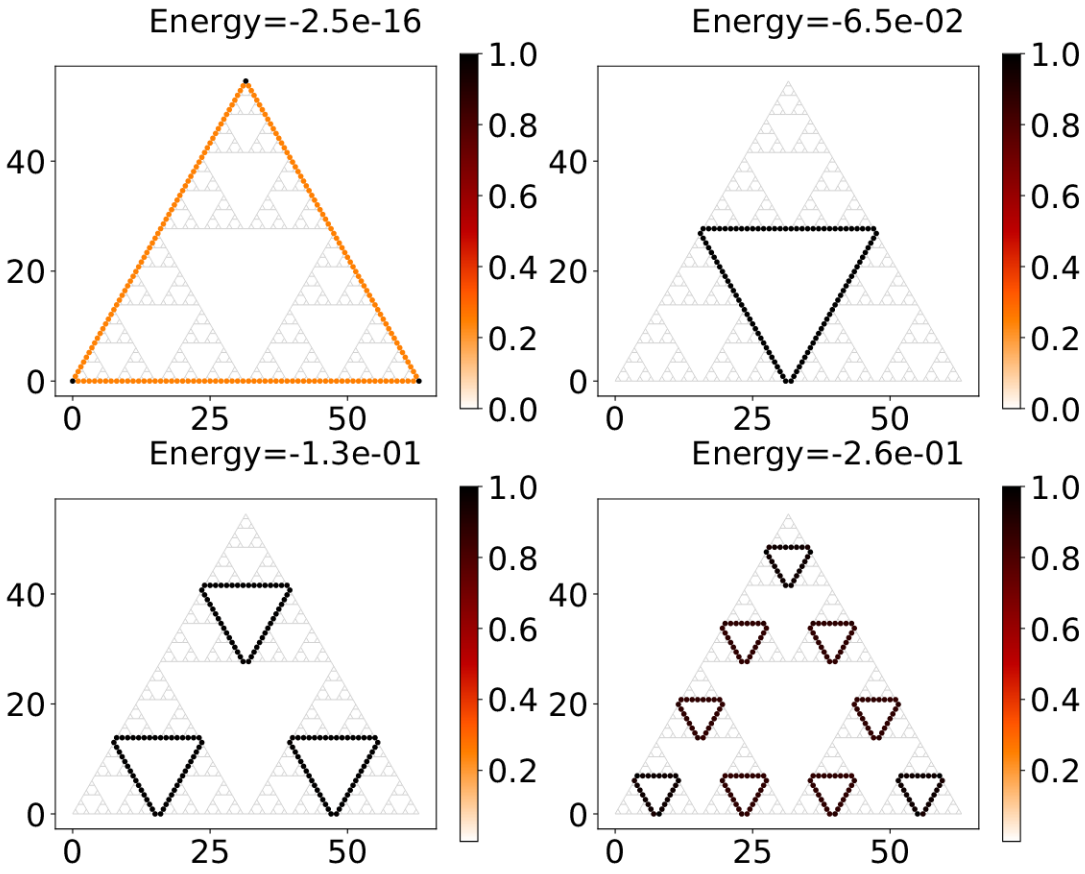

Figure 5.5: Few examples of edge-like eigenstates of H_{xy} on SG-3 with $g = 6$, close to zero energy. The color bar represents the relative density per site of an eigenstate, $|\psi_n\rangle$, defined by $\rho_n(j)/\max(\rho_n(j))$.

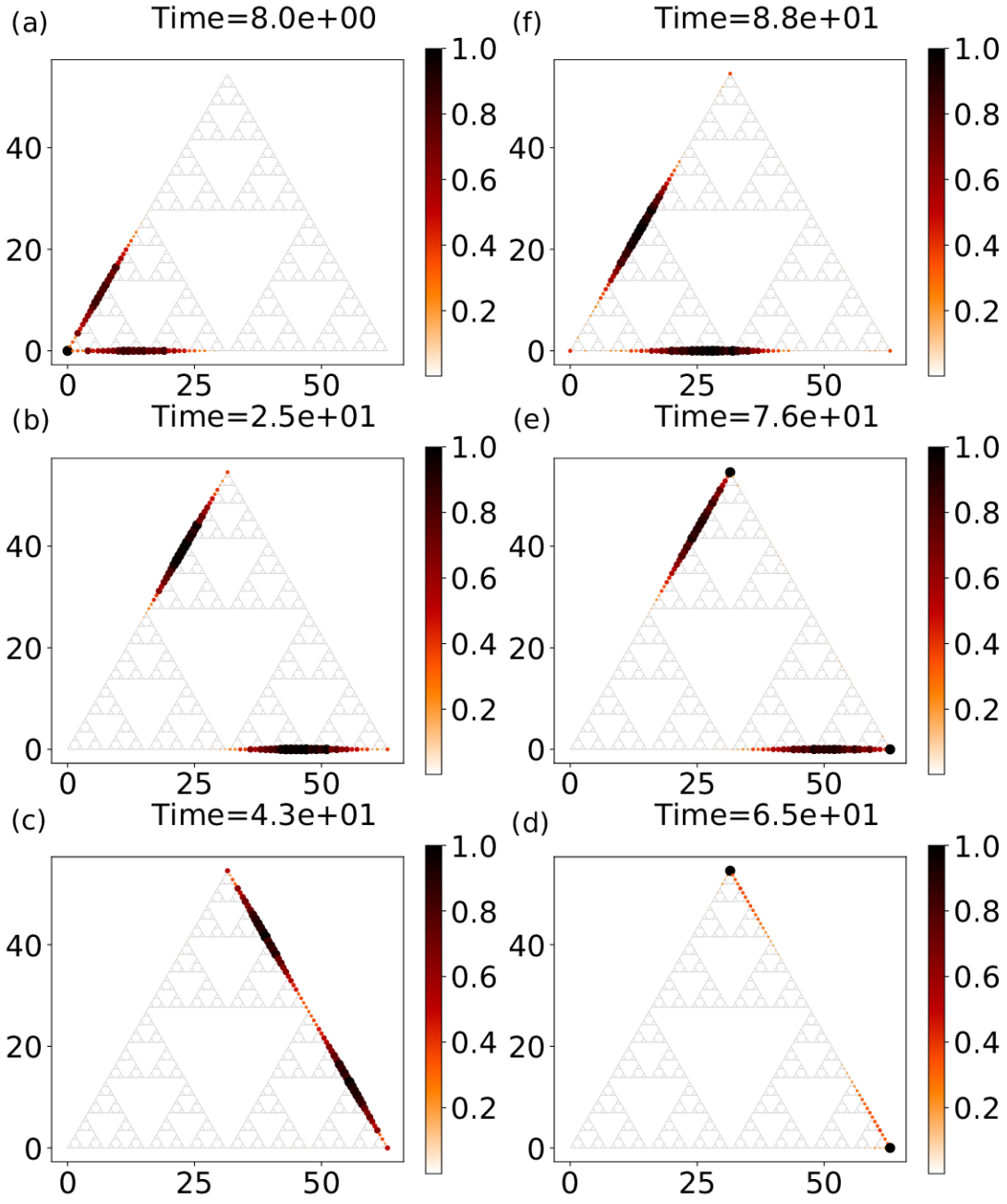

Figure 5.6: Time evolution of a state (a→b→c→d→e→f), initially localised in the c orbital of one of the corner sites on SG-3 with $g = 6$, evolved under $\hat{\mathbb{H}}$ ($t = 0$, $\lambda = 1$). The initial state is projected onto a sector defined by $-0.5 < E < 0$. The color bar represents the relative density per site of an eigenstate, $|\psi_n\rangle$, defined by $\rho_n(j)/\max(\rho_n(j))$.

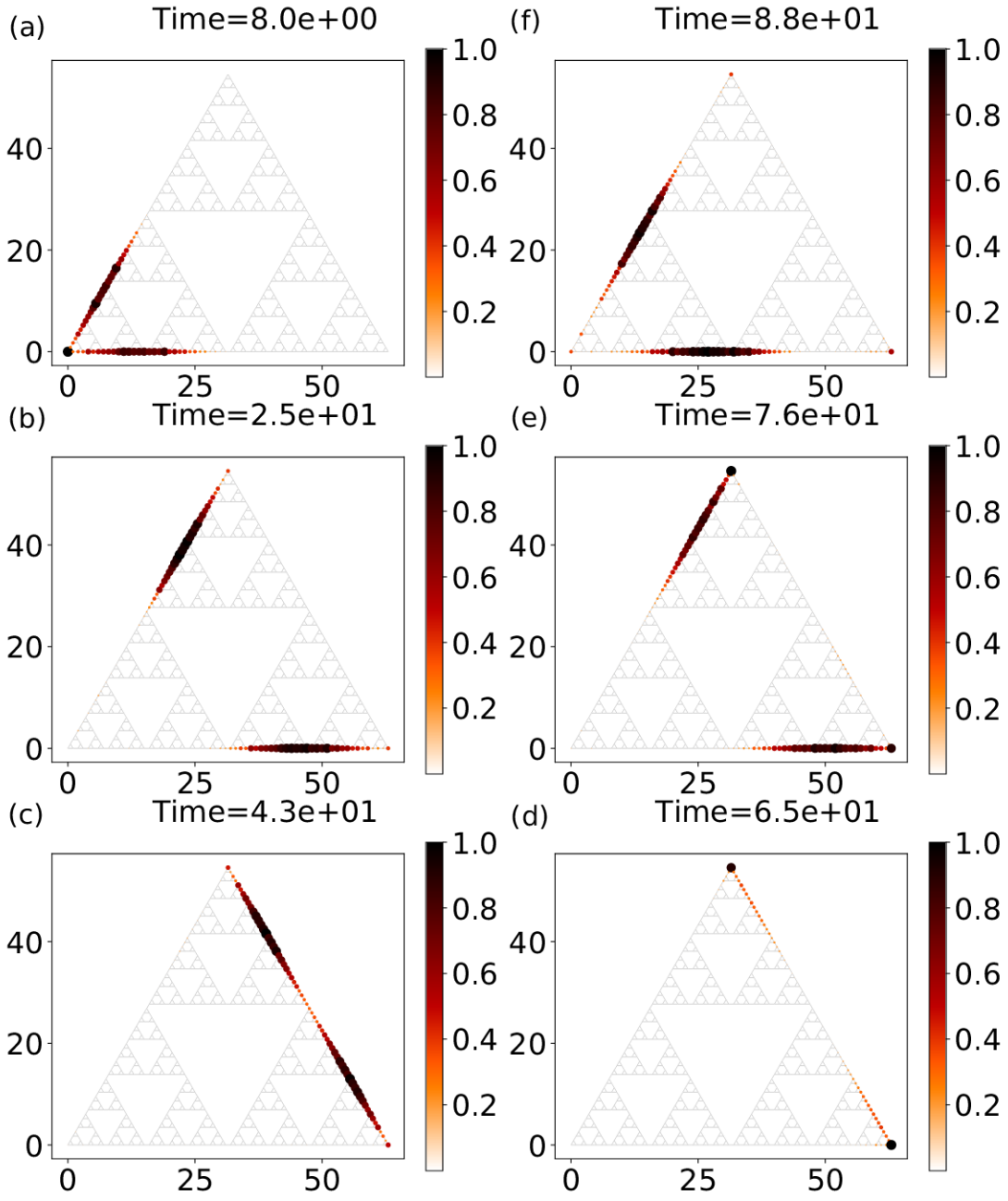

Figure 5.7: Time evolution of a state (a→b→c→d→e→f), initially localised in the c orbital of one of the corner sites on SG-3 with $g = 6$, evolved under $\hat{\mathbb{H}}_{dis}$ ($t = 0$, $\lambda = 1$) with $W = 0.1$. The initial state is projected onto a sector defined by $-0.5 < E < 0$. The color bar represents the relative density per site of an eigenstate, $|\psi_n\rangle$, defined by $\rho_n(j)/\max(\rho_n(j))$.

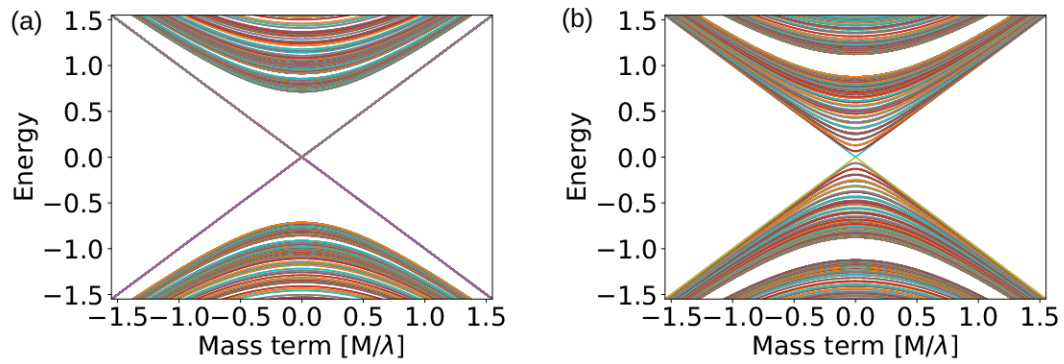

Figure 5.8: Part of the spectra of $M\tau_z + H_{xy}$ as a function of M on (a) SG-4 and (b) SG-3. The $M\tau_z$ term breaks the time-reversal symmetry and opens a gap proportional to M in the spectrum of H_{xy}.

For $\epsilon \neq 0$, we have that $|\psi\rangle$ and $\tau_z |\psi\rangle$ are orthogonal because they are eigenstates of H_{xy} with different eigenvalues. Defining $\epsilon' = \epsilon/M$ and $E' = E/M$, and equating the coefficients of $|\psi\rangle$ and $\tau_z |\psi\rangle$ in Eq. (5.21), we get

$$\beta + \alpha\epsilon' = \alpha E' \quad ; \quad \alpha - \beta\epsilon' = \beta E'. \tag{5.22}$$

Solving the pair of equations in (5.22) for α, β and E, we get

$$\frac{\alpha_\pm}{\beta_\pm} = \epsilon' \pm \sqrt{1+\epsilon'^2} \quad ; \quad E_\pm = \pm\sqrt{M^2+\epsilon^2}. \tag{5.23}$$

So we have shown that $\alpha_\pm |\psi\rangle + \beta_\pm \tau_z |\psi\rangle$ are eigenstates of $M\tau_z + H_{xy}$ with $\alpha_\pm, \beta_\pm$ satisfying Eq. (5.23).

Now, as $P^{-1}(M\tau_z + H_{xy})P = -(M\tau_z + H_{xy})$, with $P = \tau_x\mathcal{K}$, we have that $P|\Phi\rangle$ is an eigenstate of the Hamiltonian, $M\tau_z + H_{xy}$, with eigenvalue $-\xi$, if $|\Phi\rangle$ is an eigenstate with eigenvalue ξ. Hence, $|\Psi_+\rangle = \alpha_+ |\psi\rangle + \beta_+\tau_z |\psi\rangle$ and $P|\Psi_-\rangle = P\Big(\alpha_- |\psi\rangle + \beta_-\tau_z |\psi\rangle\Big)$ are both eigenstates of the Hamiltonian, $M\tau_z + H_{xy}$, with the same eigenvalue E_+. Notice that the states, $|\Psi_+\rangle$ and $P|\Psi_-\rangle$, are orthogonal to each other, as $|\psi\rangle$, $P|\psi\rangle$, $\tau_z|\psi\rangle$ and $P\tau_z|\psi\rangle = -T|\psi\rangle$, are mutually orthogonal. The states $|\psi\rangle$ and $P\tau_z|\psi\rangle$ are orthogonal to the states $P|\psi\rangle$ and $\tau_z|\psi\rangle$ as they are eigenstates of H_{xy}, a Hermitian operator, with different eigenvalues. $P|\psi\rangle = -T\tau_z|\psi\rangle$ and $\tau_z|\psi\rangle$ are orthogonal as $|\psi\rangle$ and $T|\psi\rangle$ are orthogonal to each other as shown in section 5.3.2. Hence $|\Psi_+\rangle$ and $P|\Psi_-\rangle$ cannot be the same state. This shows the existence of degenerate pairs even after the addition of the symmetry breaking term, $M\tau_z$. However, for $\epsilon = 0$, which corresponds to the zero energy modes of H_{xy}, the above argument no longer holds as $|\psi\rangle$ and $\tau_z|\psi\rangle$ no longer need to be orthogonal. Instead $|\psi\rangle$ and $\tau_z|\psi\rangle$ are eigenstates with energies $\pm M$.

5.3.3 *Class D:* $t = \lambda \neq 0$

Switching on both $[c \to c, d \to d]$ and $[c \to d, d \to c]$ hoppings brings a lot of interesting physics into the picture. From Fig. 5.9, we find that $\mathbb{H}$ hosts topological phases on both the structures. In the regime $0 \lesssim (M/\lambda) \lesssim 2.5$, both SG-3 and SG-4 host topological phases with the same Chern number $\nu = 1$ and support edge-like states. For SG-4 with different boundary conditions, similar edge-like states were reported [Aga19], which were robust against random onsite disorder, and possessed a chiral nature. In our case also, we find the same for both SG-3 and SG-4 in this regime.

To serve as a reference for studying the real space Chern number computations, we also compute the Chern number for the model on a triangular lattice using Eq. 5.14, with a system size comparable to that of the fractals. The results are shown as the green curve in Fig. 5.9(a) and (b). Due to the strong dependence of Eq. 5.14 on the system size, the transitions from one Chern number to the other is not very sharp. So the real space Chern number is only strongly quantized away from the transition region. A detailed numerical computation on the strength of the quantization of the real space Chern number on crystal lattices is presented in Fig. 4 in reference [BR11].

In the regime, $-2 \lesssim (M/\lambda) \lesssim -1.2$, SG-3 and SG-4 host different topological phases, characterized by different Chern numbers. For SG-4, in the regime, $-1.6 \lesssim (M/\lambda) \lesssim -1.3$, where there are no level crossings, we find the Chern number to be transitioning towards $\nu = -2$. Although we do not see a good enough quantization of the Chern number numerically, we do find edge-like states and chiral wave-packet dynamics in this regime, suggesting that the phase is not trivial. Also, the localization pattern of edge-like states in this regime is different from that of the regime with $\nu = 1$ (see Fig. 5.10), suggesting $\nu = -2$ as opposed to $\nu = -1$ for this regime. For SG-4, there are many level crossings in the regime $-2 \lesssim (M/\lambda) \lesssim -1.6$ (Fig. 5.11). The number of level crossings increases with generation of the fractal. Given that the Chern number is not well defined at level crossings, the computation using Eq. (5.14) does not give a definitive value (Fig. 5.9(a)).

For SG-3, there is exactly one level crossing at $(M/\lambda) \approx -1.24$, which seems to be one of the transition points from a topological phase to a trivial phase. In the regime, $-2 \lesssim (M/\lambda) \lesssim -1.24$, we find a topologically nontrivial phase with $\nu = 1$ on SG-3, which is different from what we found for SG-4. Although the Chern number computation for smaller generations shows a small dip around $(M/\lambda) \approx -1.24$ (see the red and black curve in Fig. 5.9(b)), this dip vanishes as we do the computation for higher generations (blue curve in Fig. 5.9(b)). This shows that for $t = \lambda \neq 0$, SG-3 hosts a trivial phase and only one topological phase with $\nu = 1$ in the thermodynamic limit.

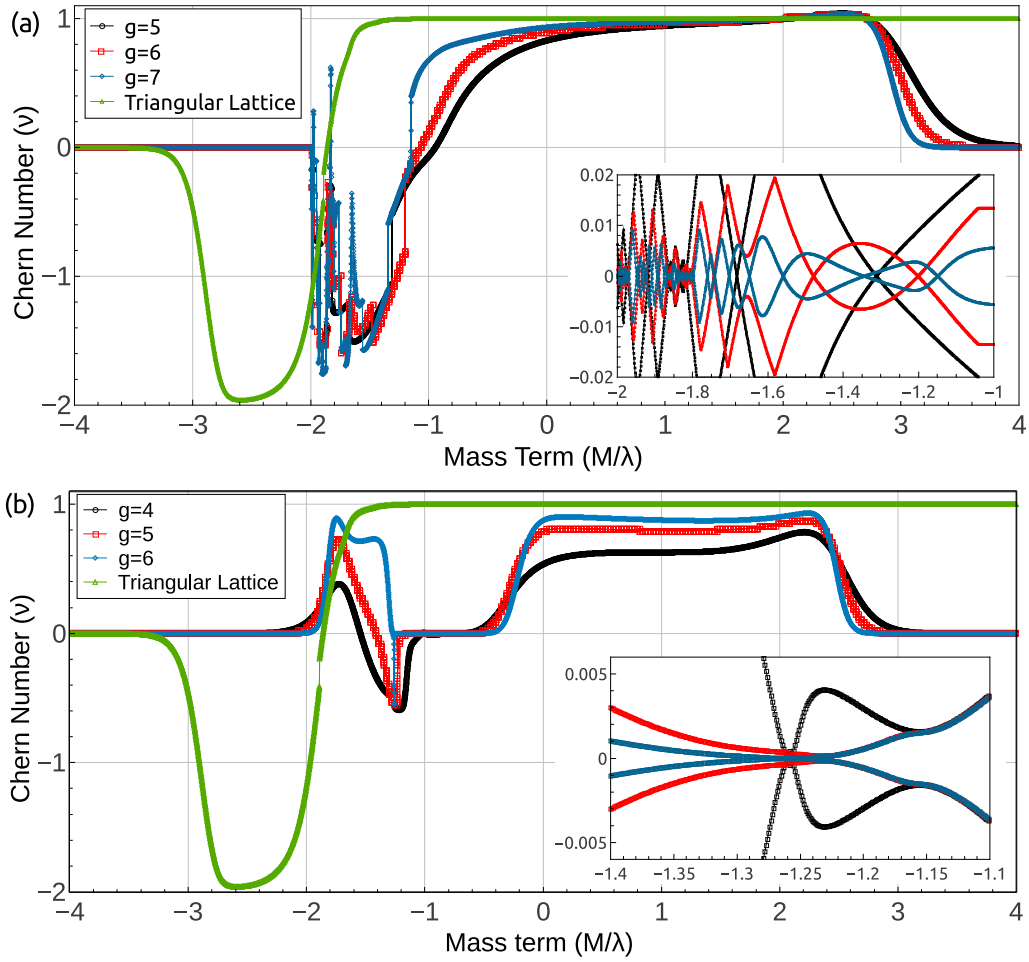

Figure 5.9: Real space Chern number for $\mathbb{H}$ in the regime $\lambda = t$ on (a) SG-4 and (b) SG-3. The computation is done using Eq. (5.14), which strongly depends on the system size. We do a system size scaling by looking at Chern numbers for different generations g. The inset in each plot shows the first two energy levels closest to the Fermi energy, for different generations. The legend for the insets are the same as that for the main plots. The inset of (a) shows numerous level crossings for SG-4, which increase with g. The inset of (b) shows a single level crossing for SG-3.

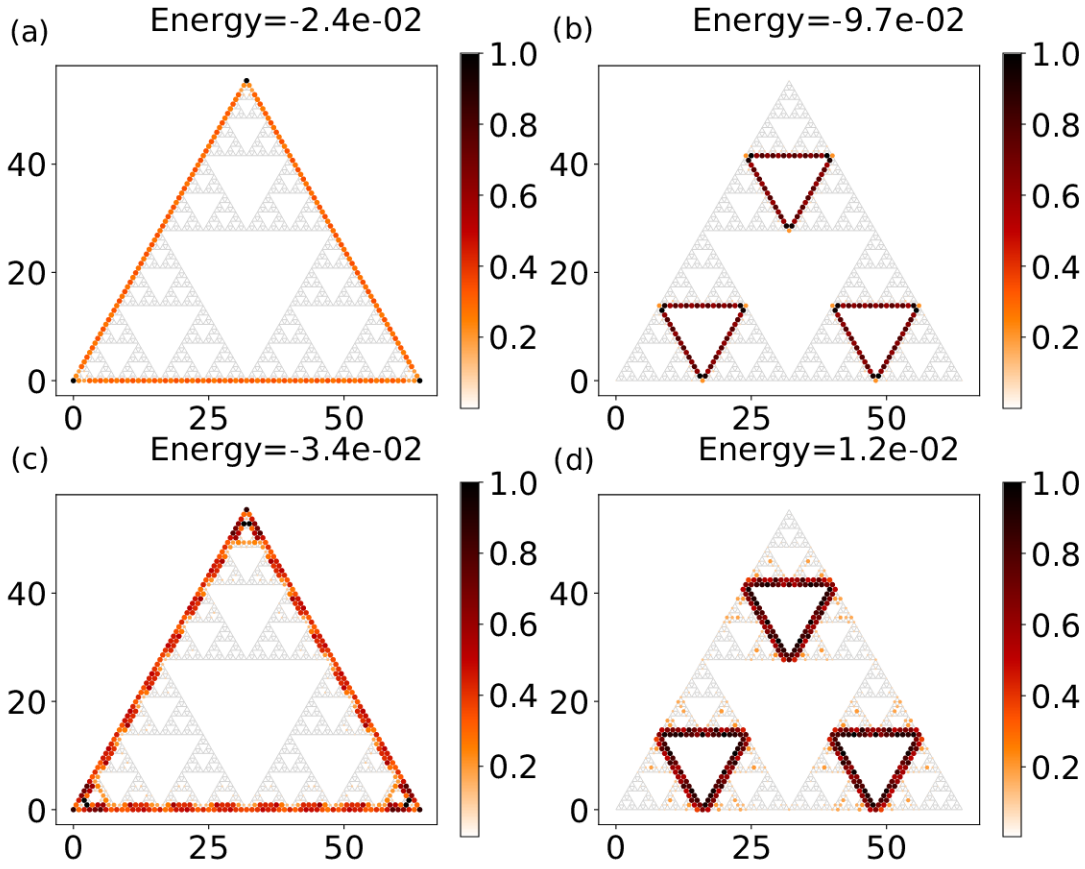

Figure 5.10: Edge-like states on SG-4. (a) and (b) are examples of edge-like states for $0 \lesssim (M/\lambda) \lesssim 2.5$ and, (c) and (d) are examples of edge-like states for $-1.6 \lesssim (M/\lambda) \lesssim -1.3$. Notice the difference in the localization pattern of edge-like states in the two regimes. For $0 \lesssim (M/\lambda) \lesssim 2.5$, the states are localized on a single layer of sites which enclose the triangles of a particular generation. In contrast, for $-1.6 \lesssim (M/\lambda) \lesssim -1.3$, the states are primarily localized on two consecutive layers of sites which enclose the triangles of a particular generation.

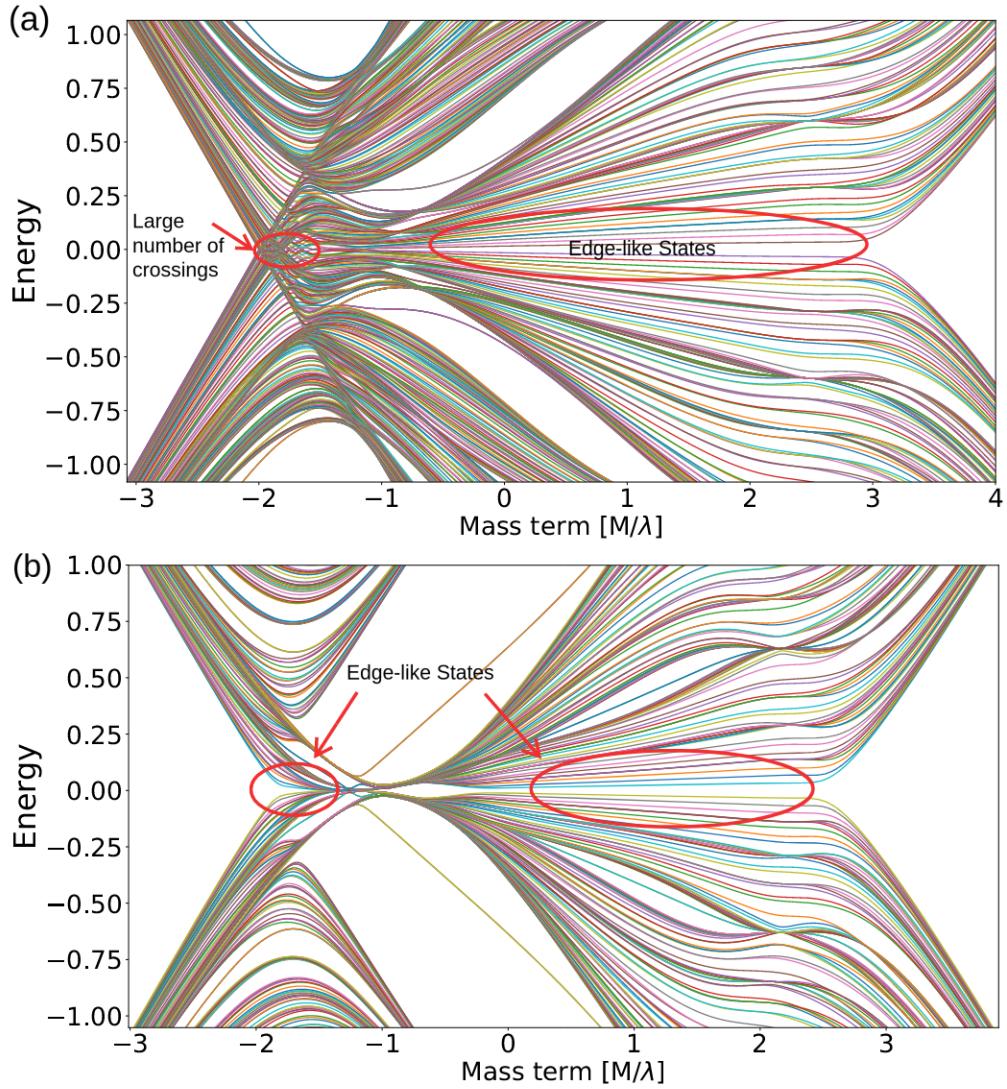

Figure 5.11: Part of the spectra for $\mathbb{H}$ in the regime $\lambda = t$ on (a) SG-4 with $g = 7$, and (b) SG-3 with $g = 6$. The regions of the spectra which host edge-like states are pointed out for both the structures. These regions correspond to the topological regions in Fig 5.9.

5.4 SUMMARY

In this chapter, we have explored the properties of a geometry dependent Hamiltonian on two different finite fractal structures (SG-3 and SG-4) which only differ in the way the sites are coordinated. The Hamiltonian has different non-spatial symmetries for different parameter regimes. We study the systems in each of these parameter regimes separately and find that the topological properties of this Hamiltonian are significantly different on the two structures. Since, the distinguishing factor between the two structures is their coordination number, we arrive at the conclusion that there is a significant interplay of non-spatial symmetries and the way the sites are coordinated, resulting in the topological properties being dependent significantly on the way the sites are coordinated. Till now we have studied topological phases on non-interacting self-similar systems. In the next part, we go on to study an interacting model which hosts topological phases on self-similar structures.

Part III

INTERACTING MODELS

This section focuses on exploring topological phases within interacting models found on self-similar structures. The next chapter will delve into our current research on chiral spin-liquids on the Sierpinski Gasket. To wrap things up, we'll conclude this document by summarizing our overall understanding of topological phases in self-similar structures and provide some thoughts on what future research avenues might hold.

6 CHIRAL SPIN-LIQUIDS ON SELF-SIMILAR STRUCTURES

In the previous chapters, we generalized the notion of topological phases in non-interacting systems on to self-similar structures. This raises the question about the possibility of the existence of topologically ordered quantum many-body phases on self-similar systems. Topologically ordered many-body phases exemplify exotic states of matter that defy conventional symmetry breaking and exhibit unique topological properties. Quantum spin liquids (QSL), in particular, represent a subclass of these phases. They are characterized by a lack of conventional magnetic order, harboring highly entangled quantum states of spins. The interest in the study of quantum spin liquids lies in their potential to reveal emergent phenomena, including long-range entanglement and fractionalized excitations. The Kitaev model on the honeycomb lattice [Kito6] provides an exactly solvable model whose ground state is a QSL where the spin degrees of freedom fractionalize into static Z2 gauge field and Majorana fermions, featuring both abelian and non-abelian anyons [BMSo7; Lah+o8; LPo9]. In this chapter we construct an exact chiral quantum spin liquid model on a Sierpinski Gasket demonstrating the presence of a topologically ordered quantum many-body phase on a fractal.

6.1 MODEL

We consider the implementation of the Kitaev like Yao-Kivelson model [YKo7] on a 3-coordinated structure defined on the Sierpinski Gasket. This structure has been referred to as SG-3 in the previous chapters. Each site has a spin-1/2 degree of freedom. The Hamiltonian of the system is given by

$$\begin{aligned} H = &\sum_{x-links} J_x \sigma_j^x \sigma_k^x + \sum_{y-links} J_y \sigma_j^y \sigma_k^y + \sum_{z-links} J_z \sigma_j^z \sigma_k^z \\ &+ \sum_{x'-links} t_x \sigma_j^x \sigma_k^x + \sum_{y'-links} t_y \sigma_j^y \sigma_k^y + \sum_{z'-links} t_z \sigma_j^z \sigma_k^z, \end{aligned} \tag{6.1}$$

where j, k represents the labels for the sites and σ_j^α ($\alpha = x, y, z$) denotes the Pauli matrix on site j. The links are always between the sites which are nearest neighbors; we denote $< jk >$ as the link between j and k. They are uniquely defined to be either of type-x, or type-y, or type-z. The uniqueness comes from the condition that, for all sites of SG-3, all links connected to a site must be of different types. The x'-links (x-links), y'-links (y-links), and z'-links (z-links) respectively denote the links of type-x, type-y and type-z which are (are not) on the smallest triangles of SG-3. Fig. 6.1(a) shows a representation of the model by marking different types of links with different colors and labelling different links with their corresponding

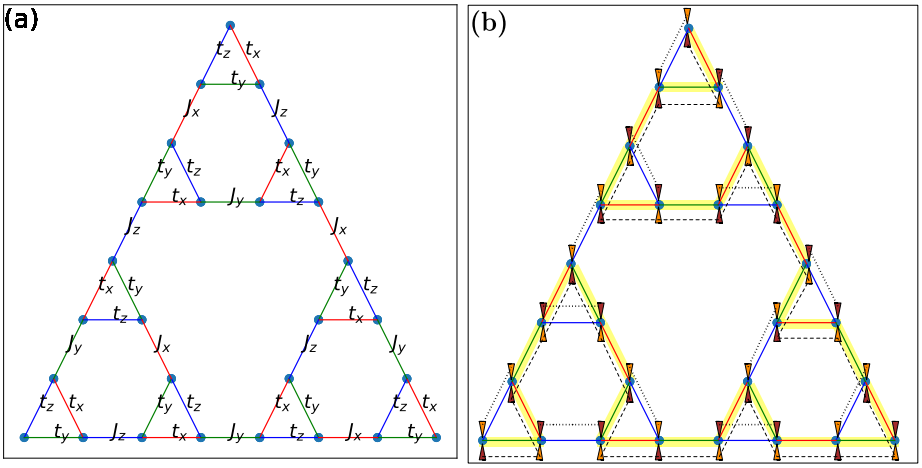

Figure 6.1: (a) Yao-Kivelson model on SG-3 with $g = 3$. The red, green and blue bonds represent the links of type-x, type-y, and type-z, respectively. Each α-link (α'-link) is labelled with its corresponding link strength, J_α (t_α). (b) Schematic representation of the Jordan-Wigner transformation of the Yao-Kivelson model on SG-3. The path highlighted in yellow, which covers all the type x and type y links in the structure, represents the Jordan-Wigner (JW) string. Each site represents a fermion given by the Jordan-Wigner transformation of the original spin-1/2 degrees of freedom. The majorana fermions, $f_j + f_j^\dagger$ and $i(f_j^\dagger - f_j)$, on each site are represented by the triangles (brown) and the inverted triangles (orange) respectively. All majorana fermions connected by the dashed line in (b) are named c majoranas and all majorana fermions connected by the dotted lines are named b majoranas.

interaction strengths. $t_\alpha(J_\alpha)$ are the link strengths for the links which are (are not) on the smallest triangles of SG-3 (shown in Fig. 6.1(a)).

6.1.1 *Conserved quantities*

Similar to the original Kitaev model [Kito6], the Hamiltonian in Eq. (6.1) also has an extensive number of conserved quantities when defined on the SG-3. To demonstrate this, we follow the notations used by Kitaev in reference [Kito6] and define link operator for a given link $< jk >$ as

$$K_{jk} = \begin{cases} \sigma_j^x \sigma_k^x, & \text{if } < jk > \text{is a type-}x \text{ link} \\ \sigma_j^y \sigma_k^y, & \text{if } < jk > \text{is a type-}y \text{ link} \\ \sigma_j^z \sigma_k^z, & \text{if } < jk > \text{is a type-}z \text{ link.} \end{cases} \tag{6.2}$$

We note that $[K_{jk}, K_{mn}] = 0$, when the links $< jk >$ and $< mn >$ do not share any common sites, or are identical, and $\{K_{jk}, K_{kl}\} = 0$ when the links $< jk >$ and $< kl >$ share a common site k. We define a loop operator for every loop on SG-3 as the product of link operators present on the loop, given by

$$W_L = K_{12} K_{23} K_{34} \cdots K_{(N-1)N} K_{N1} \tag{6.3}$$

where the sites on the loop L are indexed as $1, 2, \cdots, N$ in anti-clockwise direction from some starting site on the loop, and N is the number of sites present on the loop. For a given loop L, $[W_L, K_{jk}] = 0$, if the link $< jk >$ is not a part of the loop as K_{jk} commutes with all the link operators in W_L. If $< jk >$ is a part of loop L, then K_{jk} anti-commutes with exactly two link operators and commutes with every other link operator on the loop, resulting again in $[K_{jk}, W_L] = 0$. Also, $[K_{jk}, W_L] = 0$ if one of the sites j or k is a part of the loop L but $< jk >$ is not, as K_{jk} will anti-commute with exactly two link operators and commute with every other link operator on L. So, $[W_L, K_{jk}] = 0$ for all links $< jk >$ and all loops L in SG-3. This immediately leads to the conclusion that $[W_{L_1}, W_{L_2}] = 0$ for any two loops L_1 and L_2. Hence $[H, W_L] = 0$ for all loops L on SG-3. This means that the Hamiltonian given in Eq. (6.1) has a set of integrals of motion or conserved quantities in the form of the loop operators. Notice that $(W_L)^2 = 1(-1)$ for any loop L of even (odd) lengths; so the eigenvalues of the loop operator is $w_L = \pm 1(\pm i)$.

The number of such independent conserved quantities can be obtained by finding out the number of independent loops on the structure. A loop L is said to be independent of a set of loops $\{L_1, L_2, \cdots L_i\}$, if W_L cannot be expressed as a product of loop operators of any loops from the set. The number of sites, links, and independent loops in SG-3 of generation g are 3^g, $3(3^g - 1)/2$, and $(3^g - 1)/2$ respectively. So we clearly see that the system has an extensive number of conserved quantities as the number of independent loops in SG-3 scale linearly with the number of sites. In the subsequent sections, we show that extensive number of conserved quantities help in reducing the Hamiltonian in Eq. (6.1) to an exactly solvable quadratic Hamiltonian.

6.1.2 *Fractionalization through Hilbert space expansion*

The model defined in Eq. (6.1) is exactly solvable. To see this, we follow Kitaev's approach and expand the onsite Hilbert space by placing 2 fermions on each site. Then we identify the physical Hilbert space as both fermionic states on a given site being occupied or both being empty. The two fermions in any given site, j, can be represented by 4 majorana fermions, $\{b_j^x, b_j^y, b_j^z, c_j\}$. In majorana language, the condition to represent the physical Hilbert space hence translates to $D_j = b_j^x b_j^y b_j^z c_j = 1$. So, a state in the physical Hilbert space is obtained by projecting a state in the expanded Hilbert space with the projection operator

$$P = \Pi_j \frac{(1 + D_j)}{2} \tag{6.4}$$

We construct operators $\tilde{\sigma}_j^{\alpha} = ib_j^{\alpha}c_j$. Notice that, in the physical Hilbert space $\{\tilde{\sigma}^x, \tilde{\sigma}^y, \tilde{\sigma}^z\}$ follow the same algebra as the Pauli matrices, i.e $\tilde{\sigma}^{\alpha}\tilde{\sigma}^{\beta} = i\epsilon_{\alpha\beta\gamma}\tilde{\sigma}^{\gamma}$ and $\tilde{\sigma}^x\tilde{\sigma}^y\tilde{\sigma}^z = i$. Hence, the operator

$$\begin{aligned}\tilde{H} = &\sum_{x-links} J_x\tilde{\sigma}_j^x\tilde{\sigma}_k^x + \sum_{y-links} J_y\tilde{\sigma}_j^y\tilde{\sigma}_k^y + \sum_{z-links} J_z\tilde{\sigma}_j^z\tilde{\sigma}_k^z \\ &+ \sum_{x'-links} t_x\tilde{\sigma}_j^x\tilde{\sigma}_k^x + \sum_{y'-links} t_y\tilde{\sigma}_j^y\tilde{\sigma}_k^y + \sum_{z'-links} t_z\tilde{\sigma}_j^z\tilde{\sigma}_k^z,\end{aligned} \tag{6.5}$$

becomes the Hamiltonian in Eq. (6.1) in the physical Hilbert space. We will soon see that $\tilde{H}$ will become quadratic in terms of the $\{c_j\}$ operators, making it exactly solvable.

Writing in terms of majorana fermions, we get

$$\begin{aligned}\tilde{H} &= -i\sum_{<jk>} t_{\alpha}(ib_j^{\alpha}b_k^{\alpha})c_jc_k - i\sum_{<jk>} J_{\alpha}(ib_j^{\alpha}b_k^{\alpha})c_jc_k \\ &= -i\sum_{<jk>} t_{\alpha}\hat{u}_{jk}^{\alpha}c_jc_k - i\sum_{<jk>} J_{\alpha}\hat{u}_{jk}^{\alpha}c_jc_k.\end{aligned} \tag{6.6}$$

Given a link $< jk >$, the type of the link, α, is uniquely defined. So, we chose to suppress the superscript α from now on. We see that $[\hat{u}_{jk}, \hat{u}_{lm}] = 0$, for every link $< jk >$ and $< lm >$. Hence, all $\hat{u}_{jk} = (ib_j^{\alpha}b_k^{\alpha})$ commute with each other and with the Hamiltonian $\tilde{H}$. This is essentially the same condition that the loop operators commute with the Hamiltonian, as $K_{jk} = -i\hat{u}_{jk}c_jc_k$ in the expanded Hilbert space and all the c majoranas cancel out going around a loop. Also, $(\hat{u}_{jk})^2 = 1$ for all links; the eigenvalues, $u_{jk} = \pm 1$, for any operator, $\hat{u}_{jk}$. Plugging the eigenvalues of $\hat{u}_{jk}$ in $\tilde{H}$, we get the effective Hamiltonian

$$\tilde{H}_{maj}(\{u_{jk}\}) = \sum_{<jk>} iA_{jk}c_jc_k \tag{6.7}$$

where $\{u_{jk}\}$ is the set of u_{jk} values over all links $< jk >$ on SG-3, and $A_{jk} = t_{\alpha}\hat{u}_{jk}$ ($J_{\alpha}\hat{u}_{jk}$) if the link $< jk >$ is an (is not an) edge of the smallest triangles of SG-3. Clearly, from Eq. (6.7), we see that $\tilde{H}_{maj}$ has now become quadratic in terms of the Majorana operators $\{c_j\}$. We can think of u_{jk} as $\mathbb{Z}_2$ gauge fields. So, essentially what we have achieved is that the original interacting Hamiltonian in Eq. (6.1) is effectively reduced to a solvable quadratic Hamiltonian in Eq. (6.7) by fractionalizing the original spin-1/2 degrees of freedom into majorana degrees of freedom and $\mathbb{Z}_2$ gauge fields.

6.1.3 *Fractionalization through the Jordan-Wigner transformation*

The Hamiltonian in Eq. (6.1) can also be brought to a quadratic form with Jordan-Wigner transformation. The advantage of doing a Jordan-Wigner transformation is that in this one need not expand the Hilbert space and project it back to get the physical Hilbert space. To do the Jordan-Wigner

transformation, we first identify a path which passes through all the sites of SG-3 and covers all type x and type y links on SG-3 and name it Jordan-Wigner (JW) string (shown in Fig. 6.1(b)). This allows us to label linearly all the sites on SG-3 using a single numeric label, by going along the Jordan-Wigner string from one end to the other. The transformation maps the spin-1/2 on to fermionic degrees of freedom, given by

$$f_j^\dagger = e^{i\pi\sum_{k<j}(1+\sigma_k^z)/2}\cdot\frac{(\sigma_j^x+i\sigma_j^y)}{2} \tag{6.8a}$$

$$f_j = e^{-i\pi\sum_{k<j}(1+\sigma_k^z)/2}\cdot\frac{(\sigma_j^x-i\sigma_j^y)}{2} \tag{6.8b}$$

$$f_j^\dagger f_j = \frac{(1+\sigma_j^z)}{2}. \tag{6.8c}$$

The inverse of this transformation is given by

$$\sigma_j^+ = \frac{(\sigma_j^x+i\sigma_j^y)}{2} = e^{-i\pi\sum_{k<j}f_k^\dagger f_k}\cdot f_j^\dagger \tag{6.9a}$$

$$\sigma_j^- = \frac{(\sigma_j^x-i\sigma_j^y)}{2} = e^{i\pi\sum_{k<j}f_k^\dagger f_k}\cdot f_j \tag{6.9b}$$

$$\sigma_j^z = 2f_j^\dagger f_j - 1 \tag{6.9c}$$

Given that the Jordan-Wigner string covers all the type x and type y links in SG-3, the $\sigma_j^x\sigma_k^x$ ($\sigma_j^y\sigma_k^y$) terms in Eq. (6.1) can be written as $\sigma_m^x\sigma_{m+1}^x$ ($\sigma_m^y\sigma_{m+1}^y$) by re-labelling the sites going along the Jordan-Wigner string. Using the inverse Jordan-Wigner transformation given in Eq. (6.9), we get

$$\begin{aligned}
\sigma_m^x\sigma_{m+1}^x &= (\sigma_m^+ + \sigma_m^-)(\sigma_{m+1}^+ + \sigma_{m+1}^-)\\
&= (f_m^\dagger\Pi_{j<m}e^{-i\pi\hat{n}_j} + f_m\Pi_{j<m}e^{i\pi\hat{n}_j})\cdot\\
&(f_{m+1}^\dagger\Pi_{j<m+1}e^{-i\pi\hat{n}_j} + f_{m+1}\Pi_{j<m+1}e^{i\pi\hat{n}_j})\\
&= f_m^\dagger(1-2\hat{n}_m)f_{m+1}^\dagger + f_m^\dagger(1-2\hat{n}_m)f_{m+1}\\
&+ f_m(1-2\hat{n}_m)f_{m+1}^\dagger + f_m(1-2\hat{n}_m)f_{m+1}\\
&= f_m^\dagger f_{m+1}^\dagger + f_m^\dagger f_{m+1} - f_m f_{m+1}^\dagger - f_m f_{m+1}\\
&= (f_m^\dagger - f_m)(f_{m+1}^\dagger + f_{m+1})
\end{aligned} \tag{6.10}$$

where $\hat{n}_m = f_m^\dagger f_m$. We have used the following identities for fermions in getting Eq. (6.10); $e^{\pm i\pi\hat{n}_m} = 1-2\hat{n}_m$ to go from line 2 to line 3, and $f_m^\dagger(1-2\hat{n}_m) = f_m^\dagger$, $f_m(1-2\hat{n}_m) = -f_m$ to go from line 3 to line 4. Following a similar procedure as Eq. (6.10), one can also show that

$$\sigma_m^y\sigma_{m+1}^y = -(f_m^\dagger + f_m)(f_{m+1}^\dagger - f_{m+1}). \tag{6.11}$$

It is also straight forward to see that

$$\begin{aligned}
\sigma_j^z\sigma_k^z &= (2\hat{n}_j - 1)(2\hat{n}_k - 1)\\
&= (f_j^\dagger - f_j)(f_j^\dagger + f_j)(f_k^\dagger - f_k)(f_k^\dagger + f_k)
\end{aligned} \tag{6.12}$$

Also, notice that the links of type x and type y appear alternately in succession if one follows the Jordan-Wigner string. Taking this into account and using the results of Eqs. (6.10), (6.11), and (6.12), the Hamiltonian in Eq. (6.1) becomes

$$\begin{aligned} H &= \sum_{x-links} J_x \sigma_j^x \sigma_k^x + \sum_{y-links} J_y \sigma_j^y \sigma_k^y + \sum_{z-links} J_z \sigma_j^z \sigma_k^z \\ &+ \sum_{x'-links} t_x \sigma_j^x \sigma_k^x + \sum_{y'-links} t_y \sigma_j^y \sigma_k^y + \sum_{z'-links} t_z \sigma_j^z \sigma_k^z \\ &= \sum_m (A_x \sigma_{2m-1}^x \sigma_{2m}^x + A_y \sigma_{2m}^y \sigma_{2m+1}^y) + \sum_{\text{type}-z\ links} A_z \sigma_j^z \sigma_k^z \\ &= \sum_m (A_x (f_{2m-1}^\dagger - f_{2m-1})(f_{2m}^\dagger + f_{2m}) - A_y (f_{2m}^\dagger + f_{2m})(f_{2m+1}^\dagger - f_{2m+1})) \\ &+ \sum_{\text{type}-z\ links} A_z (f_j^\dagger - f_j)(f_j^\dagger + f_j)(f_k^\dagger - f_k)(f_k^\dagger + f_k) \end{aligned} \tag{6.13}$$

where $A_\alpha = J_\alpha (t_\alpha)$ if the link is an α-link (α'-link). Each complex fermion can be decomposed into two majorana fermions, $(f_j + f_j^\dagger)$ and $i(f_j^\dagger - f_j)$. We denote the different majorana fermions by

$$\begin{aligned} c_{2m} &= (f_{2m}^\dagger + f_{2m}); \quad b_{2m} = i(f_{2m}^\dagger - f_{2m}) \\ c_{2m+1} &= i(f_{2m+1}^\dagger - f_{2m+1}); \quad b_{2m+1} = (f_{2m+1}^\dagger + f_{2m+1}); \end{aligned} \tag{6.14}$$

where m denotes the labels of the indices based on the Jordan-Wigner string. As a result, the Hamiltonian in Eq. (6.13) becomes

$$H = \sum_m (-iA_x c_{2m-1} c_{2m} + iA_y c_{2m} c_{2m+1}) - \sum_{\text{type}-z\ links} iA_z \hat{u}_{jk} c_j c_k \tag{6.15}$$

where $\hat{u}_{jk} = ib_j b_k$. We choose to use the same notation ($\hat{u}_{jk}$) for $ib_j b_k$ as we have used for $ib_j^\alpha b_k^\alpha$ as both have the same properties and can be interpreted in the exact same way as we will see ahead. We note that u_{jk} on all the type-z links commute with each other and with the Hamiltonian as no two type-z links share a common site. This results in an extensive number of conserved quantities for the Hamiltonian making it possible to find an exact solution. These are essentially the same conserved quantities which we described in section 6.1.1, as the loop operators, W_L, can be expressed in terms of $\hat{u}_{jk}$. To see this, we note that every loop operator can be always expressed as the product of successive type-x and type-y links along the Jordan-Wigner string, along with some type-z links. And

$$K_{jk} = \begin{cases} -ic_j c_k, & \text{if } < jk > \text{is a type-}x \text{ link} \\ ic_j c_k, & \text{if } < jk > \text{is a type-}y \text{ link} \\ -i\hat{u}_{jk} c_j c_k, & \text{if } < jk > \text{is a type-}z \text{ link.} \end{cases} \tag{6.16}$$

So going along a loop, the c majoranas get cancelled out resulting in

$$W_L = -\Pi_{<j_L k_L>} (-i\hat{u}_{j_L k_L}) \tag{6.17}$$

where $< j_L k_L >$ is a type-z link on the loop. The number of type-z links is exactly equal to the number of independent loops in SG-3, showing that set of the commuting operators, $\{\hat{u}_{jk}\}$, does not add any other conserved quantities different from those arising from the loop operators. We notice that $(\hat{u}_{jk})^2 = 1$, so its eigenvalues, $u_{jk} = \pm 1$ which can be interpreted as a $\mathbb{Z}_2$ gauge field. Plugging it in Eq. (6.15), we get the effective quadratic Hamiltonian for each set of $\{u_{jk}\}$

$$H_{maj}(\{u_{jk}\}) = \sum_{<jk>} iA_{jk}c_j c_k; \quad A_{jk} = \begin{cases} -A_x, & \text{if } < jk > \text{is a type-}x \text{ link} \\ A_y, & \text{if } < jk > \text{is a type-}y \text{ link} \\ -A_z u_{jk}, & \text{if } < jk > \text{is a type-}z \text{ link} \end{cases} \tag{6.18}$$

where $\{u_{jk}\}$ is the set of u_{jk} values over all type-z links on SG-3. So, using the Jordan-Wigner transformation, we have successfully been able to reduce the original Hamiltonian in Eq. (6.1) into a quadratic Hamiltonian (Eq. (6.18)) by fractionalizing the original spin-1/2 degrees of freedom into majorana and $\mathbb{Z}_2$ gauge fields. However, unlike in section 6.1.2, we can extract the physical quantities for the original spin model by directly using the Hamiltonian in Eq. (6.18) as no expansion of Hilbert space is involved in the fractionalization process in this case.

6.2 MANY-BODY GROUND STATE

We can now use the quadratic majorana Hamiltonian given in Eq. (6.7) or Eq. (6.18) to determine the many-body ground state and the ground state energy. This has been explained in detail in reference [Kito6]. Here, we use the majorana Hamiltonian obtained from the Jordan-Wigner transformation (Eq. (6.18)) as one can directly infer the information about the degeneracy from this.

We first bring H_{maj} into the canonical form in terms of complex fermions. This can be obtained by diagonalizing the matrix iA, whose elements are given by the A_{jk}s mentioned in Eq. (6.18). Note that A is a skew-symmetric $N \times N$ matrix as $c_j c_k = -c_k c_j$. Let iA be diagonalized by matrix Q, which means $iA = Q^\dagger D Q$ where D is a real diagonal matrix. Under this basis transformation, we have

$$\begin{aligned} H_{maj}(\{u_{jk}\}) &= \sum_n \epsilon_n (\sum_j c_j Q^\dagger_{jn})(\sum_k Q_{nk} c_k) = \sum_n \epsilon_n (\sum_j Q^*_{nj} c_j)(\sum_k Q_{nk} c_k) \\ &= \sum_n \epsilon_n (\sum_j \mathrm{Re}(Q_{nj}) c_j - i\mathrm{Im}(Q_{nj}) c_j)(\sum_j \mathrm{Re}(Q_{nk}) c_k + i\mathrm{Im}(Q_{nk}) c_k) \end{aligned} \tag{6.19}$$

where $\epsilon_n = D_{nn}$ is dependent on the set of $\mathbb{Z}_2$ gauge fields $\{u_{jk}\}$. The particle-hole symmetry ($(iA)^* = -iA$) in the majorana Hamiltonian implies

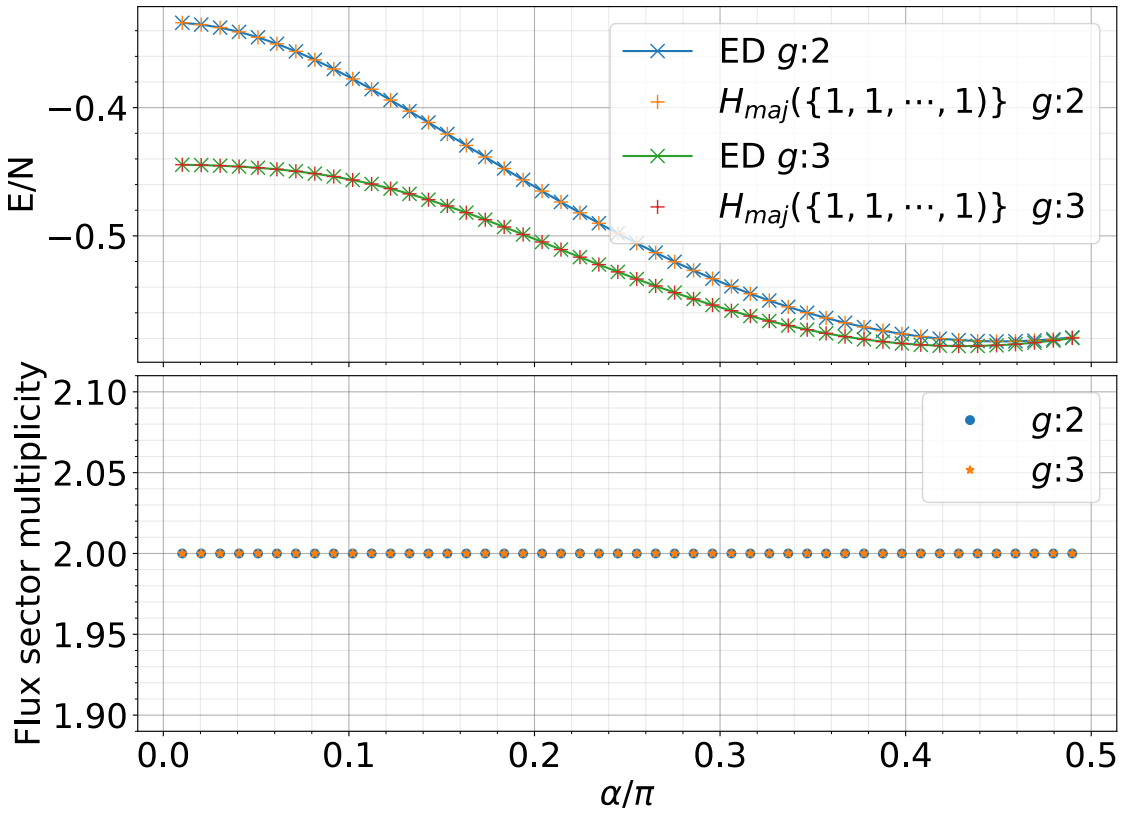

Figure 6.2: Finding the ground state flux sector. Top: The ground state energies per site obtained from the exact diagonalization of the many-body spin Hamiltonian (labeled by 'ED') and those from the quadratic majorana Hamiltonian H_{maj} in the Lieb's flux sector, as a function of the tuning parameter α. We find that for all values of α, the ground state lies in the Lieb's $\mathbb{Z}_2$ flux sector. Bottom: Number of flux sectors ('Flux sector multiplicity') having the same minimum energy E_{min} as the Lieb's flux sector. We find that only 1 other flux sector, the time-reversal partner of the Lieb's flux sector, has the same minimum energy E_{min} as the Lieb's flux sector. The system size is $N = 3^g$; the calculations are shown for $g = 2$ and $g = 3$.

that if ψ_n is an eigenvector of iA with eigenvalue ϵ_n, then ψ_n^* is also an eigenvector of iA with eigenvalue $-\epsilon_n$. This means that for every $n < N$, there exists some $n' < N$ such that $\epsilon_{n'} = -\epsilon_n$ and $Q_{n'j} = Q_{nj}^* \forall j$. Hence, we can construct canonical majorana modes defined as $c'_n = \sum_j \mathrm{Re}(Q_{nj})c_j$, $c''_n = \sum_j \mathrm{Im}(Q_{nj})c_j$, and the corresponding complex fermion operators defined as $a_n^\dagger = (c'_n - ic''_n)/2$ and $a_n = (c'_n + ic''_n)/2$. So, H_{maj} can be written in the canonical form as

$$H_{maj}(\{u_{jk}\}) = \sum_{n:\epsilon_n \geq 0} \epsilon_n (ic'_n c''_n) = \sum_{n:\epsilon_n \geq 0} \epsilon_n (2a_n^\dagger a_n - 1) \tag{6.20}$$

The minimum energy state for a given set of $\{u_{jk}\}$ is given by $a_n |\psi\rangle = 0, \forall n$ and the corresponding energy is given by $E_{min}(\{u_{jk}\}) = -\sum_{n:\epsilon_n \geq 0} \epsilon_n$.

The ground state is obtained by minimizing $E_{min}(\{u_{jk}\})$ over all possible sets of $\mathbb{Z}_2$ flux configurations, the ground state energy is given by

$$E_0 = \min(E_{min}(\{u_{jk}\})). \tag{6.21}$$

The corresponding ground state is given by

$$|\psi_0\rangle = |\psi_0^u\rangle \otimes |\psi_0^m\rangle\,, \tag{6.22}$$

where $|\psi_0^u\rangle$ represents the wavefunction for the gauge degrees of freedom in the flux configuration which minimizes $E_{min}(\{u_{jk}\})$, and $|\psi_0^m\rangle$ represents the ground state of H_{maj} (the wavefunction for the matter degress of freedom) in the same flux configuration. The degeneracy of the ground state can then be inferred from two factors: (i) the number of states $|\psi^m\rangle$ which lead to same E_{min} given a particular flux configuration, and (ii) number of $\mathbb{Z}_2$ flux configurations which minimize E_{min}. The first factor is dependent on the number of majorana zero modes in the spectrum of H_{maj}; n_M majorana zero modes result in a 2^{n_M} degeneracy in the ground state. The second factor is typically dependent on symmetries and spontaneous symmetry breaking. In this case, the Hamiltonian H has time-reversal symmetry. So the time-reversal operator $\mathcal{T}$ commutes with H and W_L for all loops. This implies that if we have a state such that $W_L|\psi\rangle = w_L|\psi\rangle$, then $\mathcal{T}W_L\mathcal{T}^{-1}\mathcal{T}|\psi\rangle = \mathcal{T}w_L\mathcal{T}^{-1}\mathcal{T}|\psi\rangle \implies W_L\mathcal{T}|\psi\rangle = w_L^*\mathcal{T}|\psi\rangle$; the action of $\mathcal{T}$ changes the w_L to w_L^*. As $\mathcal{T}$ commutes with H, the flux sector with $\{w_L\}$ and $\{w_L^*\}$ would lead to the same E_{min}. For structures where all the independent loops of even length, this has no consequence as $w_L = \pm 1$ for all loops and $\{w_L\}$ and $\{w_L^*\}$ are the same flux sector. However, for SG-3 which has triangles (loops of odd length), $\{w_L\}$ and $\{w_L^*\}$ are different flux sectors as $w_L = \pm i$ for triangles, resulting in at least a two-fold degeneracy.

We study the parameter regime $t_x = t_y = t_z = t = |\sin\alpha|$, and $J_x = J_y = J_z = J = |\cos\alpha|$. Although Lieb's theorem is not rigorously applicable for SG-3, for all values of t/J, we still find that the many-body ground state lies in the flux sector which agrees with the Lieb's principle; for a loop L, w_L has a simple form given by

$$w_L^{GS} = -(-i)^{n_z}, \tag{6.23}$$

where n_z is the number of type-z links on the loop. We call this flux sector as the Lieb's flux sector. This is equivalent to $u_{jk} = 1$ whenever $< jk >$ is a type $-\,z$ links. To verify this, we compare the ground state energies obtained from H_{maj} in the Lieb's flux sector with that obtained from the exact diagonalization of the many-body spin Hamiltonian H (see Fig. 6.2). The many-body ground state is at least two-fold degenerate due to the spontaneous breaking of the time-reversal symmetry as mentioned in the previous paragraph. This has been verified numerically by checking the number of flux sectors which result in the same E_{min} (also shown in Fig. 6.2). In the thermodynamic limit, we see a change in the ground state

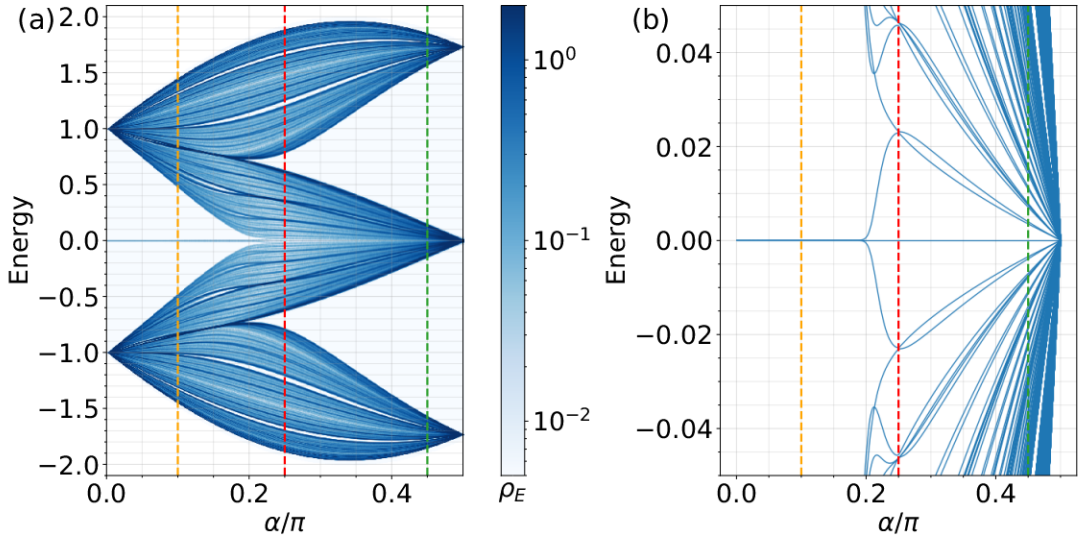

Figure 6.3: (a) Density of states (ρ_E) of H_{maj} as a function of α. (b) Low energy spectrum of H_{maj} as a function of α. The orange, red, and green dashed lines mark three values of α whose spectra and some characteristic wave functions are shown in Fig. 6.4, Fig. 6.7, and Fig. 6.8 respectively. The calculations have been done for a system with $N = 3^7$ sites with $\varepsilon = 10^{-3}$.

degeneracy due to a change in the number of majorana zero modes. The number of majorana zero modes changes from three to one across $\alpha \approx 0.2$ as $t/J = |\tan\alpha|$ is increased (shown in Fig. 6.3). This results in a change in the degeneracy of the many-body ground state; the ground state is sixteen-fold degenerate for $\alpha \lesssim 0.18\pi$ to a four-fold degenerate for $\alpha \gtrsim 0.22\pi$. We discuss this in detail in the following sections.

6.3 MAJORANA SPECTRA AND TOPOLOGICAL PHASES

We study the ground state properties of H by studying the spectrum of H_{maj} in the Lieb's flux sector in the parameter regime $t_x = t_y = t_z = t = |\sin\alpha|$, and $J_x = J_y = J_z = J = |\cos\alpha|$. H_{maj} can be interpreted as a standalone tight-binding model defined on a self-similar graph. So, we expect it to have the general features of the tight-binding models defined on self-similar graphs. To verify this, we look at the normalized density of states (ρ_E) (given in Eq. (3.8)) as a function of α (shown in Fig. 6.3(a)). We index the states according to increasing energies. The presence of particle-hole symmetry due to the majorana fermions makes the spectrum of H_{maj} symmetric about $\varepsilon = 0$, which implies $\varepsilon_{[N/2]-k} = -\varepsilon_{[N/2]+k}$ ([..] represents the floor function, N is the number of eigenvalues in the spectrum). As a result, the state with index $[N/2]$ has zero energy being protected by the particle-hole symmetry. We also find that the spectrum is self-similar in nature away from $\alpha = 0$ and $\alpha = \pi/2$ which is characteristic of the tight-binding models on SG-3 as seen in previous chapters. One of the consequences of the self-similar spectra is that the spectra is primarily dominated by low regions of ρ_E (shown in Fig.

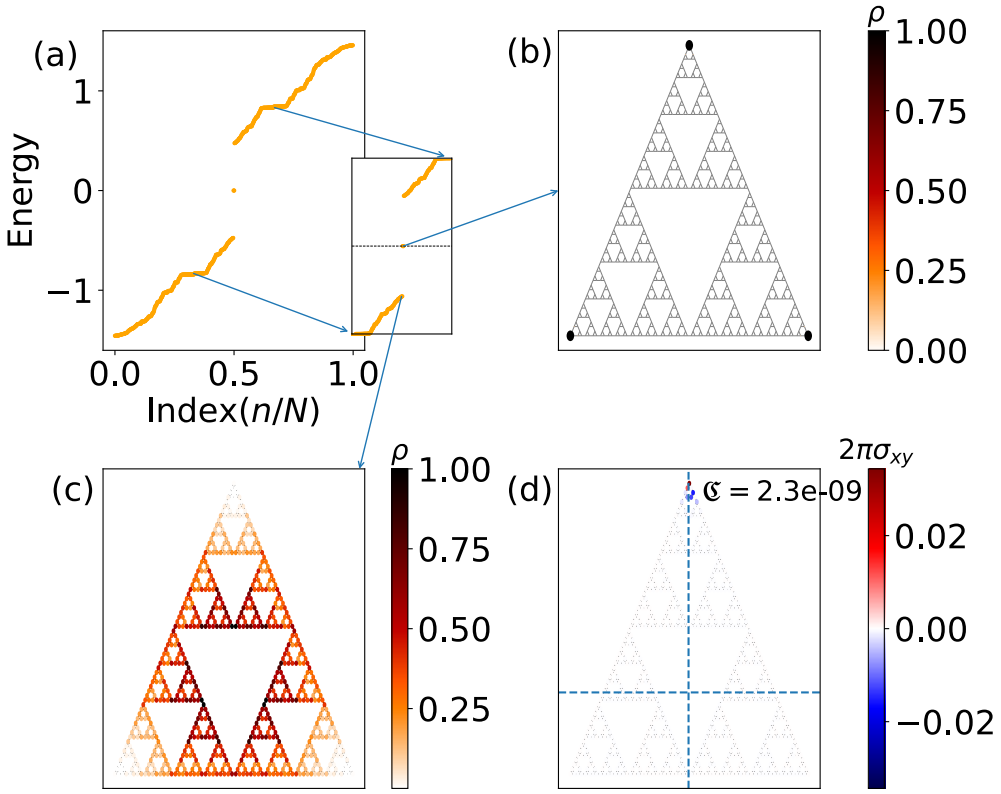

Figure 6.4: Spectrum and wavefunctions of H_{maj} for $\alpha = \pi/10$ ($t < J$). (a) Spectrum of H_{maj} and a zoomed in version of the same in the inset, showing the gap opening and the presence of triply degenerate zero modes. (b) Localization of the zero modes on the corner sites. (c) Localization of the states at the edges of the gap. Arrows are drawn from the inset of (a) to (b) and (c) to show the corresponding energies the states whose localization has been shown in (b) and (c). (d) Local Hall conductivity at half-filling. The position of the cross-hair for the local Hall conductivity calculation is shown with the dashed lines in (d). The calculation has been done for $N = 3^6$ sites.

6.3 (a)).

H_{maj} has different properties for different regimes of α. Fig. 6.3(b) shows the low energy part of the spectra as a function of α. Given that H_{maj} is in principle a tight-binding model on a self-similar structure, we use the tools we developed in the previous chapters to study the properties of H_{maj}. Fig. 6.3 shows a quantum phase transition as a function of the tuning parameter α as we clearly see a transition from a gapped phase ($\alpha \lesssim 0.2$) to a seemingly gapless phase ($\alpha \gtrsim 0.2$). We study these phases in detail by looking at the localization of the single particle wave functions. Like in chapter 4, for the numerics, given a state $|\psi\rangle = \sum_j \psi_j |\mathbf{r}_j\rangle$, the localization is shown by computing the normalized onsite density, $\rho_j = |\psi_j|^2/\max(|\psi_j|^2)$. We also study the topological aspect by looking at the local Hall conductivity as defined in section 4.3 by defining a Chern number similar to that in Eq. (4.14). The only difference in this case is that we sum $\mathfrak{C}(\vec{r}_j)$ over an additional layer of

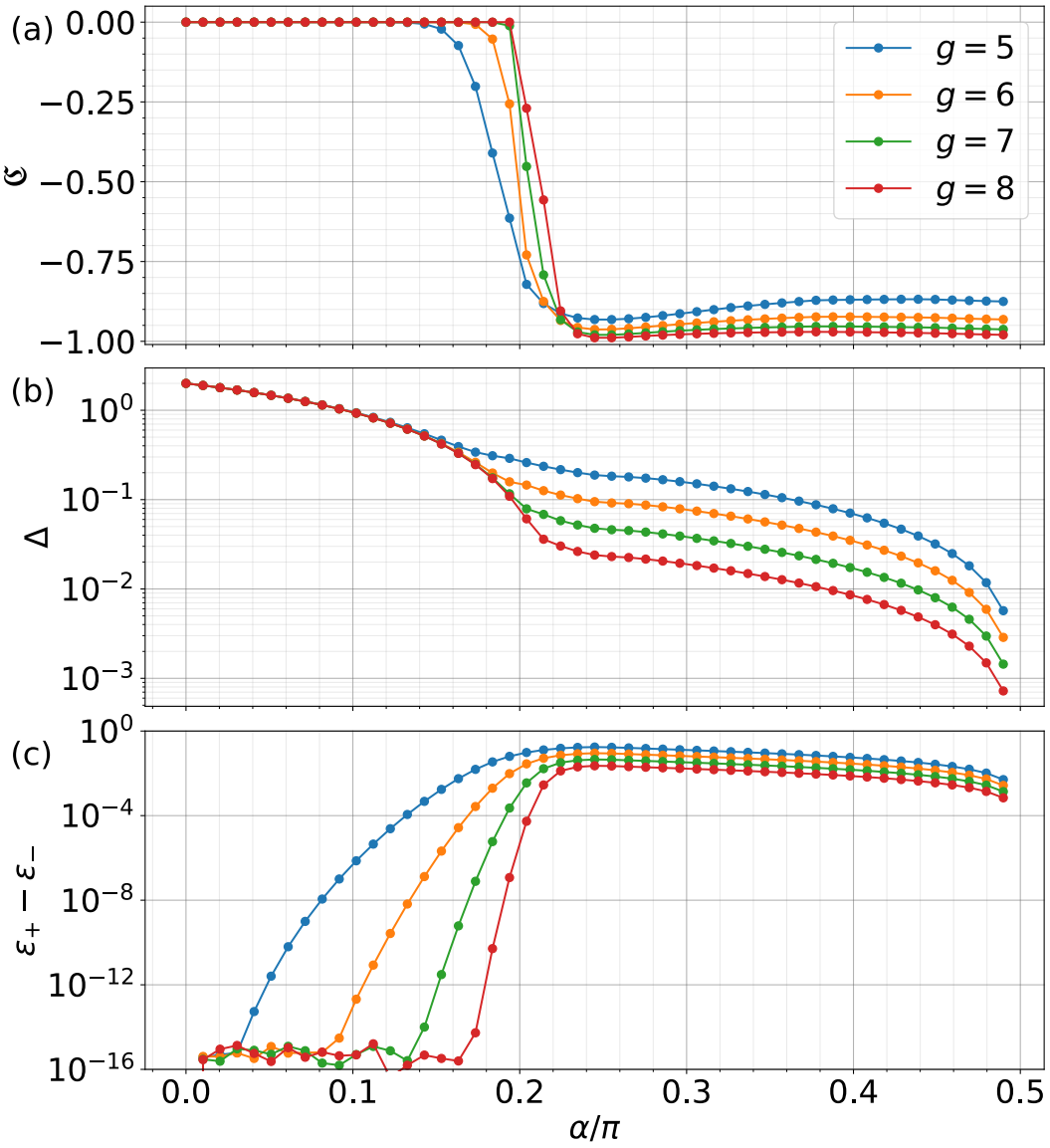

Figure 6.5: Scaling with system size of properties of the majorana spectrum in the Lieb's flux sector as a function of α. (a) Chern number as a function of α which shows a trivial to non-trivial transition in between $\alpha \approx 0.18\pi$ to $\alpha \approx 0.22\pi$ as α is increased. (b) Gap at zero energy in the majorana spectrum. The scaling as a function of system size also changes in between $\alpha \approx 0.18\pi$ to $\alpha \approx 0.22\pi$, indicating a transition from a gapped to a gapless phase in the thermodynamic limit. (c) The difference between the energies of the two states, $\varepsilon_+ = \varepsilon_{[N/2]+1}$ and $\varepsilon_- = \varepsilon_{[N/2]-1}$ as a function of α. This is an indicator of the change in the degeneracy in the majorana spectrum showing a transition from a three-fold degenerate zero energy state for $\alpha \lesssim 0.18\pi$ to a non-degenerate single zero energy majorana mode for $\alpha \gtrsim 0.22\pi$.

sites adjacent to those which immediately enclose the cross-hair. The reason for this would be clear in subsequent paragraphs.

6.3.1 *The gapped phase: $t \ll J$*

For $\alpha \lesssim 0.2\pi$, the spectrum has a gap with the presence of three degenerate majorana zero modes. These zero modes are found to be localized on the corner sites (sites with coordination number 2) of SG-3 as shown in Fig. 6.4(b). The states close to the edge of the gap are found to be bulk-like in nature. An example of such a state is shown in Fig. 6.4(c). The local Hall conductivity shows (Fig. 6.4(d)), the lack of any transverse charge transport signifying the lack of any first Chern character of the fermions in this phase. Given the spectrum in Fig. 6.4 is for a finite system, we study the scaling of the Chern number, gap and degeneracy as a function of system size (see Fig. 6.5). To measure the three-fold degeneracy, we calculate $\varepsilon_+ - \varepsilon_-$, where $\varepsilon_+ = \varepsilon_{[N/2]+1}$ and $\varepsilon_- = \varepsilon_{[N/2]-1}$. $\varepsilon_+ - \varepsilon_-$ going to zero would indicate a threefold degeneracy as $\varepsilon_{[N/2]} = 0$ due to the particle-hole symmetry. The gap can then be studied by computing $\Delta = \varepsilon_{[N/2]+2} - \varepsilon_{[N/2]-2}$. The gap is found to persist in the thermodynamic limit as shown by the system size scaling in Fig. 6.5(b). Similarly, the degeneracy of the majorana zero modes in the gapped phase becomes even more clear as one goes to higher system sizes (Fig. 6.5(c)).

Given that the three corner modes are separated by a gap, it is natural to wonder about the fate of these corner modes as a function of the disorder. Here, we study the effect of adding a disorder which randomly changes the interaction strength between the sites on SG-3. The disordered Hamiltonian for the original spin system is then defined as

$$H^{\text{dis}} = H + \sum_{<jk>} w_{jk} K_{jk}, \tag{6.24}$$

where w_{jk} is a random number distributed uniformly between $[-W/2, W/2]$. Given that the disorder only changes the interaction strength and not the form of the interaction itself, we can still perform the Jordan-Wigner transformation to fractionalize the spins into fermions and $\mathbb{Z}_2$ fluxes. H^{dis} can then be brought into a quadratic form in terms of fermionic degrees of freedom in exactly the way in which H_{maj} is obtained from H. Then the corresponding majorana Hamiltonian in the presence of disorder is given by

$$H^{\text{dis}}_{maj}(\{u_{jk}\}) = \sum_{<jk>} i(A_{jk} + w_{jk}) c_j c_k. \tag{6.25}$$

Notice that introducing such a disorder does not break the particle-hole symmetry of the system. This means that we can check the presence or absence of three-fold degenerate majorana zero modes by computing $\varepsilon_+ - \varepsilon_-$,

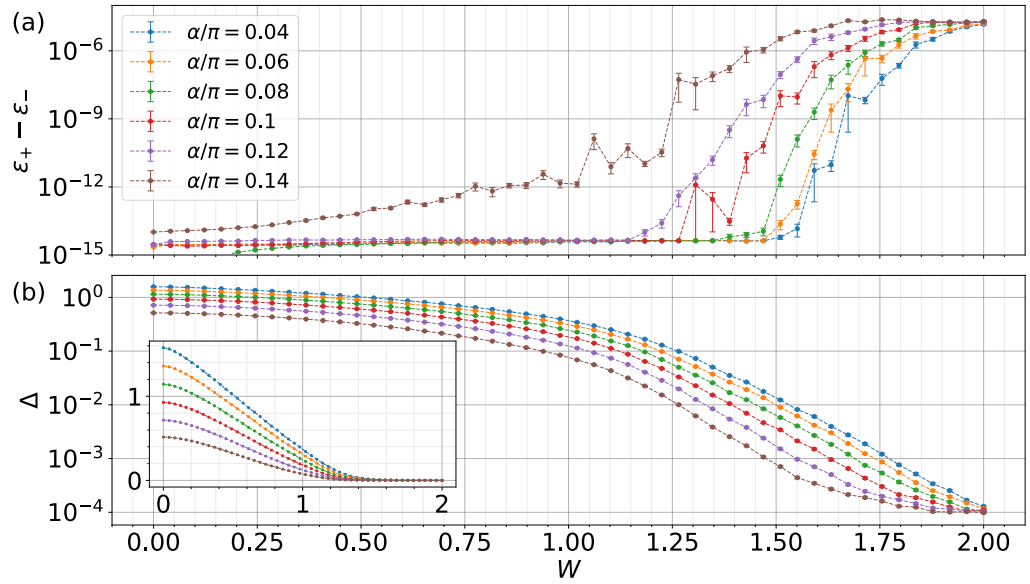

Figure 6.6: Robustness of the zero modes and the gap to disorder in the gapped phase. (a) Disorder average of the difference between the energies of the two states, $\varepsilon_+ = \varepsilon_{[N/2]+1}$ and $\varepsilon_- = \varepsilon_{[N/2]-1}$ as a function of disorder strength W, for different values of α, which shows the degeneracy to be fairly robust up to $W \approx \Delta(W = 0)$. (b) Disorder average of the gap Δ as a function of the disorder strength W. The inset shows the same data but in linear scale. The gap is found to decrease almost exponentially with W beyond $W \approx \Delta(W = 0)$, finally approaching the same order of magnitude as $\varepsilon_+ - \varepsilon_-$ indicating a gap closing. All calculations for this figure are done with SG-3 of generation $g = 7$ ($N = 3^7$ sites). Disorder averaging has been done over 1000 disorder realizations. The error bars show the standard deviation of the disorder averages.

and the gap by computing Δ. Fig. 6.6 shows the change in $\varepsilon_+ - \varepsilon_-$ and Δ as a function of the disorder strength W, for various tuning parameters α.

We find that the three-fold degeneracy and the corner localization of the three majorana zero modes are robust to disorder, up to disorder strength of the order of the disorder-free gap (Fig. 6.6(a)). Δ however shows an interesting behaviour as a function of disorder strength. We find that the Δ shows approximately linear decrease with the disorder strength for small disorders (inset of Fig. 6.6(b)). This however still preserves the gap as Δ still remains orders of magnitude higher than $\varepsilon_+ - \varepsilon_-$. Around $W \approx \Delta(W = 0)$, Δ decreases exponentially as a function of disorder strength, finally reaching the same order of magnitude as $\varepsilon_+ - \varepsilon_-$. This signifies a gap closing. At such high disorder strengths, the threefold degeneracy of the zero mode is lost and the localization of the zero mode at the corner sites is lost as well.

The robustness of the zero energy triply-degenerate majorana corner modes to particle-hole symmetric disorder shows the presence of a non-trivial topological character in this phase. However, as determined by the Chern number calculation (Fig. 6.5(a)), the first Chern character in this

phase is trivial. This means that the topological character in this phase must be of a higher order. The physical origin of the corner zero modes is also analogous to that of the boundary modes in the topological regime of the Kitaev chain. In the $t = 0, J = 1(\alpha = 0)$ limit, the system decomposes into a bunch of disconnected majorana links and 3 dangling corner majoranas. For every remaining link $< jk >$, the two majoranas c_j and c_k form a complex fermion giving rise to a degenerate spectrum with energy ± 1. For SG-3 of generation g, this degeneracy is $3(3^{g-1} - 1)/2$. The three dangling corner majorana modes remain at zero energy being gapped out from the rest of the spectrum. As $t/J = |\tan\alpha|$ is increased slightly, the system can be treated perturbatively around $\alpha = 0$ limit. It turns out that the first order perturbation is enough to replicate the spectral features of the system. In this limit, the links with strength J can be shrunk to sites representing complex fermions; the links with strength t result in inducing effective superconducting coupling between the complex-fermionic sites, similar to that obtained in the Kitaev chain. The corner modes however are not affected being protected by the gap similar to that in the Kitaev chain.

6.3.2 *The gapless phase: $t \gg J$*

For $\alpha \gtrsim 0.2\pi$, the zero energy gap starts to close with the presence of low energy states (shown in Fig. 6.3(b)). In this regime, the three-fold degeneracy of the majorana zero modes breaks leaving only one majorana zero mode which is protected by the fact that the system always has odd number of sites by definition and possesses particle-hole symmetry. We also find that the spacing between the energy levels near zero energy reduces exponentially as function of the generation of SG-3 (shown in Fig. 6.5(b)), suggesting a gapless phase in the thermodynamic limit. The local Hall conductivity shows presence of transverse charge transport (Fig. 6.7(d) and Fig. 6.8(d)) and is almost quantized to 1 (Fig. 6.5(a)), which shows a topologically non-trivial first Chern character. The majorana zero modes and the low-energy states are edge-like in nature. A few examples of the low-energy states are shown in Fig. 6.7(b-c) and Fig. 6.8(b-c).

However, the localization of the edge-like states and the local contribution to the Hall conductivity in the case of $t \gg J$ is different from the conventional localization (the $t = J$ case) of edge-like states which we have seen so far (compare Fig. 6.7 (b-d) with Fig. 6.8(b-d)). This is interesting in the first glance. However, this is simply a result of the interplay of self-similarity and the scale dependent link strengths (t being the link strength for the smallest triangles and J being the strength of the links connecting these triangles at all other scales). This behaviour can again be understood by looking at system perturbatively around $t \gg J$ or $\alpha \to \pi/2$ limit. In the $t = 1, J = 0(\alpha = \pi/2)$ limit, the system decomposes into 3^{g-1} disjoint majorana triangles. Each of the triangles have three modes with energies $\{\sqrt{3}, 0, -\sqrt{3}\}$. The effect of

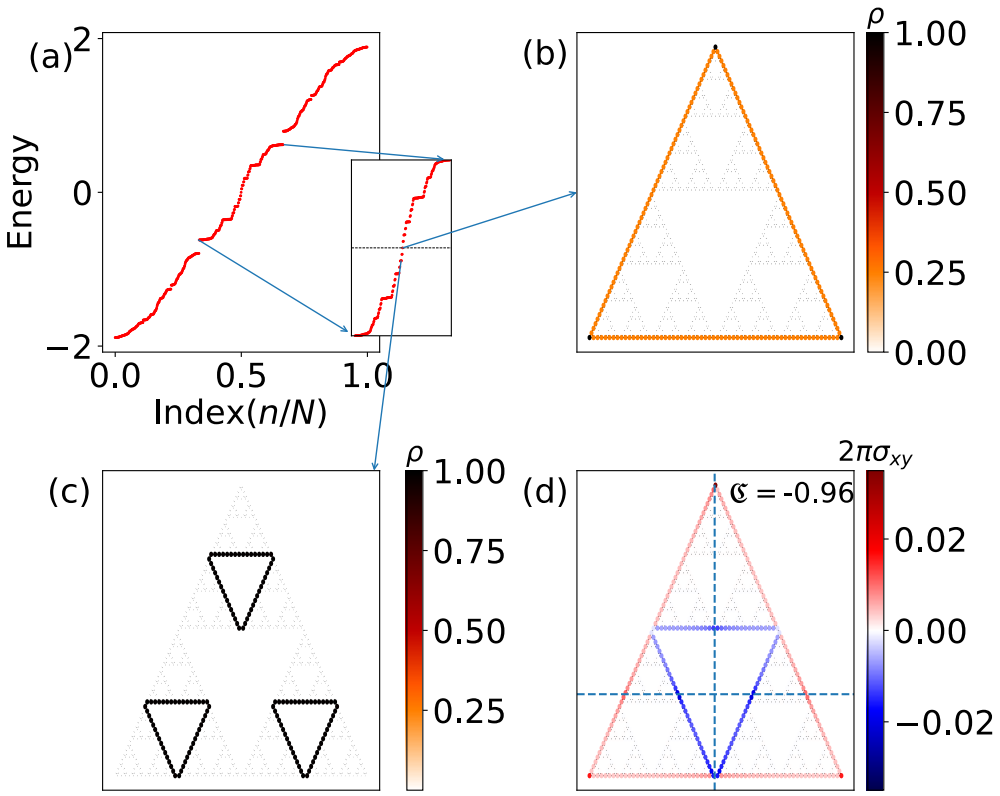

Figure 6.7: Spectrum and wavefunctions of H_{maj} for $\alpha = \pi/4$ ($t = J$). (a) Spectrum of H_{maj} and a zoomed in version of the same in the inset, showing the majorana zero mode and the low-energy edge-like modes. (b)-(c) Localization of the zero mode and a low-energy edge-like state. Arrows are drawn from the inset of (a) to (b) and (c) to show the corresponding energies the states whose localization has been shown in (b) and (c). (d) Local Hall conductivity at half-filling. The position of the cross-hair for the local Hall conductivity calculation is shown with the dashed lines in (d). The calculation has been done for $N = 3^6$ sites.

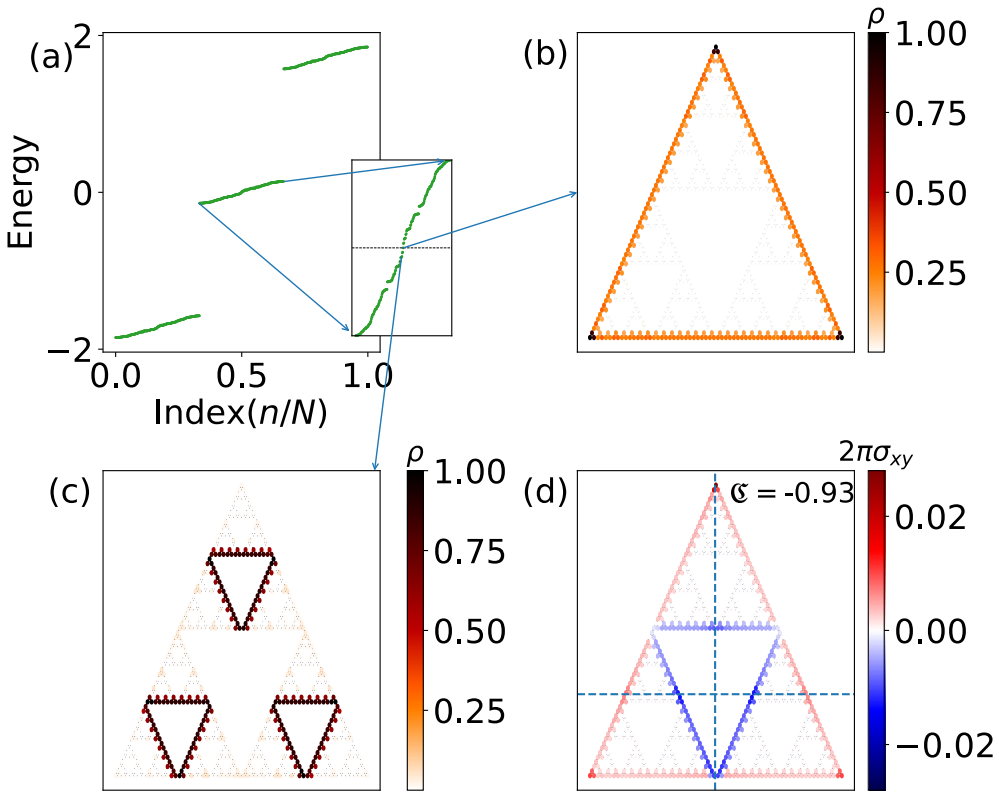

Figure 6.8: Spectrum and wavefunctions of H_{maj} for $\alpha = 0.45\pi$ ($t > J$). (a) Spectrum of H_{maj} and a zoomed in version of the same in the inset, showing the majorana zero mode and the low-energy edge-like modes. (b)-(c) Localization of the zero mode and a low-energy edge-like state. Arrows are drawn from the inset of (a) to (b) and (c) to show the corresponding energies the states whose localization has been shown in (b) and (c). (d) Local Hall conductivity at half-filling. The position of the cross-hair for the local Hall conductivity calculation is shown with the dashed lines in (d). The calculation has been done for $N = 3^6$ sites.

switching on the links with link strengths J can then be treated perturbatively. A first order perturbation results in an effective model in which the smallest triangles (link strength t) are shrunk to sites and are connected to another with link strength J. This is nothing but the same model as H_{maj} with $t = J$ but defined on an effective SG-3 with generation $g - 1$. As a result, the spectrum, which was previously degenerate at energies $-\sqrt{3}$, 0, and $\sqrt{3}$ in the $\alpha = 0$ limit, now takes a self-similar nature around each of the energies (notice the similarity in the inset of Fig. 6.8(a) and the Fig. 6.7(a)).

The topological character of the system in this regime can thus be considered to be the same as that in the $t = J$ case. The edge-like states in the effective model have exactly the same localization as the of the edge-like states shown in Fig. 6.7(b-c). But, given that sites of the effective model are essentially the triangles of the original model, the edge-like states in $t \gg J$ regime are localized on all the sites of the triangles that immediately enclose a given 'hole' in SG-3. This explains the unconventional nature of the localization of the edge-like states and the local contribution to the Hall-conductivity in this regime. And in order to account for exactly this in the Chern number computation, we have defined the Chern number to be $\mathfrak{C} = \sum_{j \in \mathcal{P}'} \mathfrak{C}(\vec{r}_j)$, where $\mathcal{P}'$ is the set of all sites on the triangles which immediately enclose the cross-hair. Notice that this definition is slightly different from that defined in Eq. (4.14) as here the sum is over an additional layer of sites adjacent to those which immediately enclose the cross-hair. The Chern number given in Fig. 6.5(a) is computed using the above definition instead of Eq. (4.14).

6.4 ANYONIC EXCITATIONS

In the previous sections, we studied the ground state of the system. We found that the ground state of the system lies on the Lieb's flux sector and the system undergoes a phase transition from a gapped phase to a gapless phase as we increase t/J. The system can be excited in two ways: (i) by exciting only the fermionic degrees of freedom, and (ii) by exciting the flux degrees of freedom. The properties of fermionic excitations can easily be studied from the spectrum of H_{maj} in the Lieb's flux sector. In this section, we focus on studying the properties of the flux excitations. We study these excitations by studying the majorana Hamiltonian, H_{maj}, away from the Lieb's flux sector. Starting from the ground state (Lieb's flux sector), we introduce excitations or vortices in the system by changing $w_L \to -w_L$ on some of the loops. This is done by setting $u_{jk} = -1$ for some type-z links in the system. Notice that there are some type-z links in the system which are present in only one loop and the rest of the type-z loops are shared by shared by two loops. This means setting $u_{jk} = -1$ on the latter would result

in the simultaneous creation of a pair of vortices.

6.4.1 *Majorana spectra for excitations*

We find that creating well-separated vortices in the gapped phase does not affect the low-energy part of the spectrum of H_{maj}. Specifically, zero energy corner modes remain unaffected as they are protected by the gap. However, in the gapless phase, creating vortices results in the significant change in the low-energy part of the majorana spectrum. We find that creating $2n$ well-separated vortices results in the creation of $2n$ additional majorana zero-modes, increasing the overall ground state degeneracy. The localization of these majorana zero modes varies for even and odd loops. At $t = J$, when vortices are created on loops of even length, the additional majorana zero modes are found to be strictly localized on the sites of the vortices irrespective of the distance between the vortices. A couple of examples are shown in Fig. 6.9(c,e). However, when vortices are created on the triangular plaquettes, the localization of the majorana zero modes has a non-trivial pattern and is dependent on the precise location of the vortices. We find that in this case, the zero modes are not only localized on the triangular plaquette carrying the vortex, but also on the sites which forms a loop with the least area enclosing all the nearest-neighbors of the vortex carrying plaquette. The nearest neighbors of the vortex carrying plaquette are nodes of the majorana zero modes. One such example has been shown in Fig. 6.9(h). Away from $t = J$ limit, the additional majorana zero modes are still found to be localized, but not strictly localized as the examples shown in Fig. 6.9

The non-trivial localization of the majorana zero modes in the presence of vortices in triangular loops is an artifact of the underlying structure of the graph. To see this, let us assume that H_{maj} can support strictly localized zero modes on a set of sites, say P. To bring H_{maj} into canonical form, we need to find eigenvectors of the matrix iA whose elements A_{jk} are given by Eq. (6.18). From Eq. (6.18), it is clear that the zero energy eigenvector of matrix A would basically be the majorana zero mode. The eigenvalue equation can then be decomposed into P and compliment of P, say Q resulting in

$$Ax = \begin{bmatrix} A_{PP} & A_{PQ} \\ A_{QP} & A_{QQ} \end{bmatrix} \begin{bmatrix} x_P \\ 0 \end{bmatrix} = 0, \tag{6.26}$$

where $x = [x_P, 0]^{\mathrm{T}}$ is the zero energy eigenstate localized on sites in P. For this to hold, A_{PP} and A_{QP} must simultaneously annihilate x_P for $x_P \neq [0, 0, \cdots]^{\mathrm{T}}$. As A_{PP} is anti-symmetric, so $x_P = [1, 1, \cdots]^{\mathrm{T}}$ is the only state which satisfies $A_{PP}x_P = 0$, up to normalization. In order to have $A_{QP}x_P = 0$, given any site $q \in Q$, we must have $\sum_p (A_{QP})_{qp} = 0$, where $p \in P$ is a nearest neighbor of q ($(A_{QP})_{pq}$ is non-zero only when q and p are nearest neighbors). This condition fails if P is the set of sites only on a

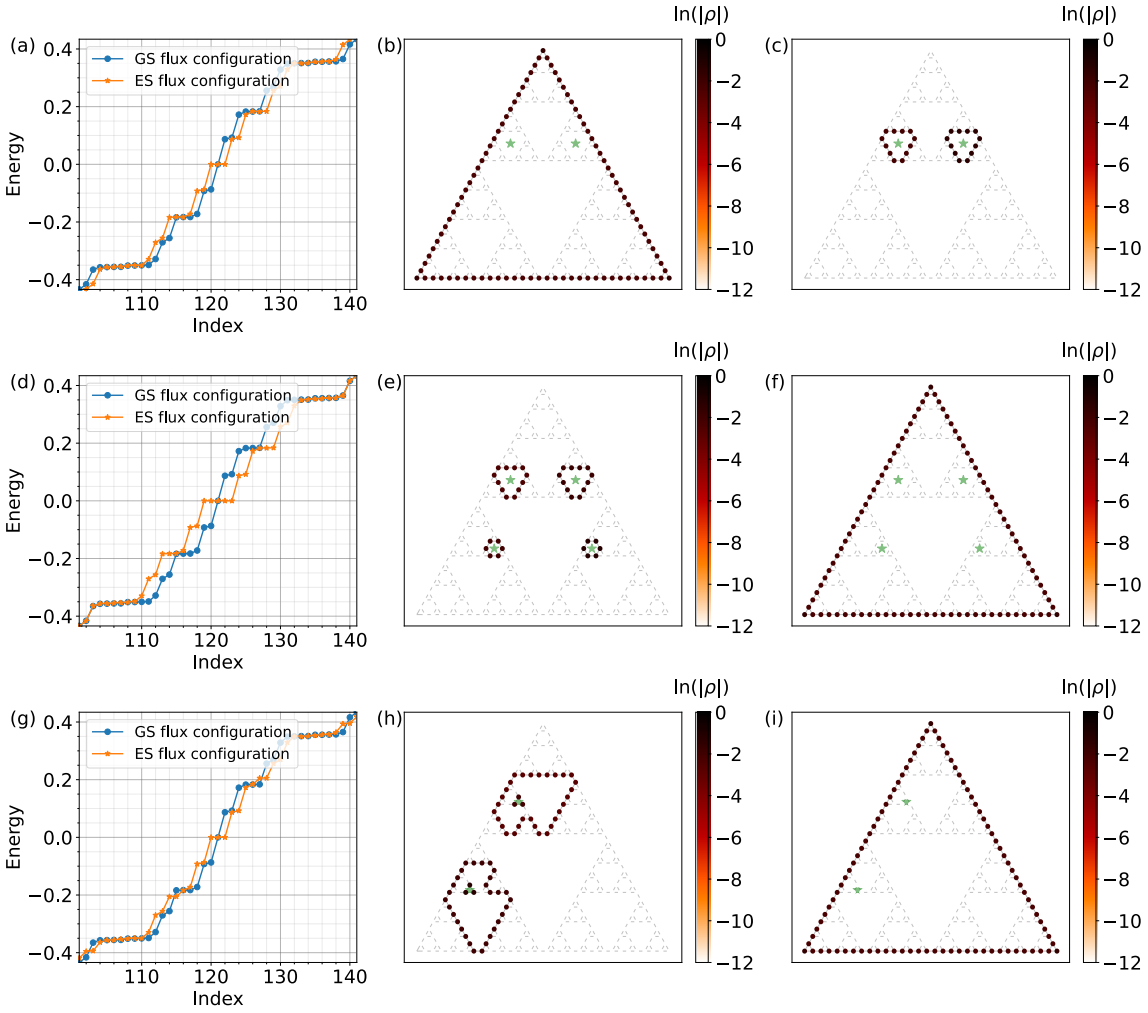

Figure 6.9: Majorana spectrum and localization of the majorana zero modes in the presence of vortices for $t = J(\alpha = 0.25)$. The spectrum of H_{maj} and localization of the zero modes for 2 vortices on even loops, 4 vortices on even loops, and 2 vortices on odd loops are shown in (a-c), (d-f), and (g-i) respectively. The loops which carry the vortices have been marked with a green star in (b,c,e,f,g,h). The low energy part of the spectrum of H_{maj} has been shown in (a), (d) and (g). The calculation has been done for $N = 3^5$ sites. In the legend of (a,d,g), 'GS flux sector stands for the ground state flux sector or the Lieb's flux sector, and 'ES flux sector' stands for excited state flux sector where the loops marked in (b,e,h) with a star carry vortices respectively.

triangular plaquette as in that case, we have at most one non-zero $(A_{QP})_{qp}$ for any $q \in Q$. The strict localization of the additional zero modes in the presence of vortices on loops of even length is also a consequence of the above. In that case, any $q \in Q$ has either 0 or 2 nearest neighbors in P. For $q \in Q$ which has two nearest neighbors in P, the corresponding matrix elements of A_{QP} have opposite sign satisfying $\sum_p (A_{QP})_{qp} = 0$. We note that the above arguments also hold true in the case of the Yao-Kivelson model [YK07] on decorated honeycomb lattice and one also finds such strict localization of the majorana zero modes for parameters $t = J$.

6.4.2 *Braiding*

The appearance of additional majorana zero modes in the presence of vortices leads to the increase in the many-body state degeneracy and signifies the possibility of anyonic statistics. In the previous section, we saw that the additional majorana modes in the presence of vortices are localized. So we ask the what phase does the many-body wavefunction gain when we switch the position of the vortices. Consider a many-body wavefunction $|\Psi(z_1, z_2)\rangle$ where z_1, z_2 are the positions of the vortices. Under an exchange of vortices, the new wavefunction $|\Psi(z_2, z_1)\rangle$ must be related to the previous one by $|\Psi(z_2, z_1)\rangle = U\,|\Psi(z_1, z_2)\rangle$, where U is phase if the wavefunction is non-degenerate. U is said to determine the characteristic quantum statistics: $U = 1$ gives bosonic statistics, $U = -1$ gives fermionic statistics, and $U = e^{i\phi}$ for $-\pi < \phi \leq \pi, \phi \neq \{0, \pi\}$ gives anyonic statistics. In the case when the wavefunction belongs to a degenerate manifold, then it is possible that the exchange of vortices can take the system to a different state of the degenerate manifold. In this case, U becomes a unitary matrix. In this case, it is also possible for the statistics to have non-abelian nature when U has off-diagonal elements. One example of such a case is the presence of non-abelian Ising anyons in the Kitaev Honeycomb model in the presence of a magnetic field [Kito6; LP09].

We study the quantum statistics of the system by studying the braiding the vortices in the system following Ref. [LP09]. To perform the braiding, we make use of the following fact that changing the sign of interaction strength $J_{jk}(t_{jk})$ on one of the links of, say $< jk >$, of the system is equivalent to $w_L \to -w_L$ for the loops which contain the link $< jk>$. This results in either creation of a pair of vortices or transfer of a vortex through the link $< jk >$, given that $< jk >$ is does not lie on the outermost loop of SG-3. Once we have created the vortices, to perform the braiding, we make sure to flip the interaction strength of only those links which does not create additional vortices. In the numerics, we obtain the matrix U using the Berry holonomy (see Eq. (6.29)). So to ensure adiabaticity, this process of changing the sign of the interaction strength of a given link $< jk >$ is done linearly in N_s in-

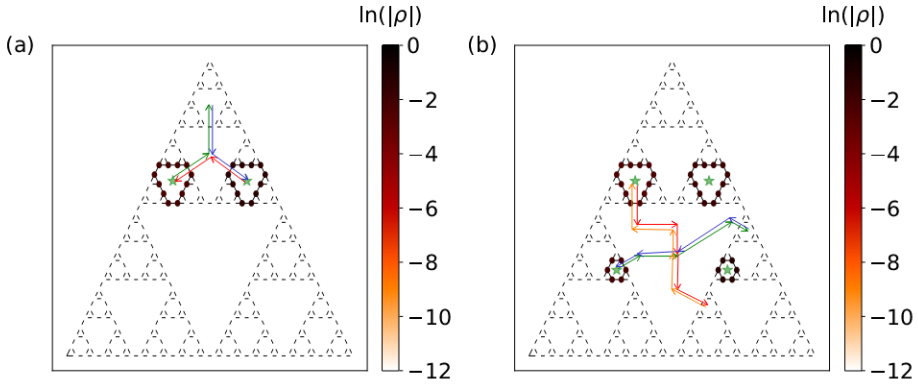

Figure 6.10: Braiding paths for the (a) 2-vortex (C_2) and (b) 4-vortex (C_4) configuration. The paths are marked by combination of directed arrows. For the 2-vortex configuration, the order of the path is given by [green, red, blue, green, red, blue]. For the 4-vortex configuration, the order of the trivial path (C_4^{triv}) is given by [green, blue, red, orange] and the order of the topological path (C_4)is given by [green, red, blue, orange]. In the numerics, the order in which the links which cut the path were flipped is determined by the direction of the arrows together with the order of the arrows mentioned above.

finitesimal steps such that at the s^{th} step, $A_{jk}(s) = A_{jk} \cdot (1 - 2s/N_s)$, where $A_{jk} = J_{jk}(t_{jk})$.

Consider a vortex configuration which such that the corresponding majorana Hamiltonian has M zero modes. Using the degenerate majorana zero modes, we can create a degenerate manifold of many-body states, $\{|\Psi_\alpha\rangle\}$, given by

$$|\Psi_\alpha\rangle = \sum_{\{k\ldots l=1|k\ldots l\neq\alpha\}}^{N_-+M-1} \frac{\varepsilon_{k\ldots l}}{\sqrt{(N_- + M - 1)!}} \psi_k^- \otimes \ldots \otimes \psi_l^- \tag{6.27}$$

where $iA\psi_k^\pm = \pm\epsilon_k\psi_k^\pm$, $\alpha \in \{1, 2, \ldots, M\}$, $N_- = (3^g - 1)/2$, and $\varepsilon_{k\ldots l}$ is a fully anti-symmetric tensor of rank $N_- + M - 1$. Now imagine the states $|\Psi_\alpha\rangle$ to be time-dependent. For such a case the inner-product between $|\Psi_\alpha(s)\rangle$ and $|\Psi_\beta(s')\rangle$ can be computed as

$$\langle\Psi_\alpha(s)|\Psi_\beta(s')\rangle = \det\left(B_{\alpha\beta}^{ss'}\right) \tag{6.28}$$

where $[B_{\alpha\beta}^{ss'}]_{kl} = \psi^{-\dagger}_k(s)\psi^-_l(s')$. Now consider the system to depend on a parameter λ (the interaction strengths on the links in this case). Upon varying λ along a closed path C, the evolution of degenerate subspace is given by the Berry holonomy Γ_C, for a path named C [PZ01; LP09]

$$\Gamma_C = \mathcal{P}\exp\oint_C A^\mu(\lambda)d\lambda_\mu = \lim_{N_s\to\infty} \mathcal{P}\prod_{s=1}^{N_s}\left(\sum_{\alpha=1}^{M} |\Psi_\alpha(\lambda(s))\rangle\langle\Psi_\alpha(\lambda(s))|\right) \tag{6.29}$$

where $[A^\mu(\lambda)]_{\alpha\beta} = \langle\Psi_\alpha(\lambda)|d/d\lambda^\mu|\Psi_\beta(\lambda)\rangle$. The second equality in Eq. (6.29) is obtained by discretizing the path C into N_s infinitesimal intervals of length

$\delta\lambda$ where $\lambda(s)$ denotes the value of the parameter at s^{th} step. The discrete holonomy is the suited for numerics as it can be well approximated by [LP09]

$$\Gamma_C \approx \mathcal{P} \prod_{s=1}^{N_s-1} \begin{bmatrix} B_{11}^{s,s+1} & \dots & B_{1M}^{s,s+1} \\ \vdots & \ddots & \vdots \\ B_{M1}^{s,s+1} & \dots & B_{MM}^{s,s+1} \end{bmatrix}. \tag{6.30}$$

We have done some preliminary computations of Γ_C for a 2-vortex and 4-vortex configuration at $t = J = \cos\pi/4$ for all links not crossing the braiding paths. The corresponding paths C_2 and C_4 are shown in Fig. 6.10. For the 2-vortex configuration, we have $M = 3$ (see Fig. 6.9(a)). In this case, we obtain the Berry holonomy

$$\begin{aligned} \Gamma_{C_2} &= \begin{bmatrix} 0.0001 + 0.9826i & 0 & 0 \\ 0 & -0.0001 - 0.9826i & 0 \\ 0 & 0 & 0.0001 + 0.9826i \end{bmatrix} \\ &\approx \begin{bmatrix} \exp\{i\pi/2\} & 0 & 0 \\ 0 & \exp\{-i\pi/2\} & 0 \\ 0 & 0 & \exp\{i\pi/2\} \end{bmatrix}. \end{aligned} \tag{6.31}$$

This shows that excitations in the 2-vortex configuration is anyonic and abelian in nature. The above computation was done with SG-3 with $g = 5$ and with different $N_s = 500$. For the 4-vortex configuration, we obtain the Berry holonomy,

$$\mathrm{Re}(\Gamma_{C_4}) = \begin{bmatrix} -0.0001 & 0.0 & 0.531 & -0.4877 & 0.2055 \\ 0.0 & -0.0001 & 0.0 & 0.0 & 0.0 \\ -0.531 & 0.0 & 0.0 & 0.2638 & 0.2055 \\ 0.4877 & 0.0 & -0.2639 & 0.0 & 0.3918 \\ -0.2055 & 0.0 & -0.2054 & -0.3917 & 0.0001 \end{bmatrix}$$

$$\mathrm{Im}(\Gamma_{C_4}) = \begin{bmatrix} -0.5855 & 0.0 & -0.1049 & -0.0857 & -0.2054 \\ 0.0 & -0.9826 & 0.0 & 0.0 & 0.0 \\ -0.1048 & 0.0 & -0.2426 & -0.653 & 0.2745 \\ -0.0858 & 0.0 & -0.653 & 0.0884 & 0.2507 \\ -0.2054 & 0.0 & 0.2746 & 0.2508 & 0.7396 \end{bmatrix}$$

.

$$\mathrm{Im}(\log(\Gamma_{C_4})) = \begin{bmatrix} -0.5 & -0.25 & -0.0621 & -0.9446 & -0.25 \\ -0.7501 & -0.5 & 0.7045 & 0.8187 & 0.5 \\ -0.938 & 0.2955 & -0.5 & -0.3778 & 0.2955 \\ -0.0554 & 0.1812 & -0.6223 & 0.5 & 0.1812 \\ -0.7501 & 0.5 & 0.7045 & 0.8187 & 0.5 \end{bmatrix} \pi$$

The numerical results presented above have been rounded upto 4 digits. Similar to the 2-vortex configuration, the above computation was also done with $g = 5$ and $N_s = 500$. This preliminary computation reveals some interesting features. First of all the presence of non-zero elements reveals non-abelian nature. We look at $\mathrm{Im}(\log(\Gamma_{C_4}))$ (element-wise operation) to get an idea about the phases appearing in Γ_{C_4}. We find that the phases appearing in the off-diagonal elements differ a lot from what is expected from Ising non-abelian anyons [LP09]. This hints towards the presence of fundamentally new anyons in this systems. However, one needs to verify these preliminary computations by checking its convergence as function of N_s.

6.5 SUMMARY

In this chapter, we demonstrate the existence of a topologically ordered chiral spin liquid within self-similar systems. We present an exact, solvable model on a self-similar system by generalizing the Kitaev model to the Sierpinski Gasket. Our approach involves a specialized Jordan-Wigner transformation, rendering the model exactly solvable. This system displays a fractionalization of particles into Majorana fermions and Z_2 fluxes, exhibiting a fractal density of states for Majorana modes. We find that the ground state of the system can be tuned from a gapped phase to gapless phase. The gapped phase features symmetry-protected Majorana corner modes, while the gapless phase hosts robust zero-energy and low-energy self-similar Majorana modes.

Furthermore, we investigate vortex excitations, revealing their intriguing localization properties, even for small fractal generations. These localized excitations exhibit anyonic behavior. Our preliminary calculations show that the anyons in the gapless phase in this system might be different from the Ising anyons which is obtained in the Kitaev model on Honeycomb lattice. These findings open up exciting possibilities for exploring unique topological phenomena within self-similar systems.

7

CONCLUSIONS AND OUTLOOK

In conclusion, we have presented a microscopic understanding an of the topological phases in self-similar structures from the perspective of adiabatic charge pumping and spectral flow. We have numerically investigated the spectral flow and the associated charge pumping when a flux tube is inserted through the structure and the flux through the tube is varied adiabatically. We have shown the nature of the spectral flow in the case of self-similar structures to be qualitatively different from that of translationally invariant non-interacting systems with a perpendicular magnetic field. We have established a correspondence between local Hall conductivity contributions and spectral flow in edge-like states, which have been approximated as eigenstates of the angular-momentum operator, exhibiting chiral properties.

We expect our results to generalize to a wider variety of self-similar structures and finite systems embedded in two dimensions, given that the systems are able to support eigenstates which are localized on sites which form loops in the graph of the Hamiltonian. More specifically, if a finite system, embedded in two dimensions, is able to support at least two different sets of eigenstates, localized on two different loops such that one loop completely encloses the other and are spatially separated from each other, then we expect the system to show spectral flow when the flux through the inner loop is varied adiabatically. As a result, we expect such systems to show quantized Hall response. The presence of edge-like states and spectral flow in self-similar systems of different Hausdorff dimension shown in Chapter. 4 supports this expectation.

Based on the understanding which we have presented, we come to the conclusion that the way in which the sites are coordinated in the structure in a primary determinant of whether or not the structure can host topological phases. A trivial example to this would be to consider a self-similar structures which lacks loops. To verify this, we have studied a geometry dependent non-interacting model on two different finite fractal structures (SG-3 and SG-4) with same Hausdorff dimension, which only differ in the way the sites are coordinated. In the presence of additional non-spatial symmetries, we have found that the interplay of local coordination and the non-spatial symmetry becomes an important determining factor for the presence of topological phases in the system.

However, it is still unclear what kind of self-similar structures or finite systems, in general, would support such states localized on loops. Also, among self- similar structures, every structure has an unique fundamental

self-similar repeating unit which is iteratively used to generate the structure of higher generations. The relation between the structure of such fundamental self-similar repeating units and the ability of the system to support localized states on loops is not known yet. Form the perspective of non-interacting systems, these can be some ares of future research.

We have demonstrated the existence of a topologically ordered chiral spin liquid in non-integer dimensions by generalizing the Kitaev model to the Sierpinski Gasket. By defining a special Jordan-Wigner transformation, we have shown exact fractionalization of spins into Majorana fermions and Z2 fluxes, exhibiting a fractal density of states for Majorana modes. We have found that the ground state of the system can be tuned from a gapped phase to a gapless phase. The gapped phase is found to host symmetry-protected Majorana corner modes, while the gapless phase hosts robust zero-energy and low-energy self-similar Majorana edge-like modes. We have also investigated vortex excitations which are found to be highly localized even for small fractal generation. These localized excitations have exhibited anyonic behavior.

With the experimental realization of quantum fractals, the implications of this work extend beyond the theoretical realm, offering a foundation for future research in this domain. The open questions surrounding the support of localized states on loops and the relationship between fundamental self-similar repeating units and localized states are enticing directions for further exploration. Moreover, the realization of non-trivial topological order in fractals opens the door to the several possible fascinating studies. Two key differences of these systems from their lattice counterparts are the self-similar nature of the majorana spectra and possible exotic non-abelian anyons. The effect of the self-similar character of the majorana spectra would be reflected in the finite temperature physics. So it would be very interesting to study the finite temperature physics of these system. Another research direction is to study interacting models which are experimentally more accessible but are not exactly solvable on self-similar systems. Perhaps one way of studying such models on self-similar systems would be to use the toolbox of tensor-network states as the inherent self-similarity of these structures can come in handy for exact contraction of the tensors.

BIBLIOGRAPHY

[Aga19] Adhip Agarwala. "Seeking Topological Phases in Fractals." In: *Excursions in Ill-Condensed Quantum Matter: From Amorphous Topological Insulators to Fractional Spins*. Cham: Springer International Publishing, 2019, pp. 81–92. ISBN: 978-3-030-21511-8. DOI: 10.1007/978-3-030-21511-8_4. URL: https://doi.org/10.1007/978-3-030-21511-8_4.

[AS17] Adhip Agarwala and Vijay B. Shenoy. "Topological Insulators in Amorphous Systems." In: *Phys. Rev. Lett.* 118 (23 2017), p. 236402. DOI: 10.1103/PhysRevLett.118.236402. URL: https://link.aps.org/doi/10.1103/PhysRevLett.118.236402.

[AZ97] Alexander Altland and Martin R. Zirnbauer. "Nonstandard symmetry classes in mesoscopic normal-superconducting hybrid structures." In: *Phys. Rev. B* 55 (2 1997), pp. 1142–1161. DOI: 10.1103/PhysRevB.55.1142. URL: https://link.aps.org/doi/10.1103/PhysRevB.55.1142.

[ABA04] James G Analytis, Stephen J Blundell, and Arzhang Ardavan. "Landau levels, molecular orbitals, and the Hofstadter butterfly in finite systems." In: *American Journal of Physics* 72.5 (2004), pp. 613–618.

[AOP16] János K. Asbóth, László Oroszlány, and András Pályi. "Two-Dimensional Chern Insulators: The Qi-Wu-Zhang Model." In: *A Short Course on Topological Insulators: Band Structure and Edge States in One and Two Dimensions*. Cham: Springer International Publishing, 2016, pp. 85–98. ISBN: 978-3-319-25607-8. DOI: 10.1007/978-3-319-25607-8_6. URL: https://doi.org/10.1007/978-3-319-25607-8_6.

[ASS94] Joseph E Avron, Ruedi Seiler, and Barry Simon. "Charge deficiency, charge transport and comparison of dimensions." In: *Communications in mathematical physics* 159.2 (1994), pp. 399–422.

[BKP85] Jayanth R. Banavar, Leo Kadanoff, and A. M. M. Pruisken. "Energy spectrum for a fractal lattice in a magnetic field." In: *Phys. Rev. B* 31 (3 1985), pp. 1388–1395. DOI: 10.1103/PhysRevB.31.1388. URL: https://link.aps.org/doi/10.1103/PhysRevB.31.1388.

[BMS07] G. Baskaran, Saptarshi Mandal, and R. Shankar. "Exact Results for Spin Dynamics and Fractionalization in the Kitaev Model." In: *Phys. Rev. Lett.* 98 (24 2007), p. 247201. DOI: 10.1103/PhysRevLett.98.247201. URL: https://link.aps.org/doi/10.1103/PhysRevLett.98.247201.

[BHZ06] B. Andrei Bernevig, Taylor L. Hughes, and Shou-Cheng Zhang. "Quantum Spin Hall Effect and Topological Phase Transition in HgTe Quantum Wells." In: *Science* 314.5806 (2006), pp. 1757–1761. ISSN: 0036-8075. DOI: 10.1126/science.1133734. URL: https://science.sciencemag.org/content/314/5806/1757.

[BR11] Raffaello Bianco and Raffaele Resta. "Mapping topological order in coordinate space." In: *Phys. Rev. B* 84 (24 2011), 241106(R). DOI: 10.1103/PhysRevB.84.241106. URL: https://link.aps.org/doi/10.1103/PhysRevB.84.241106.

[BCN18] Marta Brzezińskiska, Ashley M. Cook, and Titus Neupert. "Topology in the Sierpiński-Hofstadter problem." In: *Phys. Rev. B* 98 (20 2018), p. 205116. DOI: 10.1103/PhysRevB.98.205116. URL: https://link.aps.org/doi/10.1103/PhysRevB.98.205116.

[Chi+16] Ching-Kai Chiu, Jeffrey C. Y. Teo, Andreas P. Schnyder, and Shinsei Ryu. "Classification of topological quantum matter with symmetries." In: *Rev. Mod. Phys.* 88 (3 2016), p. 035005. DOI: 10.1103/RevModPhys.88.035005. URL: https://link.aps.org/doi/10.1103/RevModPhys.88.035005.

[Dom+83] Eytan Domany, Shlomo Alexander, David Bensimon, and Leo P. Kadanoff. "Solutions to the Schrödinger equation on some fractal lattices." In: *Phys. Rev. B* 28 (6 1983), pp. 3110–3123. DOI: 10.1103/PhysRevB.28.3110. URL: https://link.aps.org/doi/10.1103/PhysRevB.28.3110.

[DMN20] Callum W. Duncan, Sourav Manna, and Anne E. B. Nielsen. "Topological models in rotationally symmetric quasicrystals." In: *Phys. Rev. B* 101 (11 2020), p. 115413. DOI: 10.1103/PhysRevB.101.115413. URL: https://link.aps.org/doi/10.1103/PhysRevB.101.115413.

[FZG23] Ruihua Fan, Pengfei Zhang, and Yingfei Gu. *Generalized Real-space Chern Number Formula and Entanglement Hamiltonian*. 2023. arXiv: 2211.04510 [cond-mat.str-el].

[FGB12] Chen Fang, M.J. Gilbert, and B.A. Bernevig. "Bulk topological invariants in noninteracting point group symmetric insulators." In: *Phys. Rev. B* 86 (11 2012), p. 115112. DOI: 10.1103/PhysRevB.86.115112. URL: https://link.aps.org/doi/10.1103/PhysRevB.86.115112.

[FJK11] Lukasz Fidkowski, T. S. Jackson, and Israel Klich. "Model Characterization of Gapless Edge Modes of Topological Insulators Using Intermediate Brillouin-Zone Functions." In: *Phys. Rev. Lett.* 107 (3 2011), p. 036601. DOI: 10.1103/PhysRevLett.107.036601. URL: https://link.aps.org/doi/10.1103/PhysRevLett.107.036601.

[Fis+21] Sonja Fischer, Michal van Hooft, Twan van der Meijden, C. MoraisSmith, Lars Fritz, and Mikael Fremling. "Robustness of chiral edge modes in fractal-like lattices below two dimensions: A case study." In: *Phys. Rev. Research* 3 (4 2021), p. 043103. DOI: 10.1103/PhysRevResearch.3.043103. URL: https://link.aps.org/doi/10.1103/PhysRevResearch.3.043103.

[Fre+20] Mikael Fremling, Michal van Hooft, C. MoraisSmith, and Lars Fritz. "Existence of robust edge currents in Sierpiński fractals." In: *Phys. Rev. Research* 2 (1 2020), p. 013044. DOI: 10.1103/PhysRevResearch.2.013044. URL: https://link.aps.org/doi/10.1103/PhysRevResearch.2.013044.

[Fu11] Liang Fu. "Topological Crystalline Insulators." In: *Phys. Rev. Lett.* 106 (10 2011), p. 106802. DOI: 10.1103/PhysRevLett.106.106802. URL: https://link.aps.org/doi/10.1103/PhysRevLett.106.106802.

[FK07] Liang Fu and C. L. Kane. "Topological insulators with inversion symmetry." In: *Phys. Rev. B* 76 (4 2007), p. 045302. DOI: 10.1103/PhysRevB.76.045302. URL: https://link.aps.org/doi/10.1103/PhysRevB.76.045302.

[Ghe+87] J.M. Ghez, Yin Yu Wang, R. Rammal, B. Pannetier, and J. Bellissard. "Band spectrum for an electron on a Sierpinski gasket in a magnetic field." In: *Solid State Communications* 64.10 (1987), pp. 1291–1294. ISSN: 0038-1098. DOI: https://doi.org/10.1016/0038-1098(87)90628-4. URL: https://www.sciencedirect.com/science/article/pii/0038109887906284.

[Gro+14] Christoph W Groth, Michael Wimmer, Anton R Akhmerov, and Xavier Waintal. "Kwant: a software package for quantum transport." In: *New Journal of Physics* 16.6 (2014), p. 063065. DOI: 10.1088/1367-2630/16/6/063065. URL: https://doi.org/10.1088%2F1367-2630%2F16%2F6%2F063065.

[Hal82] B. I. Halperin. "Quantized Hall conductance, current-carrying edge states, and the existence of extended states in a two-dimensional disordered potential." In: *Phys. Rev. B* 25 (4 1982), pp. 2185–2190. DOI: 10.1103/PhysRevB.25.2185. URL: https://link.aps.org/doi/10.1103/PhysRevB.25.2185.

[Hof76] Douglas R. Hofstadter. "Energy levels and wave functions of Bloch electrons in rational and irrational magnetic fields." In: *Phys. Rev. B* 14 (6 1976), pp. 2239–2249. DOI: 10.1103/PhysRevB.14.2239. URL: https://link.aps.org/doi/10.1103/PhysRevB.14.2239.

[IKY20] Askar A. Iliasov, Mikhail I. Katsnelson, and Shengjun Yuan. "Hall conductivity of a Sierpiński carpet." In: *Phys. Rev. B* 101 (4 2020), p. 045413. DOI: 10.1103/PhysRevB.101.045413. URL: https://link.aps.org/doi/10.1103/PhysRevB.101.045413.

[Iva+22] Moein N. Ivaki, Isac Sahlberg, Kim Pöyhönen, and Teemu Ojanen. "Topological random fractals." In: *Communications Physics* 5.1 (Dec. 2022). DOI: 10.1038/s42005-022-01101-z. URL: https://doi.org/10.1038/s42005-022-01101-z.

[KM05] C. L. Kane and E. J. Mele. "Quantum Spin Hall Effect in Graphene." In: *Phys. Rev. Lett.* 95 (22 2005), p. 226801. DOI: 10.1103/PhysRevLett.95.226801. URL: https://link.aps.org/doi/10.1103/PhysRevLett.95.226801.

[Kim98] J. C. Kimball. "States on the Sierpinski Triangle." In: *Foundations of Physics* 28 (1 1998), pp. 87–105. ISSN: 1572-9516. DOI: 10.1023/A:1018760504393. URL: https://doi.org/10.1023/A:1018760504393.

[Kito6] Alexei Kitaev. "Anyons in an exactly solved model and beyond." In: *Annals of Physics* 321.1 (2006). January Special Issue, pp. 2 –111. ISSN: 0003-4916. DOI: https://doi.org/10.1016/j.aop.2005.10.005. URL: http://www.sciencedirect.com/science/article/pii/S0003491605002381.

[Kito9] Alexei Kitaev. "Periodic table for topological insulators and superconductors." In: *AIP Conference Proceedings* 1134.1 (May 2009), pp. 22–30. ISSN: 0094-243X. DOI: 10.1063/1.3149495. eprint: https://pubs.aip.org/aip/acp/article-pdf/1134/1/22/11584243/22_1_online.pdf. URL: https://doi.org/10.1063/1.3149495.

[KDP80] K. v. Klitzing, G. Dorda, and M. Pepper. "New Method for High-Accuracy Determination of the Fine-Structure Constant Based on Quantized Hall Resistance." In: *Phys. Rev. Lett.* 45 (6 1980), pp. 494–497. DOI: 10.1103/PhysRevLett.45.494. URL: https://link.aps.org/doi/10.1103/PhysRevLett.45.494.

[Lah+08] Ville Lahtinen, Graham Kells, Angelo Carollo, Tim Stitt, Jiri Vala, and Jiannis K. Pachos. "Spectrum of the non-abelian phase in Kitaev's honeycomb lattice model." In: *Annals of Physics* 323.9 (2008), pp. 2286–2310. ISSN: 0003-4916. DOI: https://doi.org/10.1016/j.aop.2007.12.009. URL: https://www.sciencedirect.com/science/article/pii/S0003491607001959.

[LP09] Ville Lahtinen and Jiannis K Pachos. "Non-Abelian statistics as a Berry phase in exactly solvable models." In: *New Journal of Physics* 11.9 (2009), p. 093027. DOI: 10.1088/1367-2630/11/9/093027. URL: https://dx.doi.org/10.1088/1367-2630/11/9/093027.

[Lau81] R. B. Laughlin. "Quantized Hall conductivity in two dimensions." In: *Phys. Rev. B* 23 (10 1981), pp. 5632–5633. DOI: 10.1103/PhysRevB.23.5632. URL: https://link.aps.org/doi/10.1103/PhysRevB.23.5632.

[LH10] T. A. Loring and M. B. Hastings. "Disordered topological insulators via C^* – *algebras*." In: *EPL (Europhysics Letters)* 92.6 (Dec. 2010), p. 67004. DOI: 10.1209/0295-5075/92/67004. URL: https://doi.org/10.1209/0295-5075/92/67004.

[Lor19] Terry A. Loring. *A Guide to the Bott Index and Localizer Index*. 2019. DOI: 10.48550/ARXIV.1907.11791. URL: https://arxiv.org/abs/1907.11791.

[Lud15] Andreas W W Ludwig. "Topological phases: classification of topological insulators and superconductors of non-interacting fermions, and beyond." In: *Physica Scripta* T168 (2015), p. 014001. DOI: 10.1088/0031-8949/2015/t168/014001. URL: https://doi.org/10.1088%2F0031-8949%2F2015%2Ft168%2F014001.

[MNR22] Sourav Manna, Snehasish Nandy, and Bitan Roy. "Higher-order topological phases on fractal lattices." In: *Phys. Rev. B* 105 (20 2022), p. L201301. DOI: 10.1103/PhysRevB.105.L201301. URL: https://link.aps.org/doi/10.1103/PhysRevB.105.L201301.

[Mit+18] Noah P. Mitchell, Lisa M. Nash, Daniel Hexner, Ari M. Turner, and William T. M. Irvine. "Amorphous topological insulators constructed from random point sets." In: *Nature Physics* 14.4 (2018), pp. 380–385. ISSN: 1745-2481. DOI: 10.1038/s41567-017-0024-5. URL: https://doi.org/10.1038/s41567-017-0024-5.

[PZ01] JIANNIS PACHOS and PAOLO ZANARDI. "QUANTUM HOLONOMIES FOR QUANTUM COMPUTING." In: *International Journal of Modern Physics B* 15.09 (Apr. 2001), pp. 1257–1285. DOI: 10.1142/s0217979201004836. URL: https://doi.org/10.1142/s0217979201004836.

[PP19] Shriya Pai and Abhinav Prem. "Topological states on fractal lattices." In: *Phys. Rev. B* 100 (15 2019), p. 155135. DOI: 10.1103/PhysRevB.100.155135. URL: https://link.aps.org/doi/10.1103/PhysRevB.100.155135.

[PH58] Linus Pauling and Roger Hayward. *No More War!* Liberty book club. Dodd, Mead, 1958. URL: https://books.google.de/books?id=ncmxf-iyYoQC.

[Pra16] Subhasree Pradhan. "Hofstadter butterfly in the Falicov–Kimball model on some finite 2D lattices." In: *Journal of Physics: Condensed Matter* 28.50 (2016), p. 505502. DOI: 10.1088/0953-8984/28/50/505502. URL: https://dx.doi.org/10.1088/0953-8984/28/50/505502.

[PHB10] Emil Prodan, Taylor L. Hughes, and B. Andrei Bernevig. "Entanglement Spectrum of a Disordered Topological Chern Insulator." In: *Phys. Rev. Lett.* 105 (11 2010), p. 115501. DOI: 10.1103/PhysRevLett.105.115501. URL: https://link.aps.org/doi/10.1103/PhysRevLett.105.115501.

[Ram85] R. Rammal. "Landau level spectrum of Bloch electrons in a honeycomb lattice." In: *Journal de Physique* 46.8 (1985), pp. 1345–1354. DOI: 10.1051/jphys:019850046080134500. URL: https://doi.org/10.1051/jphys:019850046080134500.

[RT82] R. Rammal and G. Toulouse. "Spectrum of the Schrödinger Equation on a Self-Similar Structure." In: *Phys. Rev. Lett.* 49 (16 1982), pp. 1194–1197. DOI: 10.1103/PhysRevLett.49.1194. URL: https://link.aps.org/doi/10.1103/PhysRevLett.49.1194.

[SN21] Saswat Sarangi and Anne E. B. Nielsen. "Effect of coordination on topological phases on self-similar structures." In: *Phys. Rev. B* 104 (4 2021), p. 045147. DOI: 10.1103/PhysRevB.104.045147. URL: https://link.aps.org/doi/10.1103/PhysRevB.104.045147.

[SN23] Saswat Sarangi and Anne E. B. Nielsen. "Adiabatic pumping and transport in the Sierpinski-Hofstadter model." In: *Phys. Rev. Res.* 5 (3 2023), p. 033132. DOI: 10.1103/PhysRevResearch.5.033132. URL: https://link.aps.org/doi/10.1103/PhysRevResearch.5.033132.

[Sch+08] Andreas P. Schnyder, Shinsei Ryu, Akira Furusaki, and Andreas W. W. Ludwig. "Classification of topological insulators and superconductors in three spatial dimensions." In: *Phys. Rev. B* 78 (19 2008), p. 195125. DOI: 10.1103/PhysRevB.78.195125. URL: https://link.aps.org/doi/10.1103/PhysRevB.78.195125.

[SW89] Alfred Shapere and Frank Wilczek. *Geometric phases in physics*. Vol. 5. World scientific, 1989.

[Sla+13] Robert-Jan Slager, Andrej Mesaros, Vladimir Juričić, and Jan Zaanen. "The space group classification of topological band-insulators." In: *Nature Physics* 9 (2 2013), pp. 98–102. ISSN: 1745-2481. DOI: 10.1038/nphys2513. URL: https://doi.org/10.1038/nphys2513.

[SM20] J. Spence and E. Malone. *Observations, anecdotes, and characters, of books and men. Arranged with notes by E. Malone*. John Murray, 1820.

[Tho+82] D. J. Thouless, M. Kohmoto, M. P. Nightingale, and M. den Nijs. "Quantized Hall Conductance in a Two-Dimensional Periodic Potential." In: *Phys. Rev. Lett.* 49 (6 1982), pp. 405–408. DOI: 10.1103/PhysRevLett.49.405. URL: https://link.aps.org/doi/10.1103/PhysRevLett.49.405.

[TSG82] D. C. Tsui, H. L. Stormer, and A. C. Gossard. "Two-Dimensional Magnetotransport in the Extreme Quantum Limit." In: *Phys. Rev. Lett.* 48 (22 1982), pp. 1559–1562. DOI: 10.1103/PhysRevLett.48.1559. URL: https://link.aps.org/doi/10.1103/PhysRevLett.48.1559.

[WEN90] X. G. WEN. "TOPOLOGICAL ORDERS IN RIGID STATES." In: *International Journal of Modern Physics B* 04.02 (1990), pp. 239–271. DOI: 10.1142/S0217979290000139. eprint: https://doi.org/10.1142/S0217979290000139. URL: https://doi.org/10.1142/S0217979290000139.

[Xu+21] Xiao-Yun Xu, Xiao-Wei Wang, Dan-Yang Chen, C. Morais Smith, and Xian-Min Jin. "Quantum transport in fractal networks." In: *Nature Photonics* 15.9 (July 2021), pp. 703–710. DOI: 10.1038/s41566-021-00845-4. URL: https://doi.org/10.1038/s41566-021-00845-4.

[Yan+20] Zhaoju Yang, Eran Lustig, Yaakov Lumer, and Mordechai Segev. "Photonic Floquet topological insulators in a fractal lattice." In: *Light: Science &amp Applications* 9.1 (July 2020). DOI: 10.1038/s41377-020-00354-z. URL: https://doi.org/10.1038/s41377-020-00354-z.

[YK07] Hong Yao and Steven A. Kivelson. "Exact Chiral Spin Liquid with Non-Abelian Anyons." In: *Phys. Rev. Lett.* 99 (24 2007), p. 247203. DOI: 10.1103/PhysRevLett.99.247203. URL: https://link.aps.org/doi/10.1103/PhysRevLett.99.247203.

[Zhe+22] Shengjie Zheng, Xianfeng Man, Ze-Lin Kong, Zhi-Kang Lin, Guiju Duan, Ning Chen, Dejie Yu, Jian-Hua Jiang, and Baizhan Xia. "Observation of fractal higher-order topological states in acoustic metamaterials." In: *Science Bulletin* 67.20 (Oct. 2022), pp. 2069–2075. DOI: 10.1016/j.scib.2022.09.020. URL: https://doi.org/10.1016/j.scib.2022.09.020.

[dBL22] Peru d'Ornellas, Ryan Barnett, and Derek K. K. Lee. "Quantized bulk conductivity as a local Chern marker." In: *Phys. Rev. B* 106 (15 2022), p. 155124. DOI: 10.1103/PhysRevB.106.155124. URL: https://link.aps.org/doi/10.1103/PhysRevB.106.155124.

ERKLÄRUNG

Hiermit versichere ich, Saswat Sarangi, dass ich die vorliegende Arbeit ohne unzulässige Hilfe Dritter und ohne Benutzung anderer als der angegebenen Hilfsmittel angefertigt habe; die aus fremden Quellen direkt oder indirekt übernommenen Gedanken sind als solche kenntlich gemacht. Die Arbeit wurde bisher weder im Inland noch im Ausland in gleicher oder ähnlicher Form einer anderen Prüfungsbehörde vorgelegt. Diese Arbeit wurde unter der wissenschaftlichen Betreuung von Prof. Dr. Anne E. B. Nielsen. und Prof. Dr. Roderich Moessner am Max-Planck-Institut für Physik komplexer Systeme in Dresden angefertigt. Ich erkläre hiermit, dass keine früheren erfolglosen Promotionsverfahren stattgefunden haben. Ich erkenne die Promotionsordnung der Fakultät für Mathematik und Naturwissenschaften der Technische Universität Dresden an.

Dresden, Deutschland, March, 2024

Saswat Sarangi

COLOPHON

This document was typeset using the typographical look-and-feel `classicthesis` developed by André Miede and Ivo Pletikosić. The style was inspired by Robert Bringhurst's seminal book on typography *"The Elements of Typographic Style"*. `classicthesis` is available for both LaTeX and LyX:

https://bitbucket.org/amiede/classicthesis/